Monitoring deformation in glasshouses using InSAR

Pavithra Raghunathan

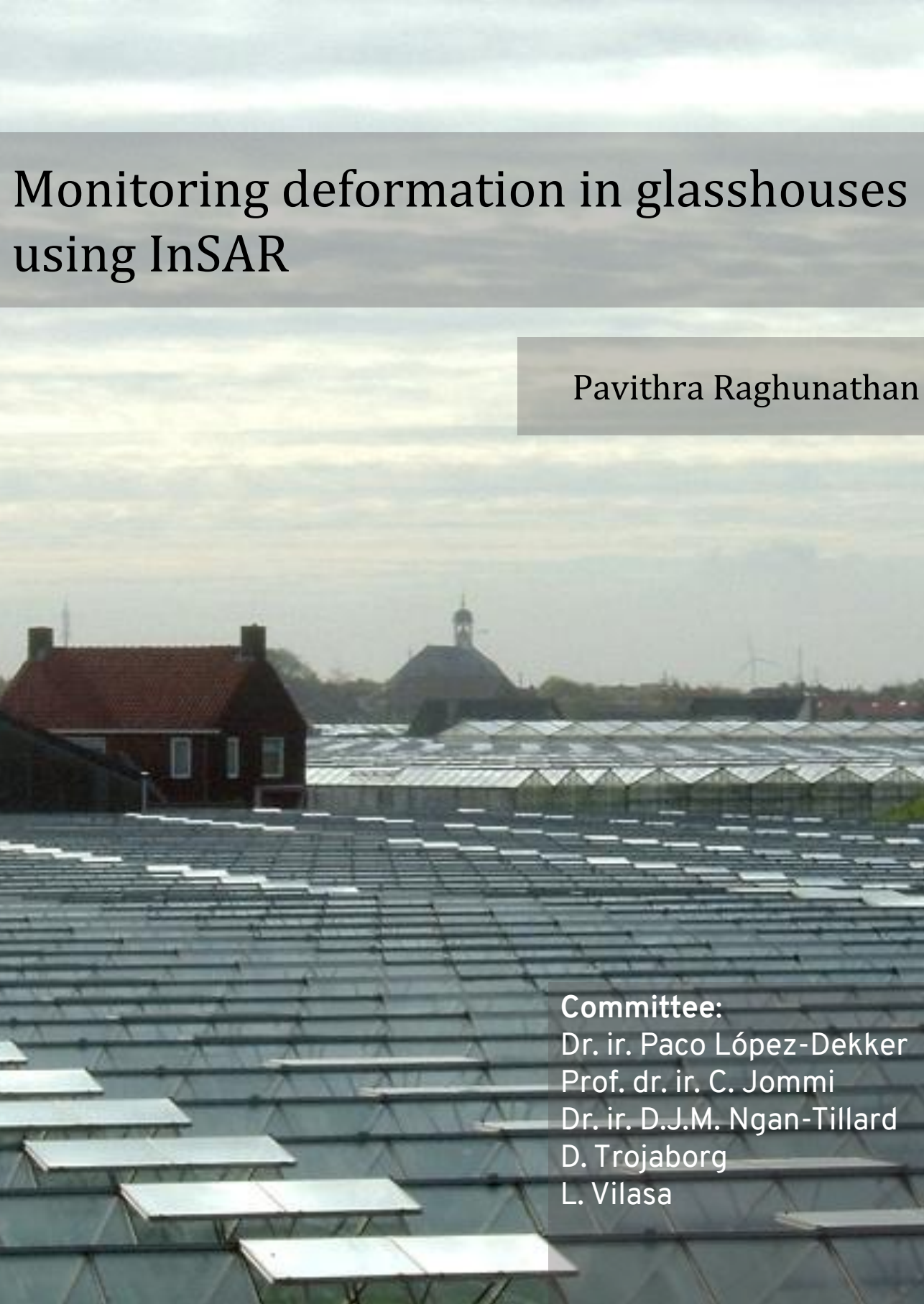

Committee:
Dr. ir. Paco López-Dekker
Prof. dr. ir. C. Jommi
Dr. ir. D.J.M. Ngan-Tillard
D. Trojaborg
L. Vilasa

[This page is left blank intentionally]

Cover page credits:
https://commons.wikimedia.org/w/index.php?curid=130481

MONITORING DEFORMATION IN GLASSHOUSES USING INSAR

by

PAVITHRA RAGHUNATHAN

For the degree of Master of Science in Civil Engineering
(Geoscience and Remote sensing) at the Delft University of Technology

To be defended on 28th October, 2020 at 10 AM.

Faculty of Civil Engineering and Geosciences (CITG) · Delft University of Technology

This thesis was done under the supervision of

Dr. ir. Paco López-Dekker	Principal Supervisor	CITG, TU Delft
Prof. dr. ir. C. Jommi	Supervisor	CITG, TU Delft
Dr. ir. D.J.M Ngan-Tillard	Supervisor	CITG TU Delft
D. Trojaborg (Msc)	Supervisor	Space Data Applications, CGI
L. Vilasa (Msc)	Supervisor	Space Data Applications, CGI

This thesis is confidential and cannot be made public until 28 October 2022.

An electronic version of this thesis will be available at
`http://repository.tudelft.nl/` after the confidentiality embargo is lifted.

ACKNOWLEDGEMENTS

The past ten months has been a very fulfilling experience for me in terms of both technical learning as well as personal growth. I would like to express my deepest gratitude to all those who have been a part of the journey that has enabled me to complete this project. The thesis would not have been possible without my principal supervisor Dr. J.F. (Paco) Lopez Dekker. From being a wonderful teacher for the foundation course in InSAR, to guiding me in this project, his support saw me working on research problems that I otherwise wouldn't have thought I was capable of. I have great admiration for his knowledge and his ability to simplify concepts while teaching.

I would like to thank Dr. Dominique G.M. Ngan-Tillard and Prof. Cristina Jommi for being very supportive in helping me understand geotechnical concepts that govern consolidation and settlement. The validation of my results from a geotechnical perspective would not have been possible if not for their patient guidance, timely support and critical assessment.

I consider myself extremely fortunate to have had the opportunity to work on a project that aligns with my interest in remote sensing as well as my desire to engage in technology that can impact the society and the environment. And for this opportunity, I am very thankful to Ditte Trojaborg for entrusting me with the project. I am very thankful for her guidance in helping me see the larger picture and for motivating me throughout the project. I would also like to thank Luis Vilasa for his overall support, for helping me assimilate Sentinel-1 data and for encouraging me constantly while providing crucial feedback.

I believe that the process of learning is always a continuous journey and I therefore am very grateful to all my teachers in India who have been instrumental in this very rewarding journey. I would like to thank my teachers in primary and high school who nurtured my curiosity in science and for my teachers at the undergraduate school who exposed me to the vast potential of the very empowering tool that remote sensing is. I am very grateful to my ex-colleagues at Skylark Drones Pvt Ltd, the first organisation I was employed in, for entrusting me with challenging projects in UAV remote sensing and for encouraging me to pursue my studies at TU Delft.

Most importantly, I owe everything I am today to my family. My parents have worked tirelessly and have left no stone unturned to provide for my education and my other interests. I am very grateful for the constant support rendered by my grandmother and for the boundless inspiration that I draw from her. I would like to mention a note of thanks to those who have stood by me in their own ways: Raghav Raghunathan, Nihal Mohan, Ria Vijayan and Remya Rajan, thank you for the unending support and kindness.

Pavithra Raghunathan
Delft, October 2020

ABSTRACT

The Netherlands has for long been witnessing problems due to subsidence. While urban infrastructure is mostly safeguarded from differential settlement by deep pile foundations, the same cannot be said about greenhouses. The greenhouses of the Netherlands has enabled the country to become the largest exporter of vegetables, second only to the United States of America. It is imperative that these greenhouses which form the backbone of the agriculture infrastructure of the country, are monitored continuously to minimize unprecedented damage.

This thesis aims to study the feasibility of using time series Interferometric Synthetic Aperture Radar (InSAR) as a means to monitor differential settlement in greenhouse structures. The analysis was primarily done using RADARSAT-2 data. In case of translucent surfaces of greenhouses, it was important to firstly identify the physical targets that are associated to scattering centres. This was done by analysing the statistics of the heights of the scatterers which helps in ascertaining where the radar signal is getting back-scattered from. It was inferred that the persistent and distributed scatterers are primarily identified from objects on the roof and outer walls of the greenhouses.

Moreover, the magnitude of deformation estimated from the scatterers have been corroborated with geotechnical data. It was seen that higher magnitudes of deformation was seen in locations with compressible soil types such as clay and peat close to the ground surface. It was also seen that greenhouse structures are prone to differential settlement when the depths of the piles are insufficient in areas with varying soil types. The effect of thermal contributions has also been studied and it was found that the estimation of thermal expansion does not significantly affect the estimated deformations.

From the study, it is evident that time series InSAR offers an effective means to monitor differential settlements in greenhouses. In order to check for differential settlement in individual greenhouses, it is proposed that a persistent scatter interferometric analysis be done initially and if it is seen that the density of these scatterers is insufficient, the analysis can be followed up with time series interferometry of distributed scatterers. Incorporating multiple track directions of radar data increases the number of greenhouses that can be monitored. Moreover, it was also seen that persistent scatterers were identified from additional greenhouses when Sentinel-1 data was used, despite its poorer spatial resolution. For further study, it is recommended that corner reflectors are used to validate the positions of the targets that are identified as persistent and distributed scatterers.

CONTENTS

List of Figures ix

List of Tables xv

1 Introduction 1
- 1.1 Topic and Relevance . . . 1
- 1.2 Research Aim . . . 2
- 1.3 Outline of the thesis . . . 3

2 Background of subsidence in the Netherlands 5
- 2.1 Surface deformation in the Netherlands . . . 5
  - 2.1.1 Types of subsidence - based on the depth of occurrence . . . 6
- 2.2 Soils and settlement . . . 8
  - 2.2.1 Determination of soil type . . . 9
- 2.3 Safeguarding of buildings in the Netherlands . . . 12
  - 2.3.1 Types of pile foundations . . . 12
  - 2.3.2 Pile foundations in the Netherlands . . . 13

3 Interferometric Synthetic Aperture Radar (InSAR) Remote Sensing 15
- 3.1 Advent of radar remote sensing . . . 15
- 3.2 SAR data acquisition . . . 16
- 3.3 SAR imagery . . . 17
- 3.4 SAR datasets . . . 18
- 3.5 SAR image signature and Geometrical effects . . . 19
- 3.6 Interferometric Synthetic Aperture Radar . . . 21
- 3.7 Interferometric phase contributors . . . 21
- 3.8 Phase Unwrapping . . . 25

4 Multi temporal analysis 27
- 4.1 Time series InSAR . . . 27
- 4.2 Persistent Scatter Interferometry . . . 28
  - 4.2.1 Single master stack - Interferogram configuration and preliminary analysis . . . 29
  - 4.2.2 Selection of Persistent scatter candidates . . . 30
  - 4.2.3 Atmospheric phase screening (APS) . . . 32
  - 4.2.4 Estimation of Parameters . . . 32
- 4.3 Distributed Scatter Interferometry . . . 33
  - 4.3.1 Adaptive Filtering - Multilooking . . . 34
  - 4.3.2 Selection of Distributed scatter candidates . . . 35
  - 4.3.3 Estimation of Parameters - weighted approach . . . 36

4.4 Summary . . . 36

5 SAR Data Processing and Areas Analysed 39
5.1 PS InSAR workflow . . . 40
5.2 DS InSAR workflow . . . 42
5.3 Exporting and visualisation of data . . . 45

6 Results and Discussion 47
6.1 Combined InSAR and Geotechnical analysis - Westland Municipality. . . . 47
6.1.1 Number of Persistent scatterers . . . 47
6.1.2 Number of PSs - Sentinel-1 and Radarsat-2 . . . 50
6.1.3 Deformation estimations from persistent scatterers . . . 50
6.2 Combined InSAR and Geotechnical analysis - Individual greenhouses . . . 54
6.2.1 Schiphol . . . 54
6.2.2 Nieuwerkerk aan den IJssel . . . 57
6.2.3 Greenhouse Westland A . . . 61
6.3 Heights Analysis - Nieuwerkerk aan den IJssel . . . 66
6.4 Heights Analysis - Westland . . . 70
6.4.1 Comparison of PSs with DSs of lower spatial coherence threshold (0.75) . . . 75
6.4.2 Concluding remarks for heights analysis . . . 80
6.5 Thermal signal . . . 83
6.6 Subsidence in Greenhouse 'Westland A' . . . 85

7 Conclusions and Recommendations 87
7.1 Conclusions for the research questions . . . 87
7.2 Recommendations for future work . . . 89

A Appendix 91
A.1 Procurement of Geotechnical data . . . 91
A.2 Supplementary results - Greenhouses facing subsidence . . . 91
A.3 Supplementary results - Heights analysis . . . 94
A.3.1 Ascending track . . . 94
A.3.2 Descending track . . . 94
A.4 Filtering data and computation of PS/DS height statistics . . . 98

References 101

List of Figures

1.1 Agricultural Landscape of the Netheralnds - Wageningen University and Research . . . 2

2.1 Soil types in the Netherlands, De Vries 1994 (based on soil map of the Netherlands 1:50000) . . . 6
2.2 Subsidence map - Bodemdalingskaart (Surface motion map 1.0) - National Centre for Geodesy and Geo-Informatics . . . 7
2.3 Time settlement curve with the settlement components . . . 9
2.4 Cone Penetration test Instrument (Ruwan Rajapakse, 2016) . . . 10
2.5 Correlation between friction ratio, cone resistance and soil type [1] . . . 11
2.6 Illustration of 2.2 correlation between sleeve friction, cone resistance and soil type [2] . . . 12
2.7 Types of pile foundations [3] . . . 13

3.1 Geometry of side looking imaging radars [4] . . . 17
3.2 Geometric effects of foreshortening and lengthening and coverage of a glasshouse in a radar image. . . . 20
3.3 Possible paths of the radar signal with multiple re-bounces inside the glasshouse (neglecting the re-bounces that do not reach the SAR sensor. Note that the radar signal is figuratively represented as straight lines but in reality they are waves.) . . . 20
3.4 Schematic of master and slave image acquisition. . . . 22

4.1 The top row represent a) distributed scatterer and b) persistent scatterer respectively. The bottom row shows the simulations of the phase dispersion where it can be seen that for the distributed scatterer the phase is distributed randomly between $[-\pi,\pi]$ and the persistent scatterer, by virtue of a dominant scatterer within the resolution cell, has a smaller phase dispersion [5]. . . . 28
4.2 Baseline configuration of a single master stack - the images are from Sentinel-1 for the period between January 2017 to December 2018. The horizontal axis shows the time of image acquisition and the vertical axis shows the perpendicular baseline. Image produced from Sarproz software. . . . 30
4.3 Initial mask for the processing of pixels . . . 31
4.4 Schematic representation of SHP's. A window is chosen around the testing pixel p. All the pixels within this window are tested to check if their statistics are the same as p. The pixels which meet the condition are then used for multilooking. Image source [6]. . . . 34

5.1 Three regions of the Netherlands analysed for subsidence in greenhouses. Data source [7] 40
5.2 PS workflow 41
5.3 Reference point chosen from the network of PSC is highlighted in red in the reflectivity map. Greenhouse 'Westland A' is highlighted with an orange boundary. 42
5.4 DS workflow 43
5.5 Spatial plots of amplitude, temporal coherence, spatial coherence and the adaptive mask for Greenhouse 'Westland A' 44

6.1 Number of PSs on greenhouses with Radarsat-2 Ascending track direction - Westland municipality 48
6.2 Number of PSs on greenhouses with Radarsat-2 Descending track direction - Westland municipality 49
6.3 Number of PSs on greenhouses with Radarsat-2 - both track directions - Westland municipality 49
6.4 PSs using Radarsat-2 (L) and Sentinel-1 (R) - Ascending track. It can be seen that the greenhouses containing PSs are different in each case. 50
6.5 Deformation from PSs in Westland - Radarsat-2 Ascending track direction - Note that the region around De Lier in the south east portion shows significant deformation. 51
6.6 One of the PSs showing high deformation rate in the region of De Lier. Note that the scatterer has a temporal coherence of 0.97 and is therefore considered to be very reliable. 52
6.7 High probability of compressible soil types (peat and clay) in the top 10m around the region of De Lier. 52
6.8 High probability of fine sand (incompressible soil layer) in the top 10m around the western portion of the analysis area of Westland. 53
6.9 Persistent scatterers - InSAR Analysis in the area of a greenhouse in Schiphol 54
6.10 Soil profile of a borehole on the road - Schiphol. The location of the borehole is highlighted in green. 55
6.11 Borehole 1 shows the shallow profile and borehole 2 shows a deep soil profile 55
6.12 The soil profile a borehole from the set of linear bore holes highlighted in red 56
6.13 Locations of cone penetration test sites - Schiphol. The site analysed is highlighted in green 56
6.14 Left: Cone Resistance and Right: Friction Number at the site analysed in Schiphol 56
6.15 Soil Profile for Cross section through the greenhouse at Schiphol 57
6.16 Persistent scatterers in Nieuwerkerk aan den Ijssel. Greenhouses A and B are annotated 57
6.17 Boreholes(Red) and Cone Penetration Test Locations(Purple) in Nieuwerkerk aan den Ijssel 58

6.18 Soil Profile(left) and Cone Resistance(center), Friction number(right) graphs for location 1 in Nieuwerkerk aan den Ijssel. The receding (negative) spikes at 20m is possibly indicative of peat or clay soil and it can also be seen in the friction ratio graph below where the same is indicated by a positive spike 58
6.19 Soil Profile(left) and Cone Resistance(center), Friction number(right) graphs for location 3 in Nieuwerkerk aan den Ijssel 59
6.20 Soil Profile(left) and Cone Resistance(center), Friction number(right) graphs for location 4 in Nieuwerkerk aan den Ijssel 59
6.21 Soil Profile for location 2(left), location 5(center), location 6(right) in Nieuwerkerk aan den Ijssel. CPT test data not available in these locations 60
6.22 Cross sectional soil profile through greenhouse A at Nieuwerkerk 61
6.23 Persistent scatterers in and to the north of Greenhouse Westland "A" . . . 62
6.24 Boreholes and CPT test site locations in Westland 62
6.25 Soil Profile for location 1(left), location 2(center), location 3(right) in westland 63
6.26 Soil Profile for location 4(left), location 5(right) in westland 63
6.27 CPT graphs for location 1 in Westland.Left: Cone Resistance and Right: Friction Number 64
6.28 CPT graphs for location 2 in Westland.Left: Cone Resistance and Right: Friction Number 64
6.29 Soil Profile for Cross section through Westland greenhouse A 65
6.30 Histograms of residual heights from pixel scatterers of 0.6 minimum TC for multiple Greenhouses in the Nieuwerkerk Aan Den IJssel Area 68
6.31 Histogram of the residual heights from ground pixel scatterers in the Nieuwerkerk Aan Den IJssel Area - Mean: -0.24m; IQR: 5.916m; Std dev: 5.495m . 68
6.32 Visualization of residual heights for PSs in the region of Nieuwerkerk aan den IJssel 69
6.33 Greenhouse 3 Heights analysis in Westland full Area - Ascending Track Direction - Left: PS, Right: DS 72
6.34 Greenhouse 4 Heights analysis in Westland full Area - Ascending Track Direction - Left: PS, Right: DS 72
6.35 Greenhouse 9 Heights analysis in Westland full Area - Ascending Track Direction - Left: PS, Right: DS 72
6.36 Greenhouse 10 Heights analysis in Westland full Area - Ascending Track Direction - Left: PS, Right: DS 73
6.37 Building 4 Heights analysis in Westland full Area - Ascending Track Direction - Left: PS, Right: DS 73
6.38 Building 5 Heights analysis in Westland full Area - Ascending Track Direction - Left: PS, Right: DS 73
6.39 Building 8 Heights analysis in Westland full Area - Ascending Track Direction - Left: PS, Right: DS 74
6.40 Residual heights of the persistent scatterers for greenhouse 10 (L), investigation of greenhouse's height from field visit (R) 75
6.41 Greenhouse 4 Heights analysis on individual scale - Ascending track direction - Left:PS, Right DS 76

6.42 Greenhouse 8 Heights analysis on individual scale - Descending track direction - Left:PS, Right DS 76
6.43 Greenhouse 9 Heights analysis on individual scale - Descending track direction - Left:PS, Right DS 77
6.44 Left: Reference point for the project – for greenhouse 4 and greenhouse 9. The greenhouse on the left is greenhouse 4 – Image source – Google street view 77
6.45 Site visit images of Greenhouse 4 and 9 77
6.46 PS and DS heights over greenhouse 4. 78
6.47 Layout of the buildings analysed, the reference point is highlighted in red 79
6.48 'Greenhouse Westland A' used for comparison with buildings - Left: PS histogram, Right: DS histogram 79
6.49 Building 1 at Westland - Left: PS histogram, Right: DS histogram 80
6.50 Building 2 at Westland - Left: PS histogram, Right: DS histogram 80
6.51 Persistent scatterers of buildings 1 and 2 80
6.52 Distributed scatterers of buildings 1 and 2 81
6.53 Temporal coherence between image pairs with a single master 83
6.54 Temporal coherence between image pairs with master image in 19-01-2018 (Top) and master image in 30-07-2018 (bottom). Both projects are of Greenhouse Westland A area spanning 2.5 sq km. 84
6.55 Persistent scatterers from descending track for Greenhouse 'Westland A'. Image on the left shows the scatterers without accounting for thermal expansion and the image on the right shows the scatterers when thermal expansion is accounted for. 84
6.56 All scatterers here have been processed with Radarsat-2 ascending track data 86

A.1 greenhouses in Westland with subsidence problems as estimated by PS InSAR analysis 92
A.2 The above greenhouses appear to be in a subsidence risk prone area where estimated subsidence varies from 5mm/year to 15 mm/year 93
A.3 Greenhouse 1 Heights analysis in Westland full Area - Ascending Track Direction - Left: PS, Right: DS 94
A.4 Greenhouse 5 Heights analysis in Westland full Area - Ascending Track Direction - Left: PS, Right: DS 94
A.5 Greenhouse 6 Heights analysis in Westland full Area - Ascending Track Direction - Left: PS, Right: DS 95
A.6 Building 1 Heights analysis in Westland full Area - Ascending Track Direction - Left: PS, Right: DS 95
A.7 Building 10 Heights analysis in Westland full Area - Ascending Track Direction - Left: PS, Right: DS 95
A.8 Greenhouse 7 Heights analysis in Westland full Area - Descending Track Direction - Left: PS, Right: DS 96
A.9 Greenhouse 8 Heights analysis in Westland full Area - Descending Track Direction - Left: PS, Right: DS 96

A.10 Building 4 Heights analysis in Westland full Area - Descending Track Direction - Left: PS, Right: DS 96
A.11 Building 9 Heights analysis in Westland full Area - Descending Track Direction - Left: PS, Right: DS 97
A.12 Building 10 Heights analysis in Westland full Area - Descending Track Direction - Left: PS, Right: DS 97

List of Tables

2.1 Soil type as a function of friction ratio [2] 11
2.2 Soil type as a function of friction ratio [8] 11

3.1 Sentinel-1 and RADARSAT-2 sensor overview 18

5.1 Projects processed. The strict amplitude stability threshold for PS and DS is applied only for the selection of reference point or for APS alone and not for the selection of scatterers themselves. For all projects, this threshold is 0.8. It is therefore not mentioned in the table. 46

6.1 Statistics of scatterers with TC> 0.6 - Greenhouses- Nieuwerkerk Aan Den IJssel -Heights analysis. Greenhouses with greater than 40 points are listed 67
6.2 Statistics of scatterers with TC> 0.6 - Buildings- Nieuwerkerk Aan Den IJssel -Heights analysis. Buildings with greater than 20 points are listed 67
6.3 Statistics of PSs and DSs- Greenhouses – Westland full area analysis - Ascending track direction 71
6.4 Statistics of PS and DS - Buildings – Westland full area analysis - Ascending track direction 71
6.5 Statistics of PS and DS - Greenhouses– Westland full area analysis - Descending track direction 71
6.6 Statistics of PS and DS - Buildings– Westland full area analysis - Descending track direction 74
6.7 Statistics of PSs and DSs for 3 individual greenhouses 76
6.8 The statistics of the PS and DS for Greenhouse 'Westland A' and the two buildings 78

1

INTRODUCTION

In this chapter, a discussion of the scope of the project and its relevance is discussed. The outline of the research objectives is also presented.

1.1. TOPIC AND RELEVANCE

The introduction of agriculture in the Netherlands dates back to 5300 BC [9]. Cultivation was initially practiced on loess and sand. As the population increased in the middle ages, peat areas were exploited for farming and with the advent of technological innovations, wetlands and lakes were drained for cultivation starting from the 16th century. Thus, over centuries, the landscape began to change and by the 20th century, a large part of the arable land in the Netherlands underwent redesigning. A significant part of the Dutch landscape was redesigned in the 20th century by de-watering, land consolidation and reclamation.

The greenhouse industry in the Netherlands have earned the country worldwide reputation for being the largest exporter of vegetables second only to the Unites States of America [10]. By the year 2000, a national commitment to practice sustainable agriculture under the rallying cry of "Twice as much food using half as many resources" was made by the cumulative effort of policy makers, agriculture research organisations and farmers. As of today, these temperature controlled farms have made the Netherlands the top exporter of vegetables like tomatoes, onions, pepper and cucumber among other vegetables and fruits. The dutch greenhouses have also enabled the country to contribute to one third of the global trade in vegetable seeds.

Owing to the presence of soils like peat and clay which are highly susceptible to subsidence [11], urban infrastructure in the Netherlands like buildings, bridges, dykes and other public infrastructure have been continuously monitored for deformation. Efficient monitoring of subsidence is crucial for the maintenance of both urban and agricultural infrastructure. This thesis is an attempt to study the possibility of using radar remote

1

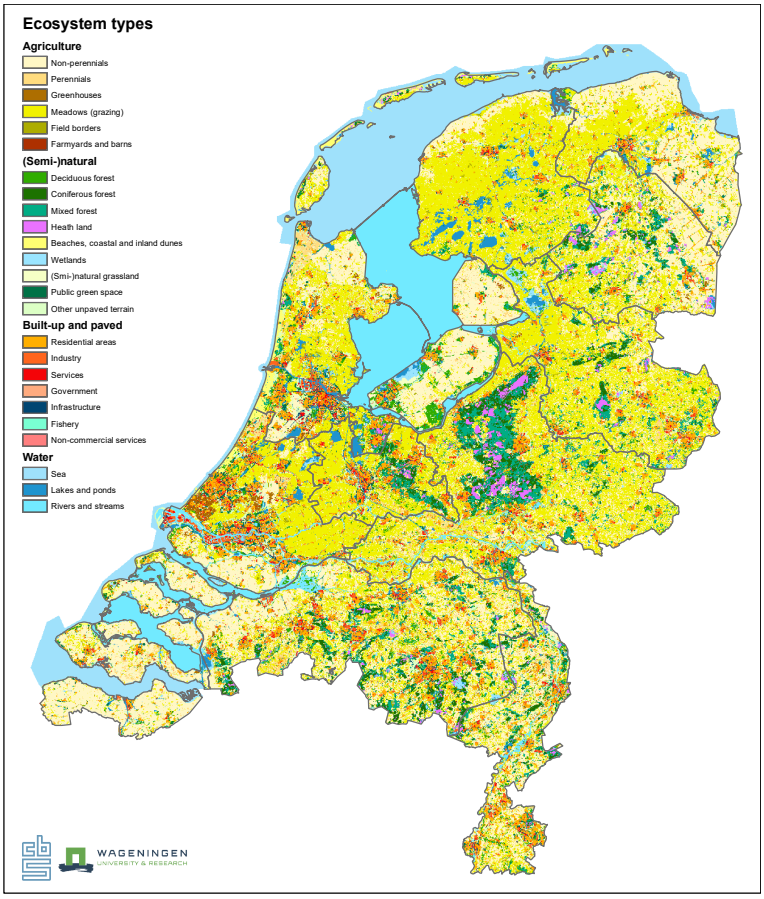

Figure 1.1: Agricultural Landscape of the Netheralnds - Wageningen University and Research

sensing, specifically, Interferometric Synthetic Aperture Radar (InSAR) to measure deformations due to settlement of greenhouses in the subsidence prone regions of Netherlands.

In order to study the effects of differential settlement in greenhouses, primary focus in this thesis has been given to Westland, the greenhouse capital of the Netherlands as can be seen from 1.1. Analysis of two other regions near Rotterdam and Amsterdam have also been conducted to gain a spatial perspective of deformation in greenhouses on different soil compositions.

1.2. RESEARCH AIM

InSAR methodologies have been used to estimate deformation of the built environment as well as natural landscapes. This thesis focuses on the estimation of deformation on

greenhouses using radar satellite data through time series interferometry. The main research question that the thesis aims to answer is:

Can InSAR techniques be used to estimate[1] *deformation in greenhouses?*

A breakdown of the primary research question into sub research questions is done to address different parts of the study that add contextual value to the project. They are broadly enumerated below.

1. In a scene covering greenhouse(s), from what components of the greenhouse is the radar signal getting back-scattered from?

   This question aims to give clarity on what targets are being observed by the SAR sensor. This question is answered by analysing the statistics of the heights of both persistent scatterers as well as distributed scatterers.

2. Can the deformation observed, be explained with the geotechnical properties of the area?

   To address this, the question is further broken down to approach the geotechnical causes of the deformation estimated from the InSAR analysis.

   (a) With the knowledge of the soil profiles of the area, can assumptions be made on the expected subsidence of the area?

   (b) Can the deformation estimated from the InSAR analysis, be explained with the knowledge of the type of foundation of the greenhouse structure?

3. Can contributions of thermal effects be seen in the InSAR estimations of deformation?

   The varying temperature throughout the different seasons in a year may cause expansion and contraction of infrastructure. This research question is aimed at detecting these contributions.

4. How does the methodology of Persistent Scatter Interferometry compare with Distributed Scatter Interferometry for estimation of deformation in greenhouses?

1.3. OUTLINE OF THE THESIS

The thesis is organised into seven chapters including the Introduction chapter. Chapter 2 provides a background of subsidence that is prevalent in the Netherlands with focus on the types of soils and the ways in which buildings are typically safeguarded from settlement. Chapter 3 provides a background of Radar Remote sensing that is used for interferometry and the equipments and technological infrastructure that is in place. Chapter 4 focuses on the background of multi-temporal interferometric methodologies like

[1] The process of arriving at the values the unknown parameters from observations/measurements is referred to as parameter estimation or simply estimation. When there is no other way of finding the correct value of the unknown parameter, except through the set of measurements, estimation refers to the process of determining the unknown set of parameters, from the set of measurements made.

Persistent Scatter Interferometry and Distributed Scatter Interferometry. Chapter 5 outlines the methodology adopted in this thesis for the InSAR analysis of deformation in greenhouses. Chapter 6 presents the results obtained and a discussion of the analysis is provided. Chapter 7 outlines the conclusions of the research questions and presents recommendation for future work.

2

BACKGROUND OF SUBSIDENCE IN THE NETHERLANDS

This chapter aims to provide background into the geotechnical properties and characteristics of soils in the Netherlands which makes it susceptible to subsidence. Since the thesis aims at detecting relative settlements of greenhouses in areas that are prone to subsidence, this chapter also provides some background on soil settlement. Additionally, the mechanisms employed to safeguard urban infrastructure from settlement is also delved into.

2.1. SURFACE DEFORMATION IN THE NETHERLANDS

The Netherlands, having over 26% of its land below the mean sea level [12] and a history of land reclamation, is an example of one of the countries facing the challenge of land subsidence. The Netherlands, has for a long time dealt with implications of land subsidence such as flooding and increased risk of infrastructure failure due to land subsidence. Some studies have projected costs of infrastructure maintenance and destruction mitigation due to subsidence related problems to exceed 5.2 Billion Euros by 2050 [13]. For the effective and strategic intervention of policy makers, infrastructure planning authorities and government stakeholders, land deformation needs to be studied and precisely monitored.

One of the primary causes of subsidence in the Netherlands has been linked with the presence of peat and clay soil. Peat is formed when undecomposed plant remains are deposited under low temperature or high humidity. Throughout the world, peat areas are mostly located near estuaries of major rivers, making the land highly fertile and therefore highly suitable for agriculture. However, this soft soil has to be drained first, a process which causes shrinkage and oxidation of peat which leads to land subsidence [14]. The land subsidence cycle starts over again, when the soil shrinks and gets compacted to an extent where the reduction in volume reaches the level of the water table.

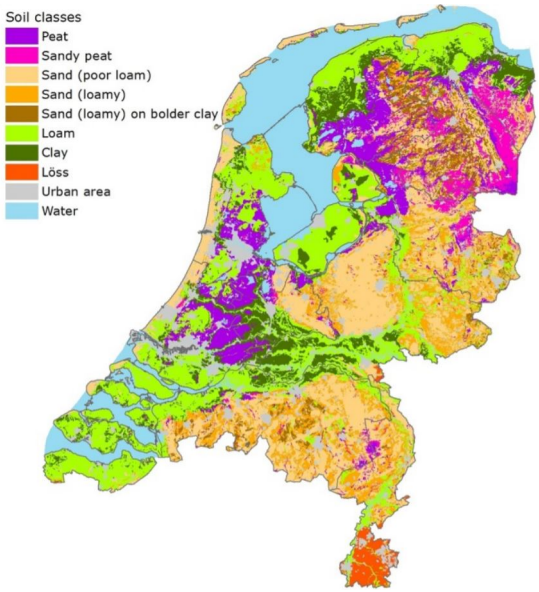

Figure 2.1: Soil types in the Netherlands, De Vries 1994 (based on soil map of the Netherlands 1:50000)

In the province of South Holland, the coastal peat lands are drained to create land that is cultivable. The location of these peat lands can be seen in Figure 2.1.

In the north eastern part of the country, land subsidence in Groningen has occurred due to land compaction arising as a result of gas extraction in the gas fields where commercial gas extraction had started from the early 1960's [15]. Some studies have indicated that the expected subsidence at the heart of the subsidence "bowl" in Groningen would be between 50 to 70 cm by 2080 [16].The study also points that the formation of sink holes has increased in this region. Despite mining operational activity ceasing in the 1970s , the consequence of subsequent pumping of mine water ending in the 1990s is resulting in ground heave causing instability of buildings.

To analyze the aerial extents of Peat soils, Figure 2.1 indicates the extent of this particular type of soil composition. The map shown below is based on 456 typical soil profiles which are assigned to soil map units at the 1:50,000 soil map of the Netherlands.

2.1.1. TYPES OF SUBSIDENCE - BASED ON THE DEPTH OF OCCURRENCE

The major types of subsidences that occur can be classified in different categories like cause of subsidence, extent of subsidence, the depths at which subsidence takes place and the geological layer that is present at the location where subsidence is predominant.

The soil subsidence committee of the Netherlands, established in 1984, Commissie Bodemdaling door aardgasswinning [17] categorizes soil subsidence as 'shallow' and

'deep' based on the depth at which subsidence is occurring. The committee was established to determine the measures that have to be taken to minimize losses due to subsidence related issues.

- Shallow subsidence refers to subsidence that takes place between 0 to 5m depths ie., in the uppermost part of the soil. The cause of subsidence in these layers is attributed to consolidation and settlement from causes such as oxidation of organic material that occurs as a consequence of draining water from peat land.
- Deep subsidence refers to subsidence that takes place at depths exceeding 400m. The primary anthropogenic causes for deep subsidence are extraction of natural gas from the subsurface as can be seen in Groningen and deep excavation in the process of mining minerals in Groningen, Friesland, Overijssel and Limburg.
- The Commissie Bodemdaling door aardgasswinning has also categorized another class of subsidence called 'Middle-deep' subsidence which refers to subsidence between 20m to 400m. Human induced activity of extraction of ground water causes subsidence at these depths.

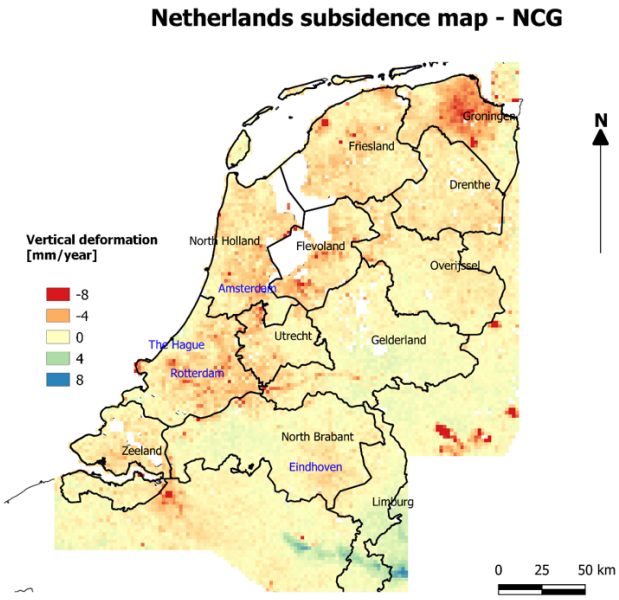

Figure 2.2: Subsidence map - Bodemdalingskaart (Surface motion map 1.0) - National Centre for Geodesy and Geo-Informatics

Several studies have been conducted to estimate the amount of subsidence throughout the Netherlands. One such study is conducted and published by the Netherlands

Centre for Geodesy and Geo-informatics (NCG) with the joint collaboration of universities and research institutes. The datasets used for the analysis are satellite data, GPS and gravity measurements. This subsidence map in Figure 2.2 serves as a reference to ascertain the type, magnitude and scale of subsidence that can be expected before analyzing specific areas of interest. The deformation map represents measurements obtained between 2015 to 2018. Here negative values indicate subsidence and positive values indicate uplift. Each grid represents a 2 X 2 km area.

2.2. SOILS AND SETTLEMENT

Soils deform under stresses and this deformation over time in the vertical direction causes settlement. The magnitude of settlement depends on the type of the soil, the depths of the different soil layers and on time. When soils are subjected to loads, permeable, less compressible soils like sand and gravel, deform fast whereas saturated soils with low permeability like clay and peat experience gradual deformation. This gradual deformation in the vertical direction causes settlement as soft soils are more prone to consolidation. When infrastructure like buildings and roads are constructed, the downward movement of the soil layers due to the weight of the structure causes settlement.

The total settlement is calculated as a sum of three components [18]:

$$S = S_i + S_c + S_s \tag{2.1}$$

where,
S_i is the immediate settlement
S_c is the primary consolidation settlement and,
S_s is the secondary compression settlement.

Immediate settlement does not depend on time and occurs as soon as the load is applied to the soil. On the other hand, primary consolidation settlement and secondary compression settlement is dependent on time and is caused by the expulsion of water from the voids of the soil and thereby the reduction in the volume of the soil pores. For primary consolidation settlement, the rate of the reduction of void ratio is dependent on the rate at which pore water escapes from the soil.

Figure 2.3 depicts time t_p at which the rate of primary consolidation settlement decreases when the effective stresses of pore water pressure and stresses due to the load reach their equilibrium values [18]. After this time, settlement continues through secondary compression where the void ratio decreases as a result of the compression of the soil skeleton itself. This happens when there is no excess pore water pressure but only the effect of the constant vertical effective stress. This time dependent settlement process is applicable for all soil types, however the magnitudes and the rate at which it occurs differs from soil type to soil type. For granular soils like gravel and sand, hydraulic conductivity is large and therefore most of the settlement takes place at the stage of immediate settlement, as soon as the load is applied. Secondary compression is also negligible for these types of soils. On the other hand, for cohesive soils like clay, hydraulic

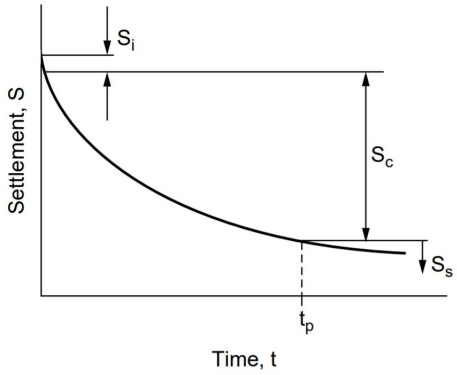

Figure 2.3: Time settlement curve with the settlement components

conductivity is low and settlement is largely dominated by primary consolidation, which can often take many years or even decades (depending on the thickness of the soil layer) and secondary compression.
However, for peat soil and soils with high organic content, settlement is dominated by rapid primary consolidation and prolonged secondary compression [19]. Depending on the soil profile in a given region, a combination of soil types may exist. Therefore, the total settlement is a sum of the settlements of the individual soil layers, each associated to their coefficients of consolidation rates C_α. For a particular cohesive soil type, the secondary consolidation at time t is given by:

$$S_s = S_c + C_\alpha * H * log\left(\frac{t}{t_p}\right) \tag{2.2}$$

where,
S_c is the settlement that has already taken place before secondary compression begins,
C_α is the coefficient of consolidation for the soil type,
H is the height of the soil layer and
t_p is the time at which primary compression reduces and secondary compression begins.

2.2.1. DETERMINATION OF SOIL TYPE

In order to estimate the total settlement that takes place in a time period, it is important to ascertain the individual soil types and the depths of the soil layers.

Soil boring is a geotechnical investigation method where drilling into the surface of the ground is done to extract soil samples. These soil samples are then tested in laboratories to determine the types of soil along the depth of the soil sample.

The Cone Penetration Test is an in situ test that is used to determine the soil type[20]. The mechanical cone penetrometer was developed in the 1930s and in the 1950s, the

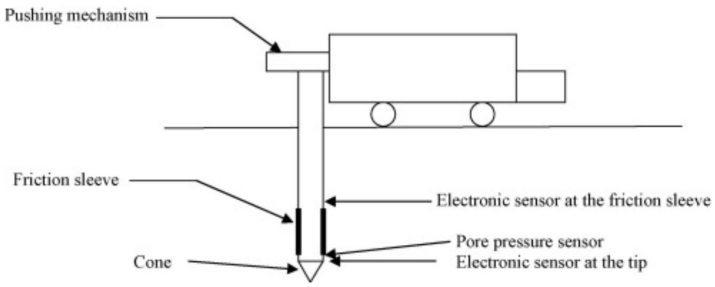

Figure 2.4: Cone Penetration test Instrument (Ruwan Rajapakse, 2016)

sleeve was added to this arrangement by Begemann in 1953 and this became known as the electric cone penetrometer. The tip resistance is determined by the force that is required to push the tip of the cone through the soil and the sleeve friction is the force that is required to push the sleeve through the soil. In the 1980s advancements were made to incorporate piezometer elements leading to the modern piezocone which enables measurement of cone resistance, sleeve friction and pore pressure caused by the cone penetration. A cone, as illustrated in Figure 2.4 is pushed into the soil at a standard rate and the penetrometer is used to measure the penetration resistance. A powerful hydraulic ram is used to generate the required force to enable the cone to penetrate various types of soils like sand, clay and sometimes even soft rock. This allows the test to supply continuous records with depths.

Two quantities that are determined during the test for the purpose of characterising the soil are the cone resistance and friction ratio. Cone resistance represents the ratio of the force measured on the cone tip to the area of the normal projection of the cone tip. The friction ratio is represented as a percentage of the ratio between sleeve friction and tip resistance.

- Cone resistance – Coarse grained soils demonstrate larger values. Cone resistances of magnitude lesser than 0.4 Mpa are indicative of peat soils [1].
- Friction ratio – Incompressible soil layers are characterized by smaller friction numbers. Peat, a compressible soil layer has friction ratio more than 3-4%.

The type of soil as a function of friction ratio proposed by Begemann for the mechanical cone is shown in table 2.1 and values proposed for the electrical con penetrometer by Vos is shown in table 2.2.

The first profiling chart of Begemann in Figure 2.6 shows the gradation of categorising the soil types based on cone resistance and sleeve friction. Robertson and Campanella proposed the gradation for categorising soil depending on the cone resistance and friction ratio for the standard electric friction cone as shown in Figure 2.5.

Table 2.1: Soil type as a function of friction ratio [2]

Soil type	Friction ratio range
Coarse sand with gravel through fine sand	1.2 % - 1.6 %
Silty sand	1.6 % - 2.2 %
Silty sandy clayey soils	2.2 % - 3.2 %
Clay and loam, and loam soils	3.2 % - 4.1 %
Clay	4.1 % - 7.0 %
Peat	>7 %

Table 2.2: Soil type as a function of friction ratio [8]

Soil type	Friction ratio range
Coarse sand and gravel	<0.5%
Fine sand	1.0% - 1.5%
Silt	1.5% - 3.0%
Silty clay	3.0% - 5.0%
Clay	4.0% - 7.0%
Peat	>7 %

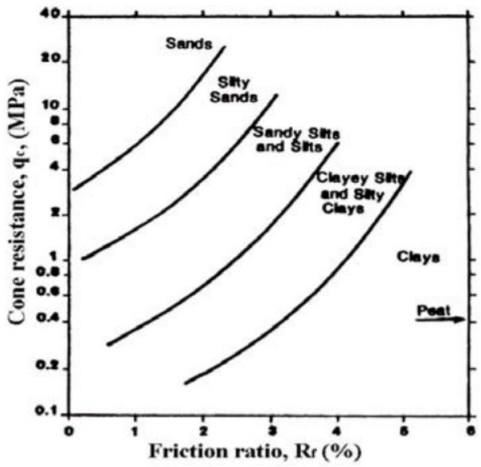

Figure 2.5: Correlation between friction ratio, cone resistance and soil type [1]

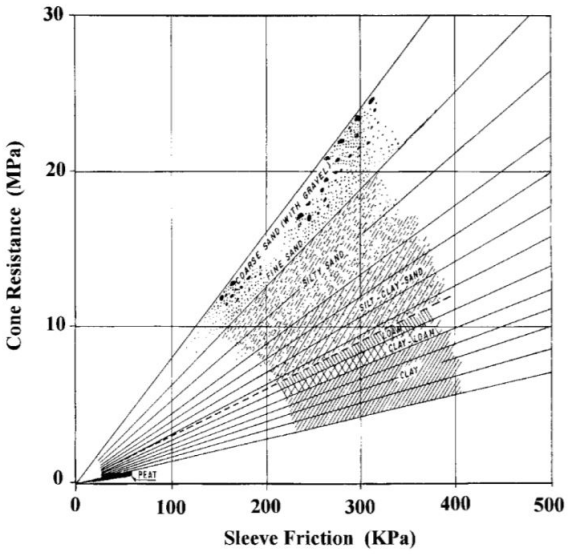

Figure 2.6: Illustration of 2.2 correlation between sleeve friction, cone resistance and soil type [2]

2.3. SAFEGUARDING OF BUILDINGS IN THE NETHERLANDS

To build permanent structures, a sufficient bearing capacity is required for building structures to be supported. In case of soft soils, pile foundations are required to transfer loads through the soft compressible soil layers into the stiff incompressible soil layers in order to provide the necessary bearing capacity.
Pile foundations are foundations where loads are transferred to deeper soil layers by means of piles that can be made of timber, concrete or steel [3]. Some of the cases where pile foundations are adopted are:

- when the loading is uneven or there is no firm strata present at reasonably sufficient depths making raft foundations unfeasible or not economical.
- when strip or spread footings become uneconomical due to firm strata being present at very high depths.
- when pumping of sub soil water is an uneconomical option or timbering to excavations is difficult to allow for the construction of other foundations.

2.3.1. TYPES OF PILE FOUNDATIONS

Depending on the geological conditions of the area such as the type of soil layers through which the pile is inserted through and the depth of the load bearing soil strata, pile foundations as shown in figure 2.7, can be of the following types[3]:

1. End bearing piles: End bearing piles transfer loads through soft compressible soil layers to a hard stratum. Most urban infrastructure like multi storeyed buildings are founded on such piles in order to minimise settlements.

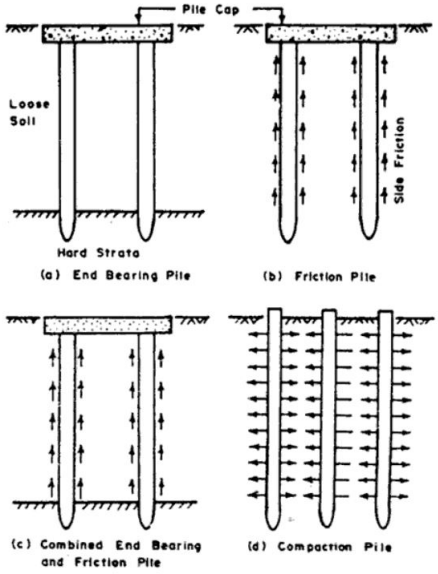

Figure 2.7: Types of pile foundations [3]

2. Friction piles: Friction piles are used in cases where the depth to a hard stratum is very high. In such cases if granular soils are present in the intermediate layers below the surface, then friction piles are used to transfer loads to a depth of a friction-load-carrying material by means of skin friction along the length of the pile.

   In figure 2.7 sub figure (c) shows a pile which transfers the super-imposed load both through end bearing and friction as well.

3. Compaction piles: Compaction piles are used to increase the bearing capacity of compact loose granular soils. Since compaction piles by themselves do not carry load, they can be made be of weaker materials like timber. The pile tube is first driven to compact the soil and is then gradually taken out. Sand is then filled in its place forming a 'sand pile'.

2.3.2. PILE FOUNDATIONS IN THE NETHERLANDS

The method of providing pile foundations to buildings, albeit for small and light structures, in the Netherlands dates as far back as the Roman period where short oak, ash and alder piles were used. As the population increased in the middle ages, there was an increased requirement for more stable foundations. Rotterdam and Amsterdam, two major dutch cities, had building foundations made of single piled beam construction and double piled beam construction respectively, in the later half of the 19th century. As the number of cities began to expand in western Netherlands, it called for more cities to be built with buildings founded by pile foundations. Until 1925 all Dutch foundations were

made of wood [21]. Between 1925 and 1950, most building foundations had wood piles with a concrete upper part. Most heavy infrastructure buildings such as multi-storeyed complexes constructed since 1950, have been founded with concrete piles.

It is noteworthy to mention that most formulas used to calculate the bearing capacity of piles are based on the Cone Penetration Test where correlations are drawn between the cone resistance and the bearing capacity of the pile. Thus piles are designed in such a way that the loads are transferred to incompressible soil layers with the design specifications of requirements based on the CPT tests.

Differential settlement in buildings, including the greenhouses of Netherlands can occur due to multiple reasons. One of the causes may occur when the depth of the piles are insufficient to ensure that loads are transferred to incompressible soil layers with sufficient bearing capacity. Negative skin friction occurs when there is a downward drag acting on the pile if the pile rests on compressible soil layers that can consolidate. Structures with shallow footings and wooden pile foundations in clay and peat soil are susceptible to damage due to subsidence when water table fluctuations occur. Falling of water tables are exacerbated in drier summer months and clay especially is more prone to shrinkage and swelling as a consequence of this [22].

3

Interferometric Synthetic Aperture Radar (InSAR) Remote Sensing

This chapter provides some background on InSAR remote sensing and highlights the components of the phase measured through interferometry.

3.1. Advent of radar remote sensing

The first experiments on electromagnetic waves in the 19th century enabled scientists to understand the application of transmitting and receiving signals to detect targets remotely. In the early 20th century, the first Radio Detection and Ranging (RADAR) device was developed. This milestone development played a key-role in the Second World War allowing military aircraft to detect others through fog and clouds.

The remarkable impact of radar technology on strengthening military and defence forces, propelled technical research in the United States leading to the invention of Synthetic Aperture Radar (SAR) in the 1950s by Carl A. Wiley. Around the same time, researchers at the University of Illinois also independently developed SAR.

The benefits of SAR arises from the creation of a 'synthetic' or artificially extended aperture by means of an antenna on a moving platform. This allows for retrieval of radar signals from multiple returns of the reflected pulse within the synthetic antenna length. The synthetically extended antenna leads to an increase in azimuth resolution in the images produced without having to increase the physical size of the antenna on the satellite [23]. This enables the generation of high resolution radar images which preserve the information of the backscatter from the targets.

The first Interferometric Synthetic Aperture Radar (InSAR) experiment was performed

by Graham et al. in 1974 by means of using two antennas on an aircraft [24]. In 1988, Goldstein used Shuttle Imaging Radar (SIR-B) images to publish the first single antenna repeat pass Digital Elevation Map (DEM) through interferometric processing [25]. Despite the potential of InSAR, decorrelation due to change in terrain reflectivity [26] and the presence of atmospheric water vapour causing delay in radar signals making phase measurements inaccurate, were major limitations to the adoption and scope of applications using InSAR. This remained until methodologies that incorporated multi-temporal InSAR analysis were developed. This is discussed in further detail in chapter 4.

3.2. SAR DATA ACQUISITION

The geometry of the radar imaging system is shown in the Figure 3.1. The satellite flies in the azimuth direction with velocity v with the antenna mounted on it. The radar beam is directed towards the surface. This direction is referred to as the range direction. The radar beam has a look angle θ with respect to nadir. As the radar beam covers positions on the surface that are nearer to the satellite to positions farther away, the look angle is not constant, but increases from near range to far range. The azimuth and range coordinates of the satellite can be projected on the surface leading to ground range and ground azimuth coordinates. The swath width is dependent on the beam angle of the radar system, while the swath length in the azimuth direction depends on the time for which the radar is turned on and together these parameters indicate the footprint of ground coverage of the beam.

The antenna beam width in azimuth direction causes point scatterers on ground to be imaged within the beam for a number of continuous pulses which are transmitted and received. During these pulses, the relative velocity of the point scatterer with respect to the radar changes as a consequence of the motion of the radar. This causes a Doppler like effect. The center frequency of a point scatterer as it passes through the antenna beam is called the Doppler centroid frequency. At zero-Doppler, the beam direction is perpendicular to the flight direction and the doppler frequency is zero. The Doppler centroid frequency of every image is taken, from which the center frequency of the azimuth window is obtained, which is used for azimuth filtering of the data. The raw SAR data products are called level-0 products which have data in the compressed and unfocused form. Various algorithms are then employed to obtain the focused and filtered forms of the images. The focused SAR images thus obtained is referred to as Single-Look-Complex (SLC) images.

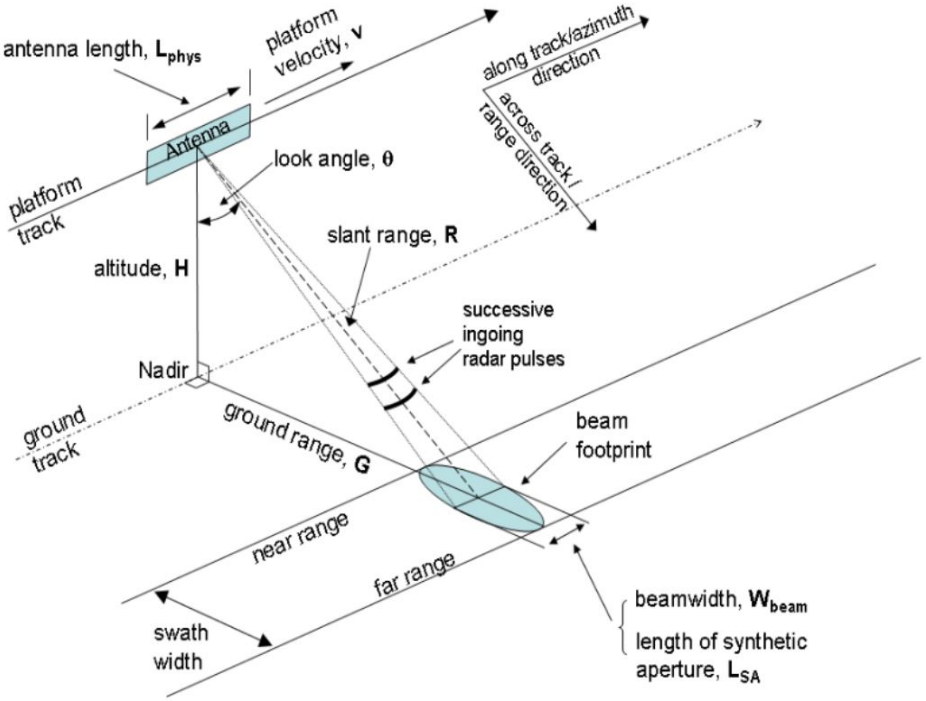

Figure 3.1: Geometry of side looking imaging radars [4]

3.3. SAR IMAGERY

The electromagnetic pulses which are emitted by the radar instrument on board the spacecraft or aircraft are reflected back by some targets on the earth's surface. The distance from the radar instrument to the object on the earth's surface in the line-of-sight (LOS) direction is referred to as the range distance. The Range distance is estimated based on the two way travel time of the pulse. The measured intensity of the received pulse from the target also provides information about the nature of the reflective surface [27], [23]. This includes information information about the physical and electrical characteristics of the surface as it depends on the roughness and di-electric properties of the surface. The intensity is represented by the amplitude A of the signal and the travel time is represented by the phase ϕ. This information is stored in a Real Aperture Radar (RAR) image. The complex phasor P represents the total radar measurement comprised of amplitude and travel time.

$$P = A\exp(i\phi), \tag{3.1}$$

where P represents the sum of all reflections from the terrain of observation, that falls within the pixel. The complex phasor P is stored as a two dimensional image where $\mathrm{Re}(P) = A\cos(\phi)$ and $\mathrm{Im}(P) = A\sin(\phi)$. The phase of each point in the SLC is represented

by:

$$\phi = \arctan\left(\frac{\mathrm{Im}(P)}{\mathrm{Re}(P)}\right), \tag{3.2}$$

where, phase ϕ represents the phase difference between the emitted wave (from the radar instrument) and the returned wave (from the surface of the Earth). The phase is wrapped in the interval $[-\pi, \pi]$, because the total number (integer) of phase cycles is not known. The phase is affected by contributions due to the range, atmosphere, scattering and noise. The phase of a target can be expressed in terms of the distance from the sensor as:

$$\phi_{range} = \frac{4\pi}{\lambda} R, \tag{3.3}$$

where R is the distance of the target from the sensor.
Because different targets have different scattering properties, each pixel can display different scattering characteristics.

3.4. SAR DATASETS

Table 3.1 shows the SAR sensor overview of the two data products used in the thesis, RADARSAT-2 and Sentinel-1. RADARSAT-2 data is commercially available globally but is free to access for the Netherlands through the Netherlands Space Office [28]. Sentinel-1 can be downloaded from the Copernicus Open Access Hub [29].
The resolution depends on the bandwidth in range and azimuth direction. The pixel spacing differs from the resolution due to re-sampling processes and represents the distance between adjacent pixels in an image. Both RADARSAT-2 and Sentinel-1 operate in C-band.

The polarization of the wave refers to the orientation of the electromagnetic wave. The radar instrument emits the signal either vertically or horizontally. Depending on how the signal interacts with the target, the reflected signal is received by the radar instrument in a particular polarisation vertically or horizontally. The radar sensors used for the thesis are either in quad-polarization or dual polarization. The first letter denotes the orientation of the emitted signal and the second letter denotes the orientation of the received signal.
The revisit time is a measure of the temporal resolution of the data product. Note that table 3.1 shows the orbit repeat of the satellite.

Table 3.1: Sentinel-1 and RADARSAT-2 sensor overview

Satellite	**Beam Mode**	**Resolution (Rng x Azi) [m]**	**Pixel Spacing (Rng x Azi) [m]**	**Wavelength [cm] (band)**	**Polarization**	**Orbit Repeat [days]**
Sentinel-1	Interferometric Wide Swath	2.7 x 22 to 3.5 x 22	2.3 x 14.1	5.6 (C-band)	HH,VV, HV, VH	12
RADARSAT-2	Extra-Fine	3.1 x 4.6	2.7 x 2.9	5.6 (C-band)	HH, VV	24

3.5. SAR IMAGE SIGNATURE AND GEOMETRICAL EFFECTS

The glass panels of most greenhouses are supported on trusses. The image signature obtained from these structures can appear differently as two possible scenarios. Which are:

- The roof of the glasshouse is opaque to the radar signals as depicted in figure 3.2.
- The roof is semi transparent to radar signals leading to some beams reflecting and others passing through as depicted in figure 3.3.

Note that the radar beams are shown here figuratively as straight rays but in reality they are waves that can get reflected and can propagate. Due to the side looking nature of the sensor and the variation of terrain on ground, the surface is not completely imaged by the SAR. Some parts of the structures on ground can fall in the shadow region of the radar beam and therefore will not be imaged [30]. The solid orange line in figure 3.2 represents a single line in a SAR image. The dotted lines represent the perpendicular wave fronts separated by the spatial resolution of the sensor. The slope AB appears as A'B' which is foreshortened since it faces the sensor and the slope BC appears as B'C' which is lengthened and appears longer than A'B' even though AB and BC may be of equal lengths. This is because the CD slope faces away from the sensor. If the inclination of the slope CD is lesser than the incidence angle of the radar signal with respect to the vertical, then the slope can even fall in the shadow region.

The incidence angle is a crucial parameter on which the sensitivity to deformation depends, since the deformation is detected for movements along the line-of-sight of the incoming signal. The sensor is not sensitive to deformation which is perpendicular to the direction of signal propagation.

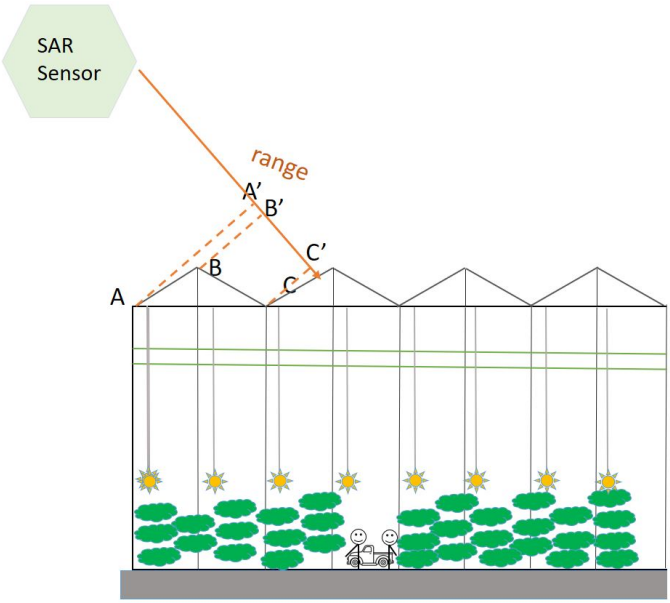

Figure 3.2: Geometric effects of foreshortening and lengthening and coverage of a glasshouse in a radar image.

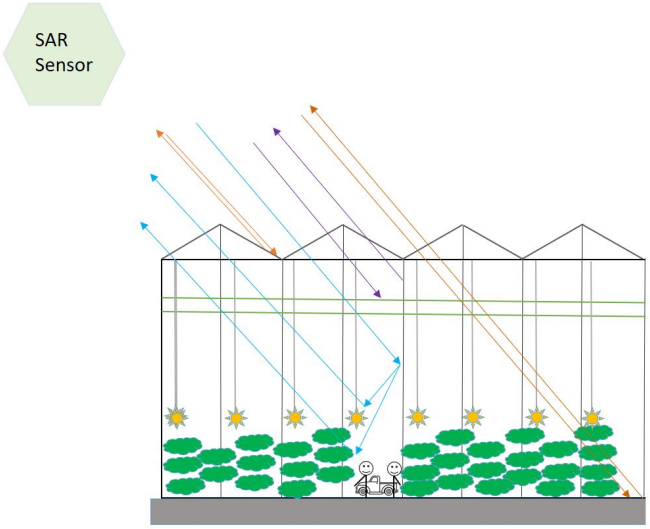

Figure 3.3: Possible paths of the radar signal with multiple re-bounces inside the glasshouse (neglecting the re-bounces that do not reach the SAR sensor. Note that the radar signal is figuratively represented as straight lines but in reality they are waves.)

3.6. INTERFEROMETRIC SYNTHETIC APERTURE RADAR

One of the primary limitations of SAR (also in RAR - Real Aperture Radar) is in the inability to measure angles. Targets on the surface can be differentiated based on their range distance to the radar sensor, but not based on the differences in the angles. In order to distinguish targets having the same range and interpret information, two SAR images can be combined to form a complex image called an interferogram. The interferogram displays phase differences between two aligned SAR acquisitions of the same area. The technique used to obtain interferograms is known as Interferometric SAR, or *InSAR*. The complex interferogram is obtained by the multiplication of the phasor of one image called the master [1] image, with the complex conjugate of the other image, called the slave image [23]. The pixel coordinates in range are often referred to as the "sample" and the pixel coordinates in azimuth are referred to as "line". The interferogram between two radar images i and k is expressed as

$$\text{Img}_{i,k}(s,l) = \text{Img}_i(s,l).\text{Img}_k^*(s,l), \tag{3.4}$$

where $\text{Img}(s,l)$ denotes the complex value of the image at the coordinates of its sample and line. The product is applied to every pixel where * denotes the complex conjugate. The interferometric phase between the images i and k is expressed as

$$\phi_{i,k} = \phi_i(s,l) - \phi_k(s,l). \tag{3.5}$$

By combining equation 3.5 and equation 3.3, the interferometric phase in terms of the range to the target and pixel coordinates is obtained as

$$\phi_{i,k}(s,l) = \frac{4\pi}{\lambda}[R_i(s,l) - R_k(s,l)]. \tag{3.6}$$

3.7. INTERFEROMETRIC PHASE CONTRIBUTORS

The interferometric phase of a target P with respect to a reference point O can be better understood by figure 3.4a. The target P is at a distance of Δx from O and at a height of Δh. S_i is the location of the satellite when the master image is taken and S_k is its position when the slave image is taken. The relative positions between the two positions of the satellite measured along the direction normal to the reference slant range is called the Normal Baseline represented by B_n in figure 3.4a. In interferograms, longer baselines would typically generate interferograms with higher frequency of fringes.
The interferometric phase can be expressed as a sum of all of its contributors as: [31],[32],[33]

$$\phi_{i,k} = \phi_{flat} + \phi_{topo} + \phi_{orbit} + \phi_{def} + \phi_{atm} + \phi_{scat} + \phi_{noise}, \tag{3.7}$$

where
$\phi_{i,k}$: interferometric phase
ϕ_{flat}: flat earth phase ϕ_{topo}: topographic phase contribution
ϕ_{orbit}: phase error due to errors in orbit information

[1] The terms 'master' and 'slave ' have been used in the current thesis for lack of alternate standardised terminologies. The author is aware that the InSAR community needs to find suitable alternatives for these terms.

ϕ_{atm}: phase affected by atmospheric conditions
ϕ_{scat}:phase contribution related to the scatterer's electrical properties
ϕ_{noise}: total noise in phase.

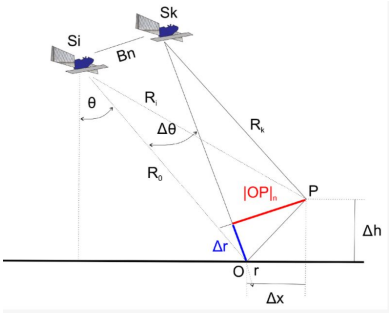

(a) Acquisition geometry for interferogram formation. S denotes the satellite position, O is the reference point and P is the target. Image source from [34]

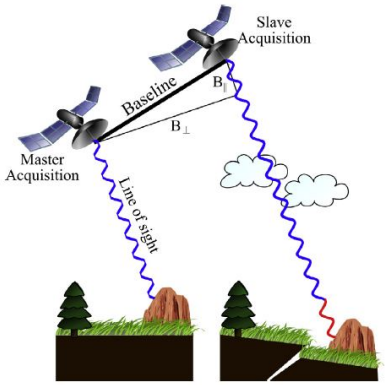

(b) Illustration of baselines in acquisitions of master and slave image. Image source from [33]

Figure 3.4: Schematic of master and slave image acquisition.

The individual contributors are explained below:

1. Flat earth phase (ϕ_{flat}) is due to the shape of the Earth, which can be calculated using the satellite orbits and the geodetic datum. The flat earth phase is considered because most SAR imaging software focus images with a flat earth assumption. The flat earth phase is:

$$\phi_{flat} = \frac{4\pi}{\lambda}.B_{||}, \tag{3.8}$$

where $B_{||}$ is the parallel baseline for each pixel [35]. The parallel baseline is illustrated in figure 3.4b.

The flat earth phase can also be expressed as

$$\phi_{flat} = \frac{4\pi}{\lambda}\frac{B_n}{R_k}\frac{\Delta r}{\tan\theta}, \tag{3.9}$$

where Δr is the change in range of the target between the two acquisitions and θ is the incidence angle. The flat earth phase depends on the slant range of the target P and not on its height. Since the flat earth phase does not carry useful information it is simply removed.

2. Topographic phase(ϕ_{topo}) is the phase component of the interferogram which is due to the topography above the reference ellipsoid and it is proportional to the perpendicular baseline and expressed as [27]:

$$\phi_{topo} = \frac{4\pi}{\lambda} \frac{B_{\perp}}{R_k \sin\theta} \Delta h, \tag{3.10}$$

where $B_{\perp}$ is the perpendicular baseline.

The topographic phase component shows that the interferograms are sensitive to topography which is what enabled the production of digital elevation maps from Interferometry [24]. The sensitivity of the interferometric phase towards topography can be quantified using 'height of ambiguity'. The height of ambiguity, Δh_a is the height that causes a phase change of 2π. It is quantified as

$$\Delta h_a = \frac{\lambda R_k \sin\theta}{2B_n}. \tag{3.11}$$

Highlighting the effect of equation 3.10 in the current context, it is important to note the role of the interferometric baseline B_n in height estimation. A large normal baseline reduces the height of ambiguity. However, there is a drawback to high baselines which can cause decorrelation in the interferometric phase. The concept of decorrelation is discussed further while elaborating ϕ_{noise}.

3. Deformation phase (ϕ_{def}) is the phase induced due to deformation of the target and it is measured along the line-of-sight direction. The deformation of the target P in vector form in the time interval between acquisitions of images can be expressed as

$$\vec{d} = \delta\vec{x} + \delta\vec{h}. \tag{3.12}$$

The phase induced as a result of this deformation can be expressed as [27]

$$\phi_{def} = \frac{4\pi}{\lambda} |\vec{d}| = |\delta\vec{x}| \sin\theta + |\delta\vec{h}| \cos\theta, \tag{3.13}$$

where θ is the incidence angle of the radar signal.

The interferometric phase is highly sensitive to deformation since a displacement of half a wavelength causes a phase change of 2π. From equation 3.13, it is evident that it is not possible to reconstruct the the direction of displacement with a single acquisition geometry. Also, a displacement of the target in a direction perpendicular to the slant range would remain undetected.

4. Atmospheric phase (ϕ_{atm}) is the phase contributed due to difference in atmospheric conditions over the area of analysis during acquisition of master and slave images. Water vapour can delay radar signals and cause biases in the InSAR phase. The atmospheric phase of radar acquisitions can consist of the tropospheric part and the ionospheric part. The tropospheric part is generally referred to as the Atmospheric Phase Screen (APS) for C-band (4-6 GHz) and lower frequency radars [33].

The tropospheric delay can be split into hydrostatic delay and wet delay. The hydrostatic delay is generally constant at around 2.3m. The wet delay is more difficult to determine although the maximum value is relatively low at around 0.35m. In case of ionospheric delay, longer wavelengths have larger delay than shorter wavelengths. In case of L-band (1-2 GHz) and lower frequency radars, changes in the Total Electron Content (TEC) of the ionosphere can affect the interferometric phase. Since the hydrostatic delay and ionospheric delay are largely constant, they get cancelled in the interferograms.

5. Scatterer phase (ϕ_{scat}) is the phase contribution due to the change in scaterrer's electrical characteristics between the acquisitions of the images. This contributor is affected by the changes in the dielectric properties of the scatterer and is exploited in studies pertaining to estimating penetration depth, water equivalent of dry snow and soil moisture [36].

6. The interferometric noise (ϕ_{noise}) is linked to coherence. One of the primary limitations to InSAR is that it works well only when there is good correlation between SAR images. Correlation between SAR images depends on the nature of targets captured in the SAR image pixels. Decorrelation is caused when images lose coherence. The coherence ranges from 0 to 1 and it can be broken into five decorrelation terms as formulated as [23], [37].

$$\gamma_{tot} = \gamma_{temp} * \gamma_{geom} * \gamma_{DC} * \gamma_{therm} * \gamma_{proc}. \tag{3.14}$$

   - Temporal decorrelation (γ_{temp}) occurs when there is a change in the surface between the acquisitions of the images.The total phase of two radar acquisitions at time $t1$ and $t2$ are:

$$\begin{aligned} \phi_{t1} &= \phi_{geom,t1} + \phi_{scat,t1} + \eta_{t1}, \\ \phi_{t2} &= \phi_{geom,t2} + \phi_{scat,t2} + \eta_{t2}, \end{aligned} \tag{3.15}$$

     where ϕ_{geom} is the phase component due to the viewing geometry.
     ϕ_{scat} is the phase component due to all the scatterers in a given resolution cell. For a coherent interferogram (where the interferometric phase is $\phi = \phi_{t2} - \phi_{t1}$), ϕ_{scat} at $t1$ and $t2$ should be very similar, and for an ideal coherent scatterer it should be equal. The difference between $\phi_{scat,t1}$ and $\phi_{scat,t2}$ leads to temporal decorrelation [23].

   - Geometric decorrelation (ϕ_{geom}) is related to the horizontal separation between two satellite orbits. It occurs when there is a difference in the viewing geometry in the image acquisitions. This happens as a result of the incidence angle being different. When this happens, the overlapping portion of the images get reduced in the data frequency spectrum and the decorrelation in the non overlapping portions causes geometric decorrelation.The geometric

decorrelation is therefore dependent on the amount of spectral shift and is quantified as [23]

$$|\gamma_{geom}| = \begin{cases} B_{\perp,crit} - B_{\perp} & |B_{\perp}| \leq B_{\perp,crit}, \\ 0 & |B_{\perp}| > B_{\perp,crit}. \end{cases}, \tag{3.16}$$

where critical baseline, $B_{\perp,crit}$ is the baseline which would result in a spectral shift equal to the bandwidth, which depends on the wavelength, the angle of incidence and the topographic slope.

- Doppler centroid decorrelation (γ_{DC}) is caused by the difference in Doppler centroid frequencies of the master and slave images. It is similar to geometric decorrelation except that it occurs in the azimuth direction.
- Thermal decorrelation (γ_{therm}) is caused due to the thermal noise within the radar and is instrument dependent.
- Processing decorrelation (γ_{proc}) occur during the processes of the interferogram formation, for example in stages of interpolation and co-registration (a process of the alignment of SAR images on a pixel by pixel basis).

3.8. PHASE UNWRAPPING

As mentioned briefly in section 3.3, interferometric phase is wrapped between $-\pi$ and π and the phase ambiguity is unknown. The unknown absolute phase is represented as ϕ which is formulated as

$$\begin{aligned} \phi_N &= \frac{-4\pi R}{\lambda} + \phi_{noise} \\ \phi_N &= 2\pi a + \phi_{noise} \end{aligned} \tag{3.17}$$

where, R is the range difference, a is the ambiguity which is the unknown number of phase cycles of 2π. The wrapped phase is converted to the absolute value of the phase signal through a process called phase unwrapping. The phase unwrapping process is a difficult stage in interferometric processing due to variations in temporal and spatial decorrelation and also, variable noise. In case of interferograms produced from images that are highly coherent, the process of unwrapping is not very difficult and problems arise when there is poor coherence. The unwrapped phase is defined as the integral of the phase derivative starting from a point whose unwrapped phase is zero (reference point) [38], formulated as:

$$\begin{aligned} \phi_N &= \int_{m=0}^{N} \phi' \mathrm{dm}, \\ \phi_0 &= 0. \end{aligned} \tag{3.18}$$

Where, ϕ_0 is called the reference point, ϕ_N is the end point, m is the variable of integration and ϕ'_m is the phase derivative.
During the process of phase unwrapping, for a given pixel taken under consideration, it

is assumed that none of the surrounding pixels can have a phase gradient beyond the $[-\pi,\pi]$ interval. However, if it is found that this is not the case, a smoothness criterion is imposed through which a cycle of 2π is either added or subtracted to the phase gradient. Thus the unwrapped true phase is obtained by starting from the reference point and proceeding to all the pixels by summing the phase gradients along each path. The limitation here is that if one of the phase gradients is unknown, it will introduce an error in the successive pixels along the path. For 2-D and 3-D phase unwrapping, there exist many path dependent and path independent algorithms.

In case of multi-temporal InSAR analysis, which is discussed in further detail in the chapter 4, phase unwrapping is often solved using a pre-defined kinematic behaviour in time of the area of interest. Thus, a-priori information about the possible deformation behavior is beneficial. For detailed explanations, the reader is requested to refer to [23].

4

MULTI TEMPORAL ANALYSIS

This chapter presents a background of multi-temporal InSAR methodologies. Specifically, the methodologies of Persistent Scatter Interferometry (PSI) and the approach of using Distributed Scatterers. The processing steps involved in both approaches are explained with reference to the software used in this thesis [39].

4.1. TIME SERIES INSAR

The process of using InSAR to study deformation or topography requires accurate delineation of the signal of interest from the other components of the phase. Separating the other signal/noise components from the signal of interest is difficult to perform when single interferograms are used. This is due to temporal and geometric decorrelation that results in large scattering noise in the interferograms. Moreover, in case of deformation monitoring where the aim is to detect deformation in the order of millimeters, atmospheric phase (ϕ_{atm}) makes it difficult to distinguish the signal from atmospheric effects [6].

Since atmospheric effects are mostly uncorrelated temporally, a stack of interferograms (as opposed to single interferograms) can filter out atmospheric disturbances by temporal averaging [23]. One of the distinct aspects about the atmospheric phase is that it has a strong correlation in space (over an area of a few square kilometers) and these spatio-temporal characteristics enable its separation from other signals like deformation which may be correlated both temporally and spatially.

The two broad ways in which time series InSAR has been developed are based on the manner in which the pixels of interferograms are treated. On one end, pixels having high signal-to-noise ratio (SNR) are isolated and on the other end, a processing scheme is employed to process multiple pixels (despite them being affected by decorrelation) to filter useful information. These two branches of time series analysis have lead to the development of two broad classes of pixels: one is the persistent scatterers (PS) and the other

is the distributed scatterers (DS) as shown in figure 4.1. These are further elaborated in this chapter.

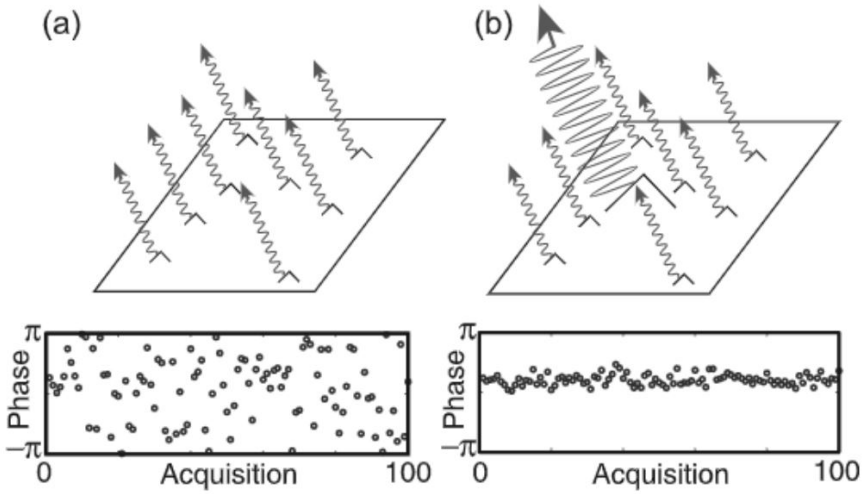

Figure 4.1: The top row represent a) distributed scatterer and b) persistent scatterer respectively. The bottom row shows the simulations of the phase dispersion where it can be seen that for the distributed scatterer the phase is distributed randomly between $[-\pi, \pi]$ and the persistent scatterer, by virtue of a dominant scatterer within the resolution cell, has a smaller phase dispersion [5].

Although there exist other scattering models that make use of scatterers apart from PS and DS, they are not discussed in the scope of this thesis. The reader is requested to refer to [6] for a brief overview of these techniques.

4.2. PERSISTENT SCATTER INTERFEROMETRY

The Persistent Scatter Interferometry time series methodology was first developed by Feretti et al., [31]. This technique uses persistent scatterers which are scatterers that are identified by their high stability in their amplitude of backscatter. The radar measurement of the resolution cell is predominantly affected by a strong reflecting object while other scatterers of the resolution cell only contribute to noise, which is called 'clutter'.

As mentioned in section 3.3, the phase measurement of each pixel is a result of the coherent sum of contributions from all the scatterers within the resolution cell [6]. The distribution of the scattering centres within the resolution cells of the SAR images directly impacts the degree of decorrelation. In the case of an ideal PS, where there is just one stable point scatterer within the resolution cell, the decorrelation would be zero. In reality though, there is never zero decorrelation but some scatterers do behave like PS and their decorrelation phase variation is small. Most PS have scattering centres that are man-made structures and therefore the PSI technique works well in urban areas. In case of areas with natural vegetation, rocks and boulders can be PS [6]. PS are therefore not

affected by baseline decorrelation. In the PSI methodology, a single master stack (stack of images where interferograms are formed by combinations between a single master image and the remaining other images) can be formed even if the baselines are longer than the critical baseline [33].

The PSI algorithm has the following main processing steps [33], [6], [37]:

1. Selection of the single master stack
2. Selection of persistent scatter candidates (PSC)
3. Atmospheric phase screening
4. Estimation of parameters (deformation, height) with the final Persistent scatterers.

These main processing steps are discussed briefly in the sections to follow.

4.2.1. SINGLE MASTER STACK - INTERFEROGRAM CONFIGURATION AND PRELIMINARY ANALYSIS

The interferogram configuration defines the combination of interferograms from which the phase time series is estimated. For the PSI methodology, a single master stack configuration is used. Figure 4.2 shows the perpendicular baseline of the image pairs with all images having a common master image as its pair. The master image is chosen at the barycentre of the distribution of temporal and normal baseline [40]. This is done to maximize the stack coherence.

The remaining images in the stack are the slave images of the interferograms. These slave images, along with the master image, need to be co-registered in order to process the stack of images. Co-registration is the process of aligning all the images on a pixel by pixel basis. Alignment of images can be done based on matching correlation windows or by means of a DEM. DEM based co-registration works well in areas with steep or varying topography. In the case of matching correlation windows, the cross correlation between squared amplitudes are used to compute the shift between two images. The shift is given by the peak of the cross correlation in both range and azimuth directions. Sub pixel shifts are accounted for after oversampling of the images which also avoids aliasing. The software Sarproz, also has a provision for co-registration based on orbit data if precise orbit information is available.

For the PSI analysis, an initial mask of points is selected. This selection is made by computing the local maxima around the neighbourhood of every pixel to select visible peaks from the image of the average amplitude of all images. This averaging operation suppresses noise and highlights the targets that have stable amplitude throughout the time span of the dataset acquisition. Figure 4.3 shows the reflectivity map (average amplitude map) and the selection of the points as the initial mask. The figure contains the scene of a greenhouse in the region of Westland which is henceforth referred to as 'Greenhouse Westland A' in the thesis.

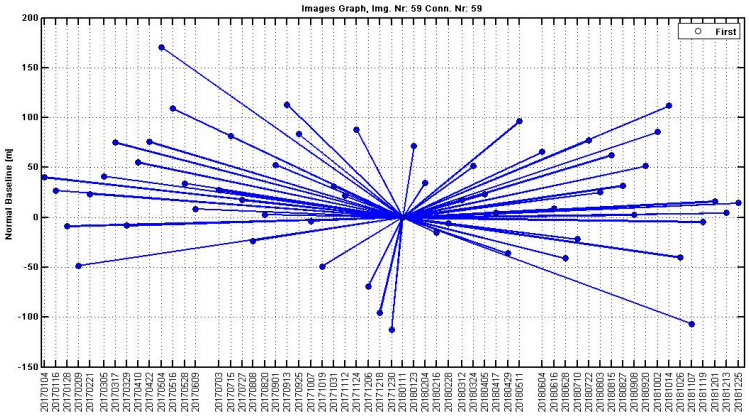

Figure 4.2: Baseline configuration of a single master stack - the images are from Sentinel-1 for the period between January 2017 to December 2018. The horizontal axis shows the time of image acquisition and the vertical axis shows the perpendicular baseline. Image produced from Sarproz software.

The external elevation model required for the analysis can be provided by a DEM and in the case of the study in this thesis, the SRTM (Shuttle Radar Topography Mission) DEM is used [41].
The last stage of the preliminary analysis is the GCP (Ground Control Point) selection. A reference point is used to tie the line and sample coordinates of the reflectivity map (and therefore the entire stack of master and slave images) to the latitude and longitude of the point as visualised in Google Earth. In this thesis, objects that are clearly identifiable both in the reflectivity map as well as Google Earth's aerial imagery have been used as GCPs.

4.2.2. SELECTION OF PERSISTENT SCATTER CANDIDATES

In most PSI methodologies, persistent scatterers are detected in two stages [6]. The first stage is where Persistent Scatter Candidates (PSC) are used to eliminate the atmospheric phase. The second stage is where further persistent scatterers may be added to the network to estimate the parameters of interest, like heights and deformation.

Persistent scatter candidates, as the name suggests, are candidate pixels for the final persistent scatterers that are selected based on a pre-selection criteria. The selection is based on a metric called 'amplitude dispersion' which was first defined by Feretti et al., [31] as the ratio of standard deviation of the amplitude values to the mean of the amplitude values, calculated as:

$$D_A = \sigma_A / \mu_A, \tag{4.1}$$

where D_A is the value of the amplitude dispersion, σ_A is the standard deviation of the amplitude and μ_A is the mean of the amplitude values. This metric is used to identify stable scatterers from unstable scatterers since the change in phase for stable scatterers is affected to a lesser extent by noise as compared to unstable scatterers. Therefore the stability of the amplitude is used as a proxy for the scatterer phase variability in the selection of the PSC's. Since this is a normalized index, values can range between 0 and

(a) Reflectivity map visualised by the computation of the average of the amplitudes of all images in the data-stack, in this case of 28 Radarsat-2 images covering a scene with greenhouse 'Westland A'

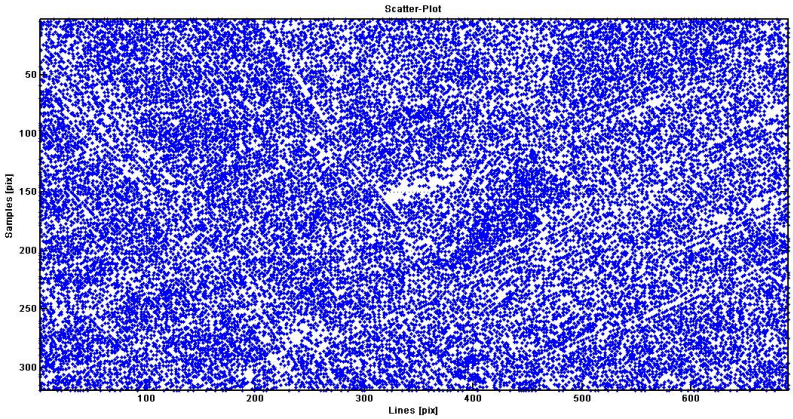

(b) Local maxima of amplitude points which will be analysed in the steps of PSI and DSInSAR to follow

Figure 4.3: Initial mask for the processing of pixels

1. Lower values of amplitude dispersion are indicative of stronger targets. Within the domain of the Sarproz software, this metric is called 'Amplitude stability index', its value is $1 - D_A$ and therefore higher values of the amplitude stability index are indicative of stronger targets.

At the pixel locations of the persistent scatterer candidates, the interferometric phase values are used to estimate it's height and deformation velocity based on a range of minimum and maximum values for the heights and a pre-defined temporal model of deformation which is used for unwrapping phase in the time domain.

4.2.3. ATMOSPHERIC PHASE SCREENING (APS)

Residual phase values are obtained after the phase change due to height and due to deformation are removed from the interferometric phase. This include the phase contribution due to atmosphere and noise. The scatterer phase change can be neglected for PSCs [33].

APS estimation is done using the unwrapped data from the PSC [6]. The interferograms of the PSI technique are obtained from the single-master stack and the atmospheric phase of the master image can be estimated by the average of the residuals since all the interferograms contain the master acquisition. Since atmospheric phase is spatially correlated and temporally not correlated, a high pass filter in the time domain is applied (since deformation is temporally correlated) followed by a kriging interpolation operation in space domain (since noise does not have spatial correlation) to remove the atmospheric phase. This operation relies on the number of scenes available and the density of the PSC for its accuracy [27], [33]. At this stage, a suitable reference point is chosen such that it has high temporal and spatial coherence to ensure that the reference scatterer is stable. Deformation velocities and residual heights that are estimated in the time series Interferometry are estimated with this scatterer as the reference. This is further explained in the following chapter.

4.2.4. ESTIMATION OF PARAMETERS

The estimation of parameters such as height and deformation velocity is done after the atmospheric phase is removed from the wrapped phase of the PSCs. At this stage, a more relaxed condition can be imposed on the amplitude stability threshold to select more persistent scatterers.

If the total number of persistent scatterer pixels are P and number of interferograms from the master stack are N_I, then the estimation of parameters is a problem of N_P equations with N_I samples. The parameters to be estimated for every persistent scatterer p are the height $\Delta h(p)$ and velocity $\Delta v(p)$, which is solved by the maximization of the periodogram[1] in which the frequencies to be scanned are given by these parameters [31], [40].

The periodogram $\xi[\Delta v(p), \Delta h(p)]$ is expressed as:

$$\xi[\Delta v(p), \Delta h(p)] = \frac{1}{N_I} \sum_{i=1}^{N_I} e^{[j\Delta\phi_{i,k}(p) - \kappa_v \Delta v(p) B_{t,i} - \kappa_h \Delta h(p) B_{n,i}]}, \tag{4.2}$$

where, $\kappa_v = \frac{4\pi}{\lambda}$ and $\kappa_h = \frac{4\pi}{\lambda R sin\theta}$ are factors which link velocity to time and height to normal baseline.

$\Delta\phi_{i,k}(p)$ is the interferometric phase of the interferometric pair (i,k) after the atmospheric phase and flat earth phase are removed. Since it is a single master stack, k is the

[1] A periodogram calculates the significance of different frequencies in a time series to identify any intrinsic periodic signals

fixed master and i is a generic image of the stack.
$B_{t,i}$ and $B_{n,i}$ are the temporal and normal baseline for the interferometric pair.

The solution for the parameters is given by the value that maximises the absolute value of the periodogram and can be expressed as:

$$\Delta\tilde{h}(p), \Delta\tilde{v}(p) = \text{argmax}|\xi[\Delta h(p), \Delta v(p)]|. \tag{4.3}$$

When the argument of the periodogram is close to zero, the observed phase is matched by the model and conversely, when the argument of the periodogram is affected by noise and the temporal coherence is low, the model does not match the observed phase. It is noteworthy to highlight the importance of the number of images (therefore the number of interferograms), (N_I) used since temporal coherence is biased to higher values.

The wrapped phase is unwrapped using the pre-defined temporal deformation model (like the constant velocity model or the periodic model) which are then spatially integrated in order to obtain the time series of deformation with respect to the reference point. The persistent scatterers to be finally used for analysis can be further filtered by a threshold on the temporal coherence. An overview of the various algorithms used for temporal unwrapping can be found in [37], [31].
In case of modelling seasonal signals like thermal expansion, a possible model can be expressed as [40]:

$$\Delta\phi_{i,k}^{therm} = \frac{4\pi}{\lambda}\Delta\alpha(p)\,T_i, \tag{4.4}$$

where, $\Delta\alpha(p)$ is the thermal expansion coefficient of point p in mm/C° with respect to the reference point and T_i is the temperature of the scene at the time of acquisition. When this model is added to the linear deformation model, the periodogram is solved for height, deformation and thermal expansion co-efficient. For buildings with metallic components, the thermal expansion search range values can be between $-0.2 mm/C^\circ$ to $0.6 mm/C^\circ$ [40].

Another category of the PSI technique uses phase stability (instead of amplitude stability) in the space domain in addition to time domain using spatial coherence as a metric [42]. These methodologies are useful in analysing non-urban areas since a less stringent threshold is imposed on the amplitude dispersion [33].

In case of the second category of the PSI technique where phase values are directly analysed, spatially correlated signals are removed by band-pass filtering and the spatially uncorrelated parts of the signals are estimated based on the perpendicular baseline correlation [42].

4.3. DISTRIBUTED SCATTER INTERFEROMETRY

Unlike PS pixels, the resolution cells of the image which contain no prominent strong scatterer, are affected by decorrelation. However, it is still possible for these resolution cells to contain some coherent information in interferograms with small temporal and perpendicular baselines. To reduce the DS pixel noise, filtering techniques such as complex multilooking and spectral filtering are employed. In order to extract this information, it is essential to use interferograms from multi-baseline configurations since the

single master stack will not contain interferograms that are optimal for DS [6]. Another key adaptation of the multi-temporal analysis of distributed scatterers is that the strict requirement of the scatterers having to be coherent in all interferograms is removed using a multi-master approach. Extracting information from distributed scatterers was first done by Berardino et al. [43] with the use of small baseline subsets of interferograms. This methodology was based on the idea that interferograms formed from images acquired within small baselines would suffer less baseline decorrelation. The premise can also be extended to incorporate interferograms that have small temporal or Doppler baselines as well.

4.3.1. ADAPTIVE FILTERING - MULTILOOKING

In order to reduce decorrelation noise, the interferograms can be be filtered by adaptive multilooking. Adaptive multilooking is the process by which spatial averaging (complex) of adjacent pixels in the interferograms is done in order to reduce noise [6]. The operation of multilooking is based on the assumption that the signal of interest is constant over the area around the pixels in which the multilooking process is done and the pixels are statistically homogeneous as shown in figure 4.4. The multilooked interferogram from an image pair (i,k) of a pixel p is computed as:

$$< I_p >= \frac{1}{N}\sum_{i=1}^{N} \mathrm{Img}_{i\,n}\mathrm{Img}_{k\,n}^{*}, \tag{4.5}$$

where <.> denotes the operation of spatial averaging, N is the number of looks and n is the index of all the adjacent pixels used in the multilooking process.

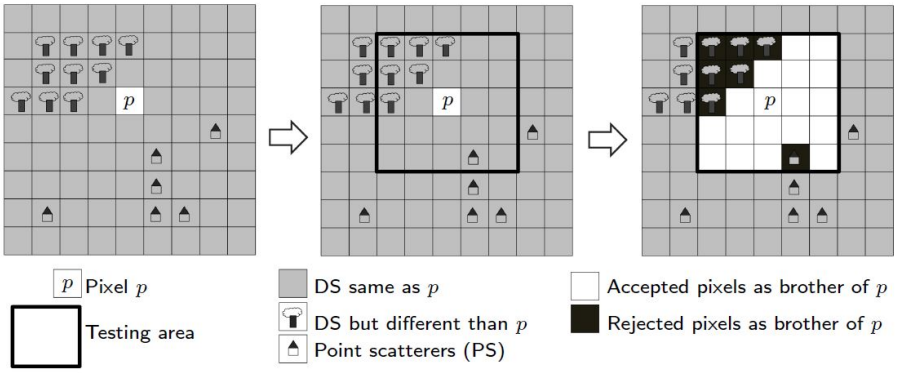

Figure 4.4: Schematic representation of SHP's. A window is chosen around the testing pixel p. All the pixels within this window are tested to check if their statistics are the same as p. The pixels which meet the condition are then used for multilooking. Image source [6].

In order to ensure that the multilooking operation is performed only on the pixels that are statistically homogeneous, spatially adaptive windows are used. There are many techniques to group statistically homogeneous pixels (SHP). It is noteworthy to highlight

that adaptive multilooking for a stack of images for time series interferometry is different from adaptive multilooking for single interferograms. This is because it is to be ensured that the estimation window for averaging is the same for all interferograms in a stack of images to avoid inconsistent multilooking.

The Anderson-Darling (AD) test is one of the non parametric tests used to identify the SHPs around a testing pixel. It was first developed by Anderson and Darling [44] and was modified into a two sample test by Pettitt [45]. It tests the probability distributions of the null hypothesis which is that the pixel under test has the same statistics as the selected pixel, and the alternate hypothesis which is that the statistics do not match. If the selected pixel has amplitude A_p and the test pixel has amplitude A_q, the null hypothesis (H_0) and the alternate (H_α) hypothesis are expressed as:

$$\begin{aligned} H_0 &: F_{\underline{A}_p}(A) = F_{\underline{A}_q}(A), \\ H_\alpha &: F_{\underline{A}_p}(A) \neq F_{\underline{A}_q}(A), \end{aligned} \tag{4.6}$$

where $F_{\cdot}(.)$ is the cumulative distribution function. The empirical cumulative distribution function (ECDF) of the amplitude of a pixel (A_p) in a stack of N images assuming stationarity [2] is computed as:

$$\hat{F}_{\underline{A}_p}(A) = \frac{1}{N}\sum_{i=1}^{N} I_{A_{p,i} \leq A}, \tag{4.7}$$

where $I_{A_{p,i} \leq A}$ is the indicator function which is equal to 1 if $I_{A_{p,i} \leq A}$ and otherwise equal to 0.
The difference between the ECDF of two data samples is used in the Anderson-Darling test for testing homogeneity. The Anderson-Darling test statistic T_{AD} is defined as:

$$T_{AD} = \frac{N}{2}\sum_{A} \frac{(\hat{F}_{\underline{A}_p}(A) - \hat{F}_{\underline{A}_q}(A))^2}{\hat{F}_{\underline{A}_{p,q}}(A)(1 - \hat{F}_{\underline{A}_{p,q}}(A))}, \tag{4.8}$$

where, $\hat{F}_{\underline{A}_{p,q}}$ is the empirical cumulative distributive function computed from the dataset of pixels p and q together.

Another popular non parametric test for the selection of homogeneous pixels is the Kolmogorov-Smirnov(KS) test. There are also parametric tests for grouping pixels which rely on assumptions of probability distribution functions (like Gaussian or Rayleigh) of the data samples. Due to this, computation time is reduced compared to non-parametric tests. For an overview of the different testing strategies the reader is requested to refer to [6].

4.3.2. SELECTION OF DISTRIBUTED SCATTER CANDIDATES

For the selection of distributed scatterers, the metric of spatial coherence is often used [6]. The spatial coherence of a pixel p in the neighbourhood of pixels n within the test

[2] the joint probability distribution (also mean and variance) of a stationary process does not change when shifted in time.

window W of an interferogram generated between two images i and k is estimated as:

$$\hat{\gamma_p} = \frac{\sum_{n \in W} i_n k_n^*}{\sqrt{\left(\sum_{n \in W} |i_n|^2\right)\left(\sum_{n \in W} |k_n|^2\right)}}, \tag{4.9}$$

where W can be a square or a rectangular window. Since the interferograms have been generated using adaptive masks, the noise in pixels which have coherent information is greatly reduced and thus making some of these pixels suitable candidates for distributed scatterers.
From the candidates of distributed scatterers the final set of distributed scatterers can be further filtered using their temporal coherence.

4

4.3.3. ESTIMATION OF PARAMETERS - WEIGHTED APPROACH

The DS pixels in the thesis have been extracted from multi-master interferogram stacks. Multi-master interferogram stacks unlike the single master stack (as seen in figure 4.2) have each image forming an interferometric pair with every other image. The parameters to be estimated using the multi-master stack can be done using the periodogram (modified from equation 4.2) expressed as [40]:

$$\xi[\Delta v(p), \Delta h(p)] = \frac{1}{N_{int}} \sum_{i=1}^{N_{int}} e^{[j\Delta\phi_{i,k}(p) - \kappa_v \Delta v(p) B_{t,i,k} - \kappa_h \Delta h(p) B_{n,i,k}]}, \tag{4.10}$$

where, p denotes the distributed scatter pixel and N_{int} denotes interferogram pair between i, k images. In this case both i and k are generic images from the stack. In order to estimate the height and deformation from DS pixels, the phase differences in the multi-master stack need to be resolved into the phase time series for every scatterer. Since DSs may be coherent only in short normal or temporal baselines, identification of interferograms in which they are coherent needs to be done. Weighted approaches make use of weights to identify the coherent interferogram combinations in order to estimate the deformation and height of a target. Of all the interferometric pairs for a given target, those with the highest weightage of coherence (of the DS pixel between the interferometric pairs' images) is considered.

4.4. SUMMARY

In addition to time series interferometry that makes use of persistent scatterers and distributed scatterers individually, several hybrid methods exist that exploit PSs and DSs together. For an overview of these methodologies the reader is requested to refer to [6]. From the broad methodologies discussed in the chapter it can be inferred that PSI works well in urban areas. For areas with vegetation and low coherence in interferograms of long baselines, the applicability of monitoring deformation using stable scatterers is difficult. It has been shown that distributed scatterers have been used to study deformation in areas with low coherence [46]. The problem statement in this thesis is to estimate relative settlements in agricultural glasshouses. Moreover, the interferometric phase which

is dependent on topography, is used in this study, to analyse the positions of the targets. Greenhouse structures have frames that may stay coherent over time but roof panels which are subject to random movement (owing to the opening and closing of roof panels). Moreover, depending on their location, these structures may be surrounded by pasture fields or by urban infrastructure and this makes development of standardised methodologies, which are uniformly applicable to all structures, difficult. The scope of the thesis includes addressing the problem by analysing both PSs and DSs since the type of processing algorithm employed has a direct impact on studying both the relative settlements as well as identifying the positions of the targets.

5

SAR Data Processing and Areas Analysed

The InSAR processing of greenhouses is done in parallel with understanding the geotechnical influences that affect the estimations of subsidence. The geotechnical data was obtained from Dinoloket [47] and bore holes and CPT data around the region of every greenhouse as beeh analysed. The locations and inferences from the data are presented in chapter 6. This chapter presents the methodologies and approaches adopted to analyse the areas of greenhouses for subsidence using multi temporal InSAR methodologies.

Firstly the entire province of Westland was analysed and later, individual greenhouses were analysed by incorporating time series InSAR methodologies on a smaller scale. The individual greenhouses are located in the regions of Schiphol, Nieuwerkerk aan den Ijssel and Westland. These three regions were chosen since contact with greenhouse owners could be established in these cases. These regions are highlighted in the subsidence map as shown in Figure 5.1.

Incidentally, the three regions have differences in the type of soil strata among them and therefore the analysis of these three regions provides scope for analysing the effect of the role of the soil composition in the detection of subsidence.

Primary analysis was done using RADARSAT-2 data with VV polarization in the ascending track. In order to ascertain the influence on the number of scatterers due to the orientation of the radar beam with respect to the structure of the greenhouses, the SLC images from the descending track with HH polarization was also used for the region of Westland. Lastly, in order to analyse the effect of spatial resolution of the data on the number of scatterers, Sentinel-1 SLC images of VV polarisation in the ascending track was also used.

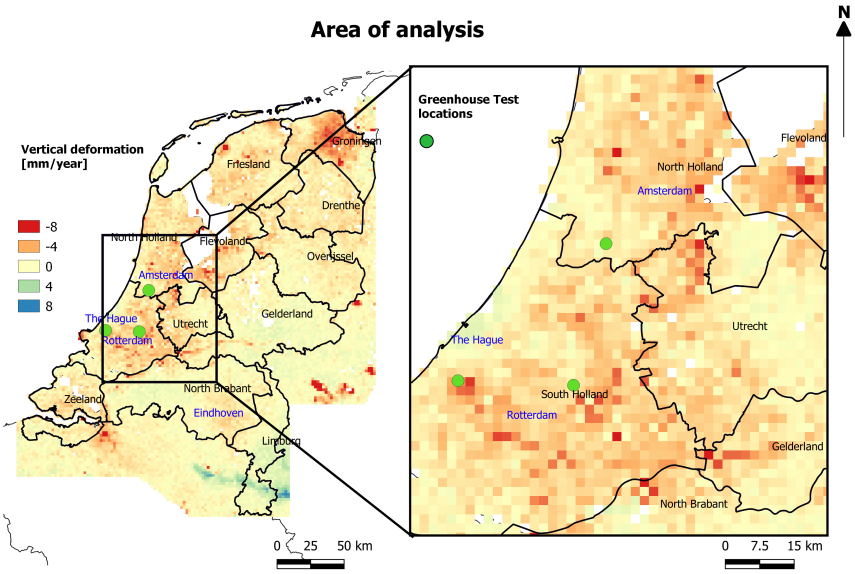

Figure 5.1: Three regions of the Netherlands analysed for subsidence in greenhouses. Data source [7]

5.1. PS INSAR WORKFLOW

The explanation of the theory behind the methodologies of PS InSAR and DS InSAR has been outlined in chapter 4. The current and the next sections outline the workflows of the time series methodologies for estimating deformation and heights from PSs and DSs in the software Sarproz that is used. For the PS methodology, after the creation of an initial mask of points (local maxima of amplitude points), a strict threshold on the amplitude stability index ($\tau_{strict\ amplitude\ stability} > 0.8$) as indicated in Figure 5.2 is imposed to generate a primary network of stable scatterers (PS candidates or PSCs). The interferometric residual phase of these scatterers are used to estimate the APS. The estimation of APS, is done only for large areas (in this thesis, it was done when the whole province of Westland and the town of Nieuwerkerk aan den IJssel were analysed) and not for the analysis of individual greenhouses. This is because, atmospheric phase is spatially correlated over small distances (upto a few kilometers < 5km) and the double differences of the phase (spatial and temporal) with respect to the reference point cancels the effect of the atmospheric phase.

For the PSI methodology in the software Sarproz, interferograms are not explicitly saved, instead, the interferometric phases at the pixel locations of the PSCs are calculated on the fly using a coherence window of 15x15 pixels. The topographic phase is estimated from the elevation model of SRTM. A network of the PSCs is made using Delauney triangulation and an initial estimation of deformation and heights is made from

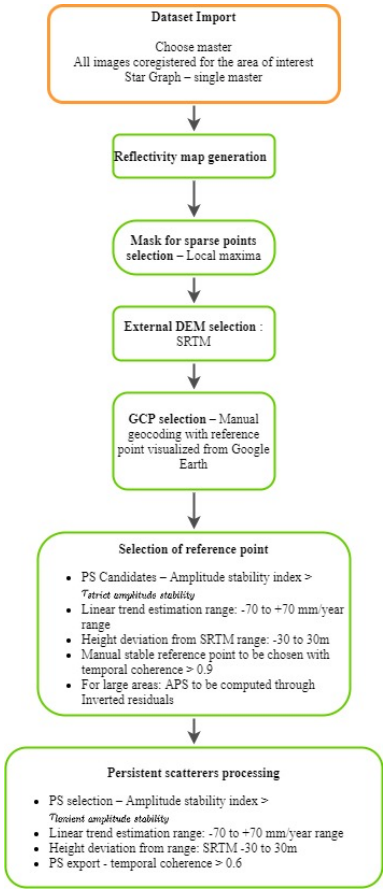

Figure 5.2: PS workflow

the PSCs. After the estimations, the quality of the connections between the PSCs of the network is visualised. The quality of a PSC is high if the phase residuals are zero. The visualisation of this network with the quality of the points plays an important role in selecting a reference point. It is ensured that the reference point has a temporal coherence greater than 0.9. In addition, the point is visualised on the reflectivity map as well as Google Earth to verify that it is a point on a stable structure close to the site of the greenhouse as shown in Figure 5.3. For all the individual greenhouses analysed in Westland, the rate of subsidence of scatterers obtained from the previously performed Westland province analysis, is used as an additional parameter to select a reference point that is stable.

After the selection of the reference point, depending on the density of the scatterers, a lenient threshold is imposed ($\tau_{lenient\ amplitude\ stability} < \tau_{strict\ amplitude\ stability}$) to include more scatterers in the network. Estimations of height and deformation are now performed with respect to the reference point. The final PSs that have temporal coher-

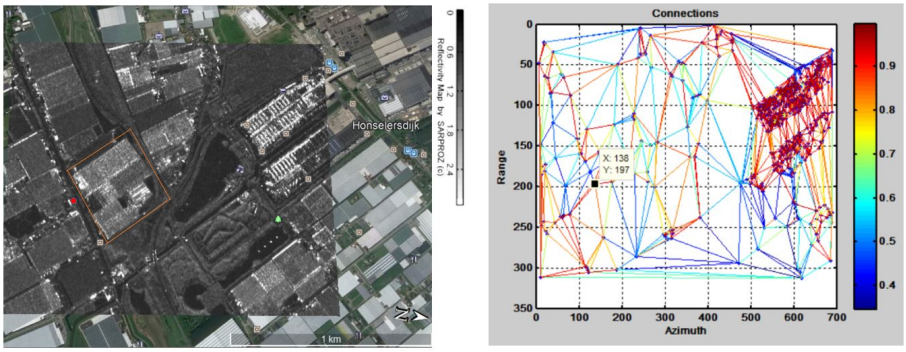

Figure 5.3: Reference point chosen from the network of PSC is highlighted in red in the reflectivity map. Greenhouse 'Westland A' is highlighted with an orange boundary.

ence greater than 0.6 are exported. The top row of figure 5.5 shows the plot of amplitude stability and temporal coherence for Greenhouse 'Westland A'.

5.2. DS INSAR WORKFLOW

The workflow for the DSs InSAR analysis as performed in the software is presented in Figure 5.4.

For the DS methodology,after the reference point is chosen in a manner similar to that of the PS methodology, the image configuration for the generation of interferograms is changed from that of the single master to a full graph where all combinations between the images are taken into account (multi master approach). In case of a large processing area, APS is still estimated using a single master configuration.

An adaptive mask is generated using the Anderson Darling test (explained in section 4.3.1) to evaluate the likeness between adjacent pixels in a window size of 5x5 pixels. This mask is then used to filter the interferograms. The coherence between the interferometric pairs is saved. The selection of DSs is made on the basis of the spatial coherence of the candidate pixels. It is noteworthy to mention that the solution to the estimations of heights and deformation is obtained by the maximization of the periodogram as expressed in equation 4.10 with coherence used as weights. The weighted approach is therefore used to select the combinations of interferograms with maximum coherence. The various thresholds used for the projects analysed in the thesis are tabulated in 5.1. After the processing of these selected pixels for heights and deformation is carried out, the final DSs are exported by imposing a condition on their temporal coherence as was done in the case of PSs. The bottom row of the figure 5.5 shows the spatial coherence and the size of the adaptive mask clusters for Greenhouse 'Westland A'.

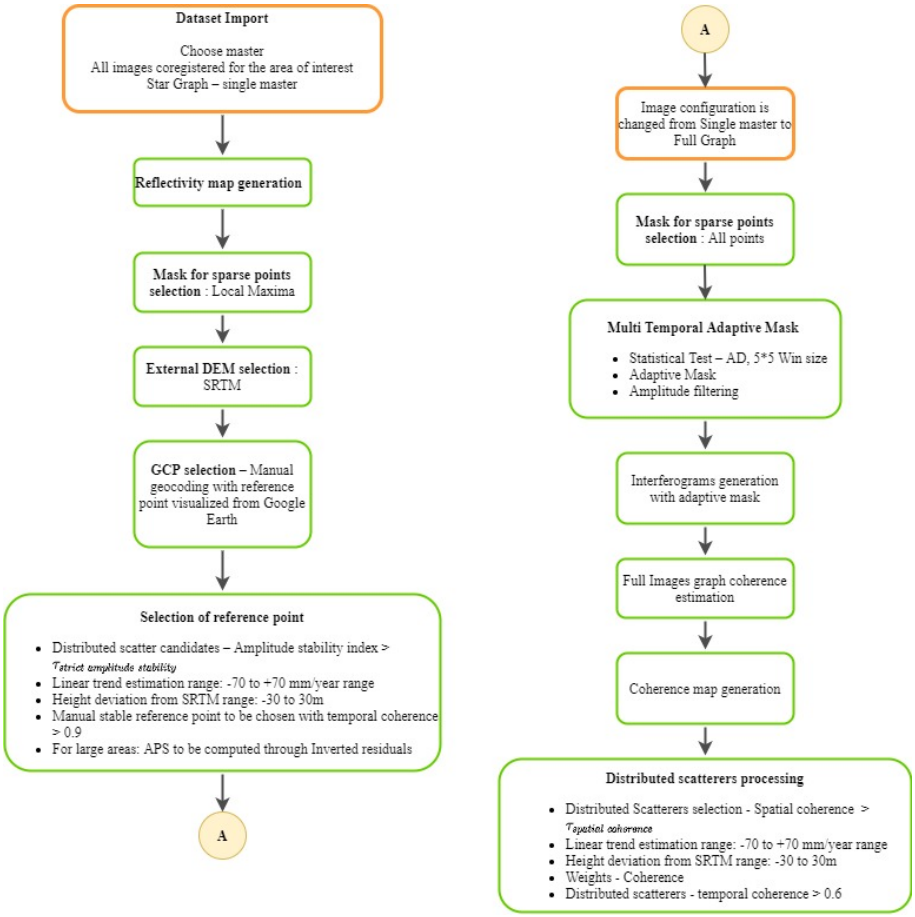

Figure 5.4: DS workflow

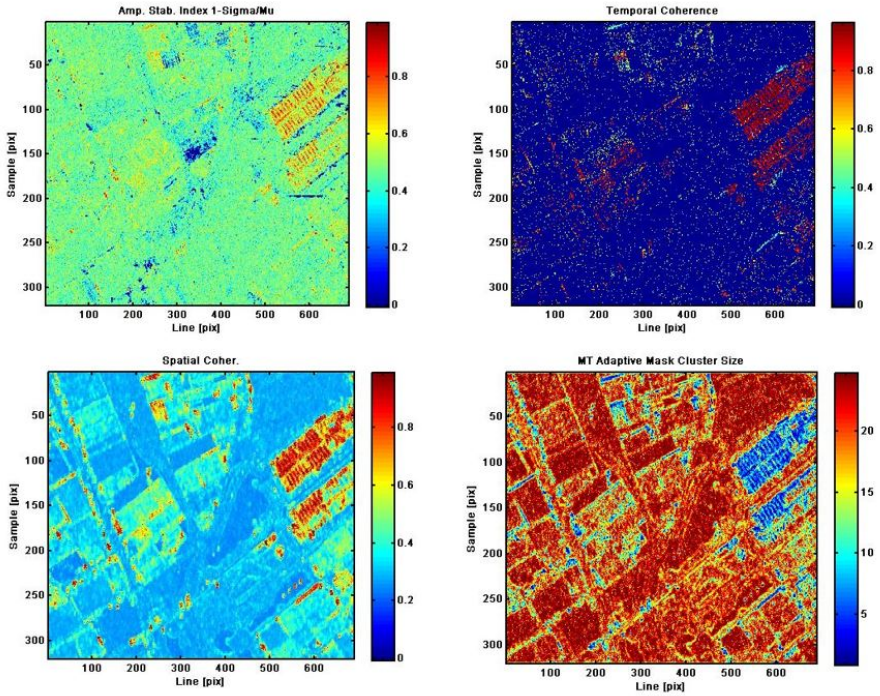

Figure 5.5: Spatial plots of amplitude, temporal coherence, spatial coherence and the adaptive mask for Greenhouse 'Westland A'

5.3. EXPORTING AND VISUALISATION OF DATA

The PSs and DSs can be exported as kml's from the software. The time series deformation curves of every scatterer is then visualised. Additionally for data analysis, the residual heights, temporal coherences, geo-locations and deformation velocities have also been exported as comma separated values (csv's) files.

They were then imported into a GIS software (QGIS) to perform spatial operations. Greenhouses and buildings around the regions of analysis have been digitised. In case of large area analysis (Nieuwerkerk aan den IJssel and Westland) where multiple greenhouses, ground points and buildings are analysed, the sequence of operations to extract the scatterers within the digitised boundaries of interest is as follows: Intersection (of scatterer points with the polygon shapefile of a single class - either greenhouse or buildings), split vector tool (to export the scatterers of individual greenhouses or buildings as a separate geopackage file) and then the geopackage files were converted to csv data in Python.
Outlier removal, generation of histograms and computation of statistics of scatterers were performed in Python. The outlier removal was done by imposing thresholds on the range of residual heights and a minimum temporal coherence.

Table 5.1: Projects processed. The strict amplitude stability threshold for PS and DS is applied only for the selection of reference point or for APS alone and not for the selection of scatterers themselves. For all projects, this threshold is 0.8. It is therefore not mentioned in the table.

Analysis project	Satellite, Track direction, No. of images	Scatterers Observed	Initial mask on SLC images	Duration	Master dd-mm-yyyy	PS thresholds	DS thresholds
Nieuwerkerk aan den IJssel - multiple greenhouses and buildings Area > 6 sq km	RS-2, Ascending, 28	PS	Local maxima	Jan 2017 to Dec 2018	19-01-2018	$\tau_{lenient\ amp\ stab} > 0.7$ TC >0.6	
		Temporal coherence filtered scatterers	Local maxima	Jan 2017 to Dec 2018	19-01-2018	TC >0.6	
Schiphol - single greenhouse	RS-2, Ascending, 28	PS	Local maxima	Jan 2018 to Jan 2020	07-02-2020	$\tau_{lenient\ amp\ stab} > 0.65$ TC >0.6	
Westland Municipality Area > 100 sq km	RS-2, Ascending, 28	PS and DS	Local maxima (PS and DS)	Jan 2017 to Dec 2018	19-01-2018	$\tau_{lenient\ amp\ stab} > 0.75$ TC >0.6	$\tau_{spatial\ coherence} > 0.85$ TC >0.6
	Sentinel1, Ascending, 59	PS	Local maxima	Jan 2017 to Dec 2018	11-01-2018	$\tau_{lenient\ amp\ stab} > 0.75$ TC >0.6	
	RS-2, Descending, 26	PS and DS	Local maxima (PS and DS)	Jan 2017 to Dec 2018	09-01-2018	$\tau_{lenient\ amp\ stab} > 0.75$ TC >0.6	$\tau_{spatial\ coherence} > 0.85$ TC >0.6
Westland 'Greenhouse A'	RS-2, Ascending, 28	PS and DS	Local maxima (PS) All points(DS)	Jan 2017 to Dec 2018	19-01-2018	$\tau_{lenient\ amp\ stab} > 0.6$ TC >0.6	- $\tau_{spatial\ coherence} > 0.75$ - $\tau_{spatial\ coherence} > 0.65$ - $\tau_{spatial\ coherence} > 0.45$ TC >0.6
	RS-2, Descending, 28	PS	Local maxima	Jan 2017 to Dec 2018	09-01-2018	$\tau_{lenient\ amp\ stab} > 0.6$ TC >0.6	
Greenhouse Westland 4 and 9	RS-2, Ascending, 28	PS and DS	Local maxima (PS) All points(DS)	Jan 2017 to Dec 2018	19-01-2018	$\tau_{lenient\ amp\ stab} > 0.75$ TC >0.6	$\tau_{spatial\ coherence} > 0.75$ TC >0.6
Greenhouse Westland B	RS-2, Ascending, 28						

6

Results and Discussion

This chapter presents the results and the inferences drawn from them. It is subdivided into sections. In sections 6.1 and 6.2, the results of the large area wise analysis and individual scale analysis of PSs are presented respectively. The analysis is made by providing context of geotechnical data. Sections 6.3 and 6.4 present the results for the analysis of the positions of the targets from the residual height estimations of PSs and DSs. Section 6.5 presents the results for evaluating the effect of thermal contributions in the estimations of deformation in a greenhouse. The last section 6.6 presents the results for the comparison between PSs and DSs in their ability to represent areas of subsidence in a greenhouse.

6.1. Combined InSAR and Geotechnical analysis - Westland Municipality

This section is divided into two parts. Section 6.1.1 contains the results of the PSs (threshold of 0.75 used on their amplitude stability index) detected for the big area analysis of Westland. Section 6.1.3 presents the results for the comparison between the magnitude of deformation estimated and the type of soil present in the regions analysed.

6.1.1. Number of Persistent scatterers

Figure 6.1 shows the number of PSs on greenhouses from the ascending track of Radarsat-2 data. From this, it was seen that only 89 of 1388 greenhouses had more than 10 PSs.

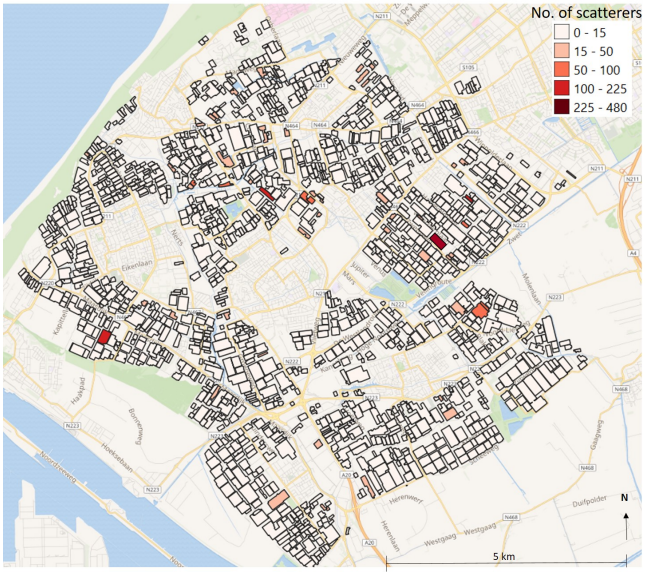

Figure 6.1: Number of PSs on greenhouses with Radarsat-2 Ascending track direction - Westland municipality

Figure 6.2 shows the number of PSs on greenhouses from the descending track of Radarsat-2 data. From this analysis, it was seen that only 101 of 1388 greenhouses contained more than 10 PSs. The shapefile polygons for the greenhouses in Westland were obtained from PDOK open source data [48]. The number of greenhouses in this case is only slightly higher than that for the ascending track direction.

Figure 6.3 shows the number of PSs on greenhouses from both the ascending and descending tracks of Radarsat-2 data. Together, when both track directions are considered, the number of greenhouses that contain more than 10 PSs is 196 out of 1388 greenhouses. The analysis therefore indicates that most greenhouses have PSs that get detected for a specific track direction (when the amplitude stability index chosen is 0.75). This indicates that the orientation of the beam with respect to the orientation of the greenhouse plays a significant role for the detection of PSs.

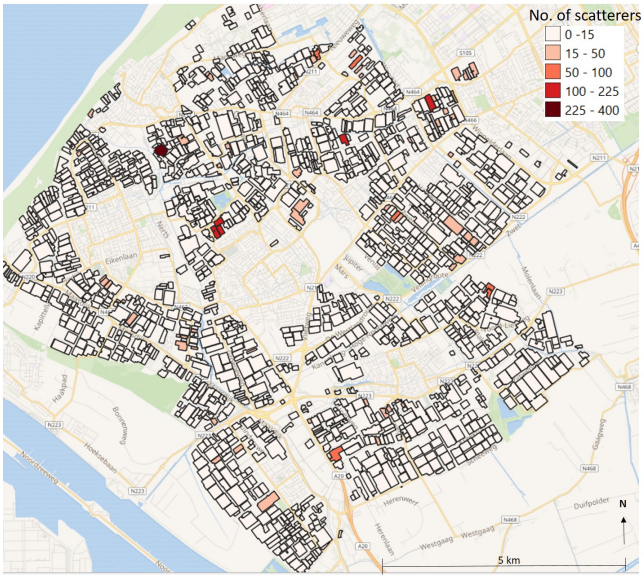

Figure 6.2: Number of PSs on greenhouses with Radarsat-2 Descending track direction - Westland municipality

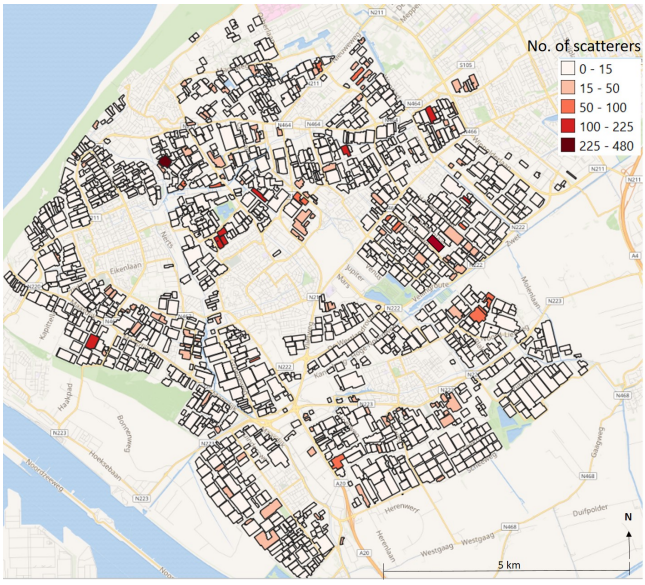

Figure 6.3: Number of PSs on greenhouses with Radarsat-2 - both track directions - Westland municipality

6.1.2. NUMBER OF PSS - SENTINEL-1 AND RADARSAT-2

To compare the number of scatterers obtained from Sentinel-1 and Radarsat-2, the ascending track direction of both datasets are considered. Recall that the spatial resolution of Sentinel-1 is lower than that of Radarsat (The specifications can be seen in table 3.1). It was seen that despite the lower resolution of Sentinel-1, PSs were still present on some greenhouses. The number of greenhouses that contained PSs from Sentinel-1 data were lower than the number of greenhouses that contained PSs from Radarsat-2 data. The reduction in the number of PSs from Sentinel-1 data can be attributed to its lower spatial resolution. Since Sentinel-1 data has a higher temporal resolution, the number of images in a given time span is higher than that for Radarsat-2. Note that in the two year time span, only 28 Radarsat-2 images are present whereas 59 Sentinel-1 images are present. This means that the PSs have to stay coherent in more number of images for Sentinel-1 than for Radarsat-2. It was seen that, when the same threshold for amplitude stability index of 0.75 and temporal coherence of 0.6 was used, only 12 out of 1388 greenhouses contained PSs. However, it is interesting to note that only 2 among these 12 greenhouses were common to the greenhouses that contained PSs from Radarsat-2. This indicates that there is potential for the usage of Sentinel-1 data to increase the number of greenhouses that can be monitored. Figure 6.4 shows the presence of PSs in two greenhouses from Sentinel-1 data that are not present when Radarsat-2 data is used. Possible reasons for this could firstly, be due to the incidence angle being different between the two satellite datasets and secondly due to the difference in the viewing geometries between Radarsat-2 and Sentinel-1 as Sentinel-1 has a smaller orbital tube (50m radius for Sentinel-1 and 100m radius for Radarsat-2).

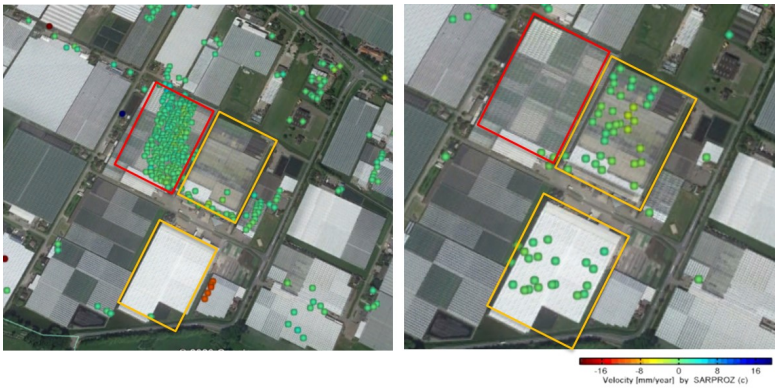

Figure 6.4: PSs using Radarsat-2 (L) and Sentinel-1 (R) - Ascending track. It can be seen that the greenhouses containing PSs are different in each case.

6.1.3. DEFORMATION ESTIMATIONS FROM PERSISTENT SCATTERERS

This section presents the results of the magnitude of deformation as estimated from the PS InSAR analysis. The estimations of deformation are only along the line of sight (LOS) direction and the results have not been converted into absolute vertical direction. Figure 6.5 shows the PSs and the scale of deformation in mm/year.

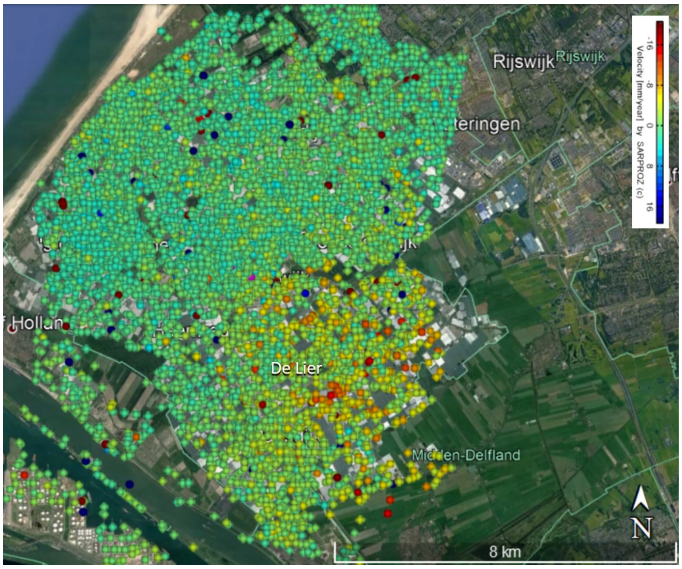

Figure 6.5: Deformation from PSs in Westland - Radarsat-2 Ascending track direction - Note that the region around De Lier in the south east portion shows significant deformation.

From the analysis, specific greenhouses that contained PSs showing deformation rates higher than 5mm/year were selected. The visualisation of these PSs can be seen in the appendix A.2. Two of these greenhouse owners confirmed the presence of subsidence related problems. It was not possible to establish contact with the other greenhouse owners.

From the results of deformation of the big area analysis of Westland, it can be seen that though there are PSs throughout westland that show the presence of deformation, the region around De Lier specifically has pronounced deformation between 3mm/year to 18 mm/year. Figure 6.6 shows one of the PSs having a deformation rate of 17mm/year.

To understand the geotechnical factors at play, soil cross section profiles (from bore hole data) were analysed from Dinoloket [47] for the two regions, De Lier and the western portion in westland respectively. While the former shows maximum deformation for the municipality, the latter shows the least amount of deformation.

On analysing the type of soil strata in the two regions, it was seen that De lier has compressible soil types (both peat and clay) very close to the ground surface whereas the western portions of westland has incompressible soil layers (fine sand) close to the ground surface. The cross sectional profiles are shown in figures 6.7 and 6.8 respectively.

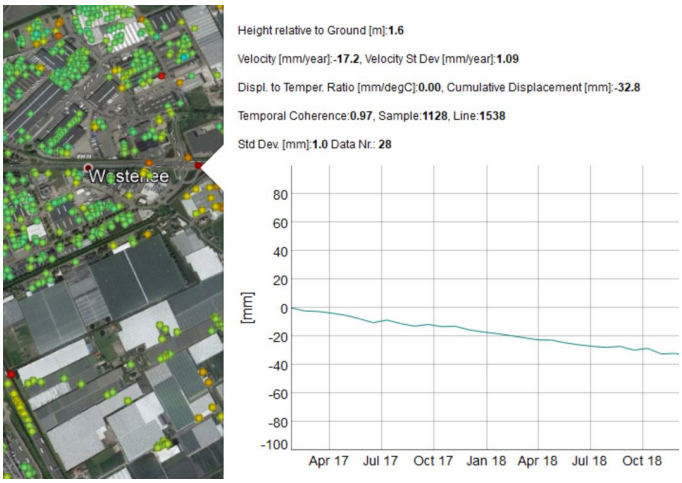

Figure 6.6: One of the PSs showing high deformation rate in the region of De Lier. Note that the scatterer has a temporal coherence of 0.97 and is therefore considered to be very reliable.

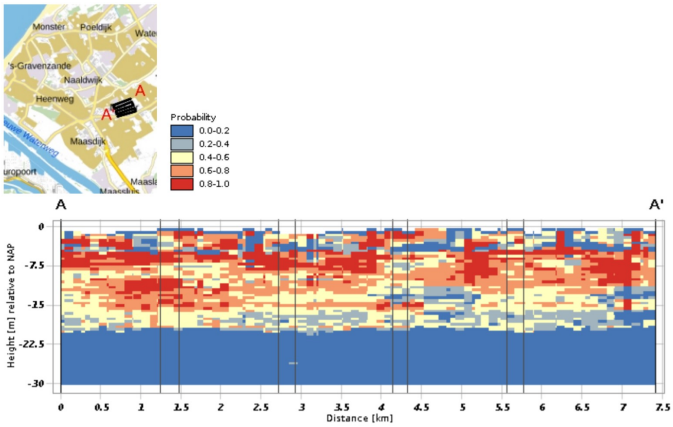

(a) Probability of clay

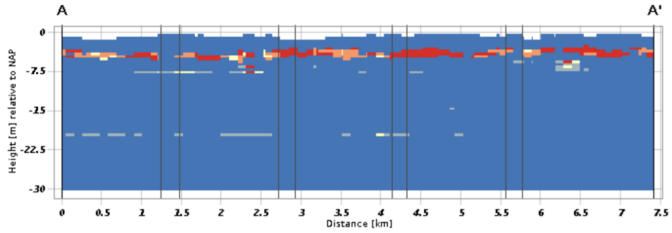

(b) Probability of Peat

Figure 6.7: High probability of compressible soil types (peat and clay) in the top 10m around the region of De Lier.

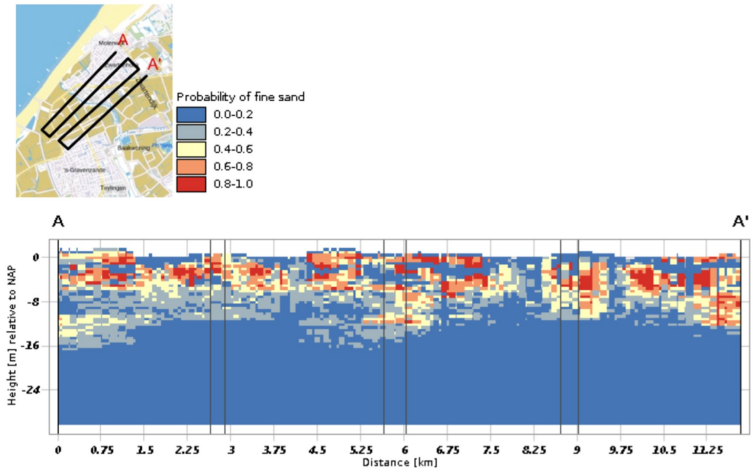

Figure 6.8: High probability of fine sand (incompressible soil layer) in the top 10m around the western portion of the analysis area of Westland.

6.2. COMBINED INSAR AND GEOTECHNICAL ANALYSIS - INDIVIDUAL GREENHOUSES

This section presents the results of the correlation of the estimated deformation from the PS InSAR analysis of individual greenhouses and their surrounding areas with the type of soil strata present at the respective regions.

6.2.1. SCHIPHOL

Figure 6.9: Persistent scatterers - InSAR Analysis in the area of a greenhouse in Schiphol

From the PSs shown in figure 6.9, it can be seen that none of the scatterers on the roads show high deformation values (>4 mm/year).

With this context, the borehole profiles of some points on the roads in these areas are analysed. The soil profile of a point on the road is shown in figure 6.10 where compressible layers are present until 5.5 m below ground level.

Further investigation of other bore hole sites in the area is shown in figure 6.11.

The soil profile indicated at location 1 in figure 6.11 is primarily used for top soil analysis. This data has applications for agriculture. For the purpose of studying aspects like expected settlements, effect of having shallow slab foundations with no piles, this data can be useful. Where information of pile foundations are known, the top 1m soil profile has little relevance.

It can be noticed in figure 6.11, that the bore hole at point number 2 shows sand starting very close to the ground surface. It is possible that the presence of an incompressible soil layer close to the ground surface may be contributing to the low rate of deformation

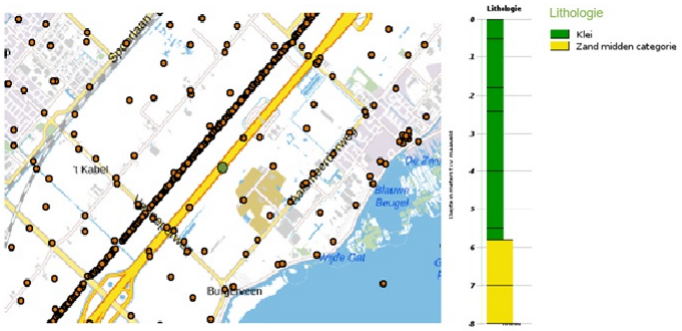

Figure 6.10: Soil profile of a borehole on the road - Schiphol. The location of the borehole is highlighted in green.

Figure 6.11: Borehole 1 shows the shallow profile and borehole 2 shows a deep soil profile

observed in the PSs of the InSAR analysis as shown in figure 6.9. A noteworthy point here is that the soil profile in borehole 2 does not indicate the same vertical soil profile as in the case of borehole 1. This is possibly an indication of the variation in soil profile even in the small distance between the points.

Along the linear set of bore hole points shown in figure 6.12, compressible soil layers are present in the top 1m below which sand is present.

CPT data was analyzed for points in the area as shown in figure 6.13. The cone resistance and friction number for the CPT site are shown in figure 6.14.

From the graphs of cone resistance and friction number in figure 6.14, it is likely that incompressible soil layers are expected to be found in the top 5m of the soil depth. Further, the presence of compressible soil layers in the top 5m of the soil strata can also be verified from the cross sectional profile as shown in figure 6.15.

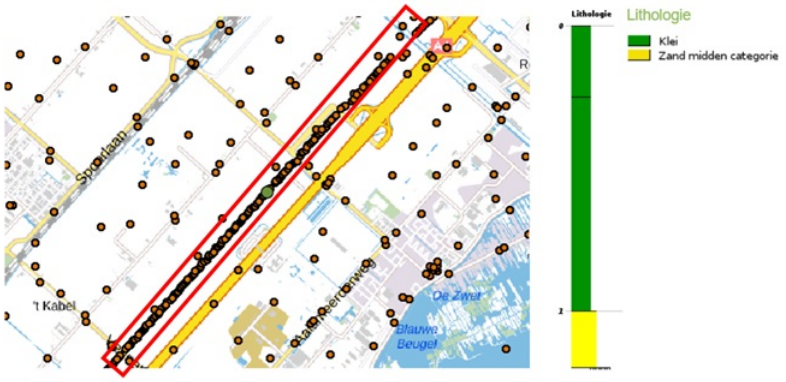

Figure 6.12: The soil profile a borehole from the set of linear bore holes highlighted in red

Figure 6.13: Locations of cone penetration test sites - Schiphol. The site analysed is highlighted in green

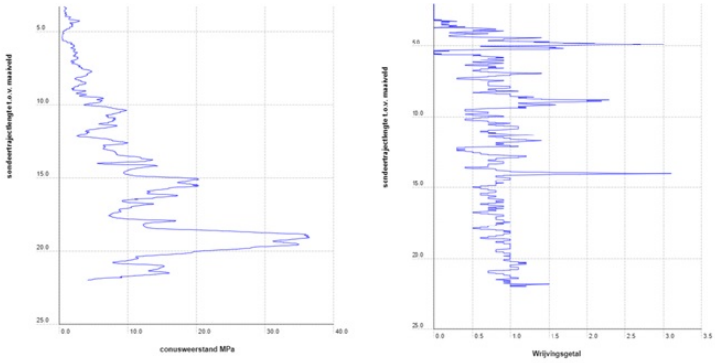

Figure 6.14: Left: Cone Resistance and Right: Friction Number at the site analysed in Schiphol

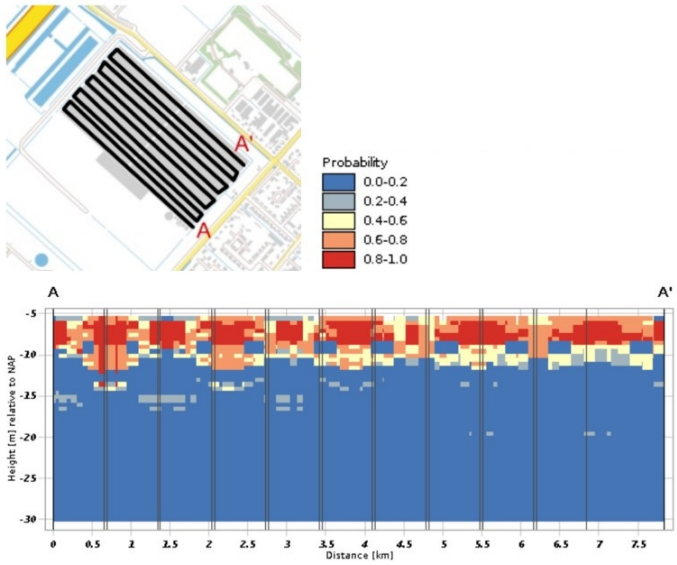

Figure 6.15: Soil Profile for Cross section through the greenhouse at Schiphol

From the comparative studies of the deformation estimated from PSs and the geotechnical data, it can be inferred that the low magnitudes of deformation estimated from the PSs, is corroborated by the presence of incompressible soil layers close to the top soil. The presence of an incompressible soil layer very close to the surface supports the estimation of low deformation rates.

6.2.2. NIEUWERKERK AAN DEN IJSSEL

The PSs in Nieuwerkerk aan den Ijssel region is seen in figure 6.16. Greenhouse A and Greenhouse B are marked in figure 6.16b. The soil bore hole data and CPT data have been obtained for locations shown in figure 6.17.

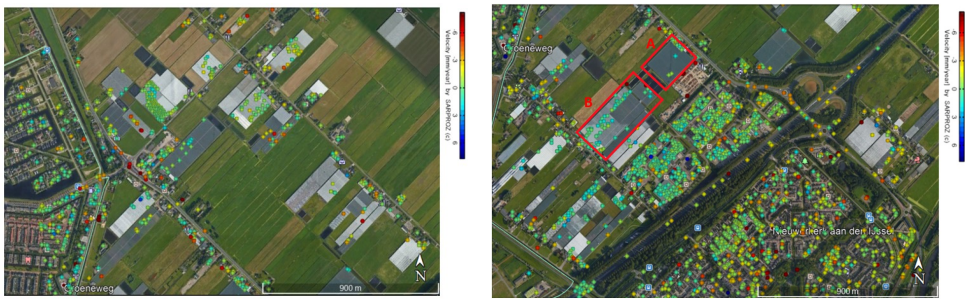

(a) Part 1

(b) Part 2

Figure 6.16: Persistent scatterers in Nieuwerkerk aan den Ijssel. Greenhouses A and B are annotated

Figure 6.17: Boreholes(Red) and Cone Penetration Test Locations(Purple) in Nieuwerkerk aan den Ijssel

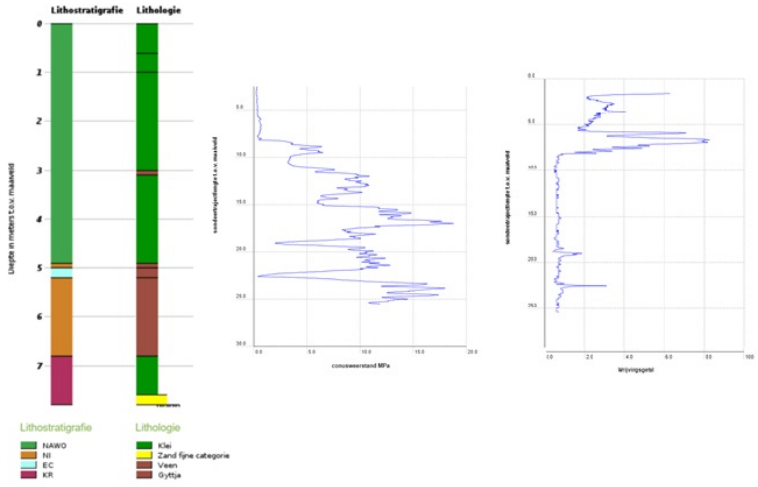

Figure 6.18: Soil Profile(left) and Cone Resistance(center), Friction number(right) graphs for location 1 in Nieuwerkerk aan den Ijssel. The receding (negative) spikes at 20m is possibly indicative of peat or clay soil and it can also be seen in the friction ratio graph below where the same is indicated by a positive spike

From the cone resistance and friction ratio graphs as shown in figures 6.18 to 6.21, it can be inferred that the first 10m of the soil is compressible and the incompressible layers are present only at depths exceeding 10m.
This can also be seen from the cross sectional soil profile through the greenhouse (Greenhouse A) which is known to have suffered subsidence (as reported by the Greenhouse owner). The cross sectional profile for the greenhouse is shown in figure 6.22.

The owner of Greenhouse A has indicated that the piles in the foundation of his

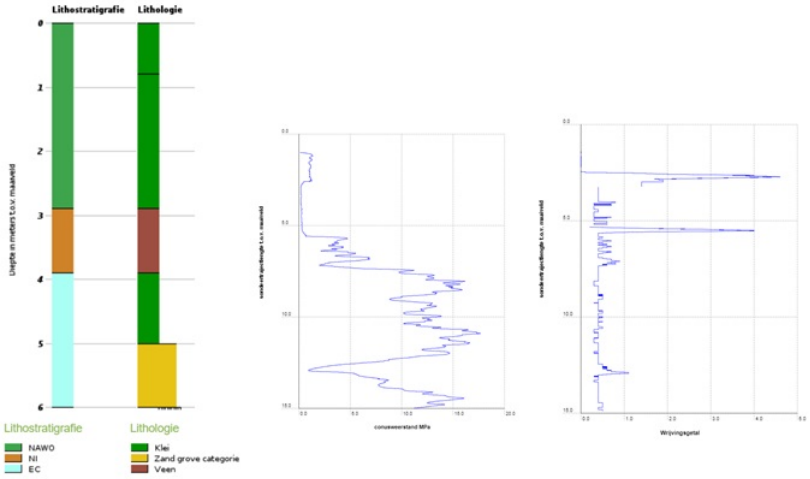

Figure 6.19: Soil Profile(left) and Cone Resistance(center), Friction number(right) graphs for location 3 in Nieuwerkerk aan den Ijssel

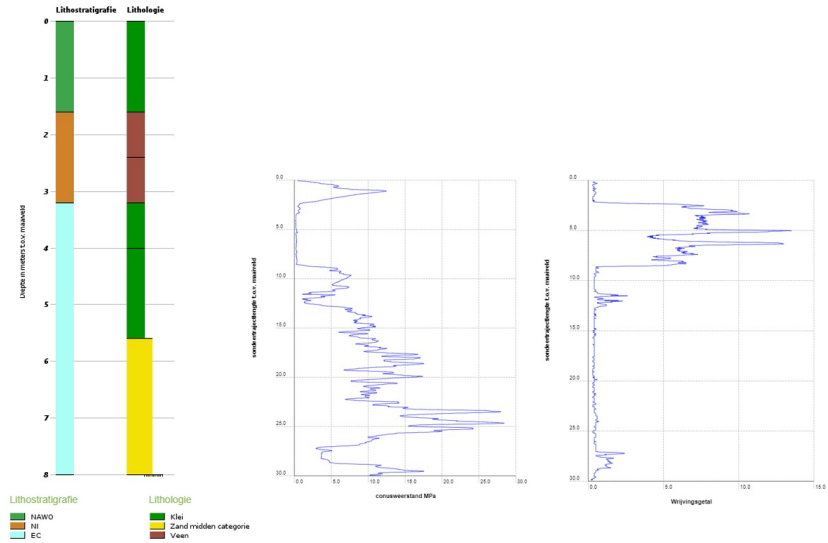

Figure 6.20: Soil Profile(left) and Cone Resistance(center), Friction number(right) graphs for location 4 in Nieuwerkerk aan den Ijssel

greenhouse are 5m deep and that his greenhouse is experiencing problems with settlement. On analyzing the soil characterization graphs, it can be seen that the first incompressible soil layer i.e. sand, is encountered at depths close to 10m. Therefore it is possible that the floating piles do not reach the sand layer and there is consolidation of the slab that draws the piles downward. Differential settlement is also possible due

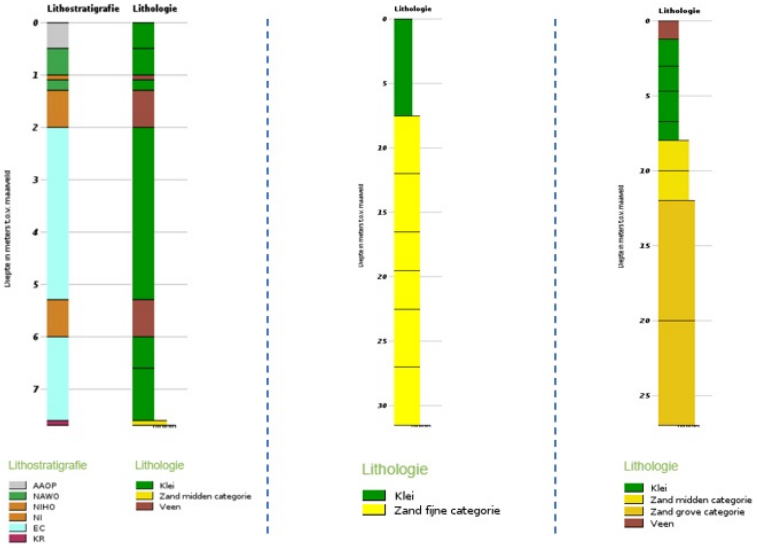

Figure 6.21: Soil Profile for location 2(left), location 5(center), location 6(right) in Nieuwerkerk aan den Ijssel. CPT test data not available in these locations

to the intermediate soil layers of smaller depths present in the different locations of the greenhouse. The spikes of the cone resistance and friction ratio graphs shown in figures 6.18 to 6.21 indicate the presence of intermediate soil layers. The PS InSAR methodology in the case of this greenhouse, does not have sufficient scatterers that can be used to estimate the rate of deformation.

On the other hand, in case of Greenhouse B, the owner has conveyed that his greenhouse is stable and that the pile foundations are at depths ranging between 14m to 17m. This depth safeguards the greenhouse against subsidence of piles since there is a high probability of sand at around 15m as shown in figure 6.22. The PSs from the InSAR analysis also indicates that no significant deformation is estimated as shown in figure 6.16b.

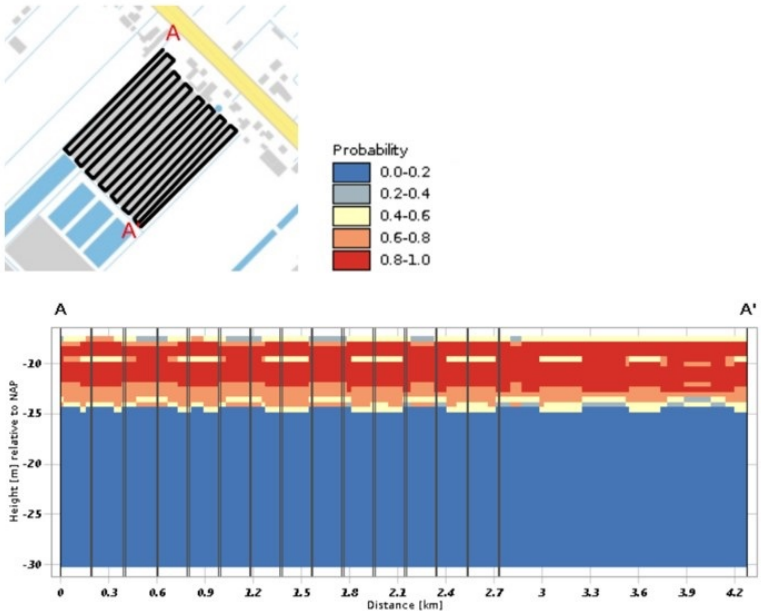

(a) Probability of clay

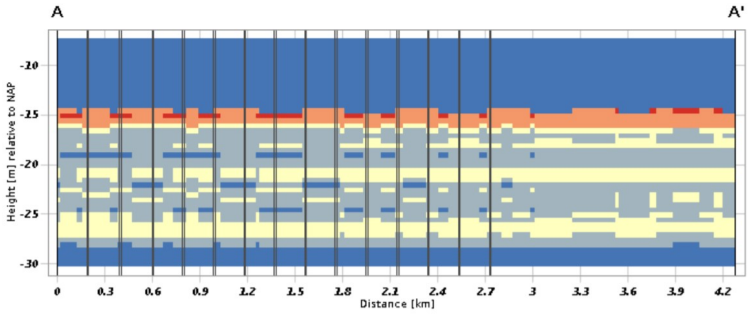

(b) Probability of moderately coarse sand

Figure 6.22: Cross sectional soil profile through greenhouse A at Nieuwerkerk

6.2.3. GREENHOUSE WESTLAND A

The PSs from the InSAR analysis for 'Greenhouse Westland A' is shown in figure 6.23.

Geotechnical data was analysed for the region as shown in 6.24a, which shows the locations of bore hole test sites. Due to the absence of CPT test sites close to most of these bore hole sites, CPT data is analysed in alternate locations close to the greenhouse as shown in figure 6.24b.

From the CPT and bore hole data as shown in figures 6.24 to 6.28, it can be seen that there is a high probability of compressible soil layers until depths of 10m to 20m. This can also be verified from the cross sectional soil profile data for Greenhouse Westland A

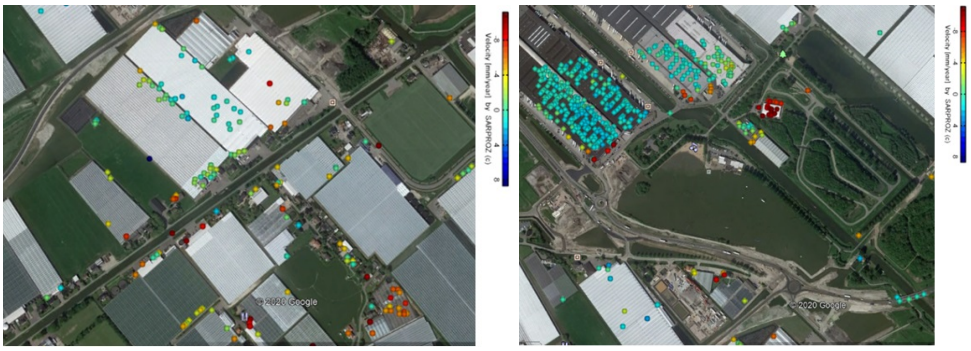

(a) Persistent scatterers of Greenhouse Westland A

(b) Persistent scatterers to the north of Greenhouse Westland A

Figure 6.23: Persistent scatterers in and to the north of Greenhouse Westland "A"

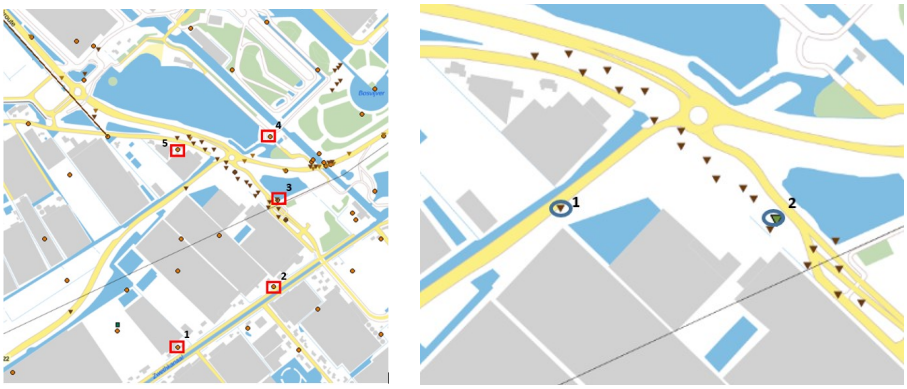

(a) Boreholes

(b) CPT test sites

Figure 6.24: Boreholes and CPT test site locations in Westland

as shown in figure 6.29.

Also, the top soil in this region contains peat as shown in figure 6.29b which is highly susceptible to compression.

The owner of Greenhouse Westland A has indicated that his greenhouse is facing problems of settlement. The greenhouse foundation consists of piles, some of which are 6m deep and some 20m deep. From the geotechnical data, it can be seen that there is a small layer of incompressibility in the soil strata at 8-11m but sand is most likely present only after 20m. Therefore a pile depth of 6m is not enough to safeguard the greenhouse from settlement. Differential settlement is most likely present due to the fact that some piles are only 6m deep whereas some others are 20m deep. The PSs from the InSAR analysis of this greenhouse indicates that the greenhouse is not as stable as commercial buildings. Analysis of the DSs for this greenhouse is presented in section 6.6.

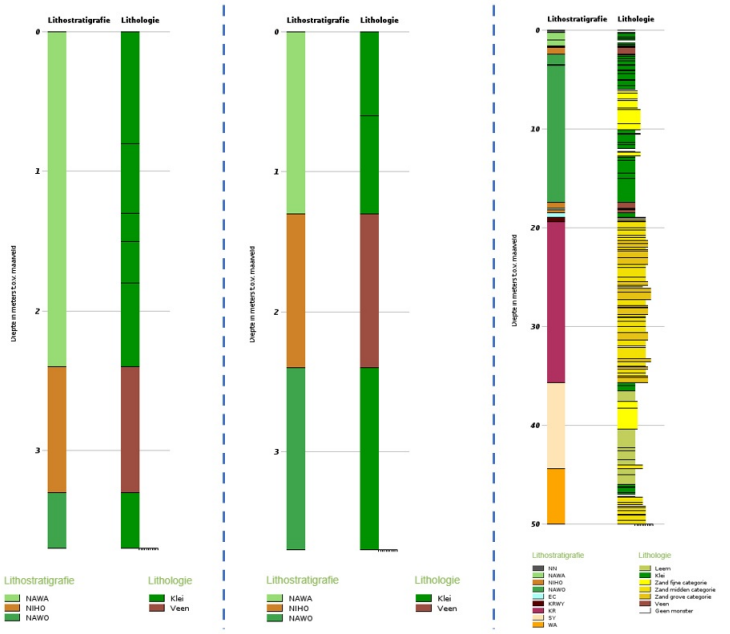

Figure 6.25: Soil Profile for location 1(left), location 2(center), location 3(right) in westland

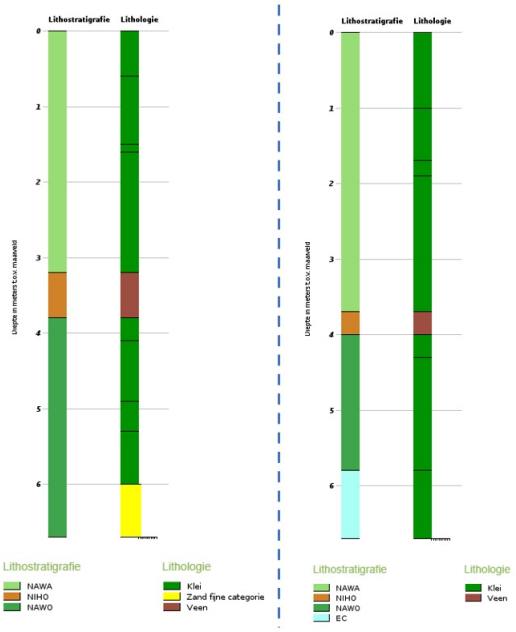

Figure 6.26: Soil Profile for location 4(left), location 5(right) in westland

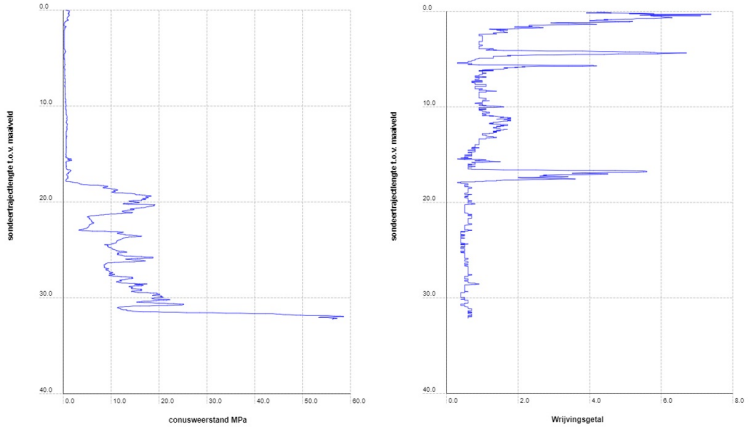

Figure 6.27: CPT graphs for location 1 in Westland.Left: Cone Resistance and Right: Friction Number

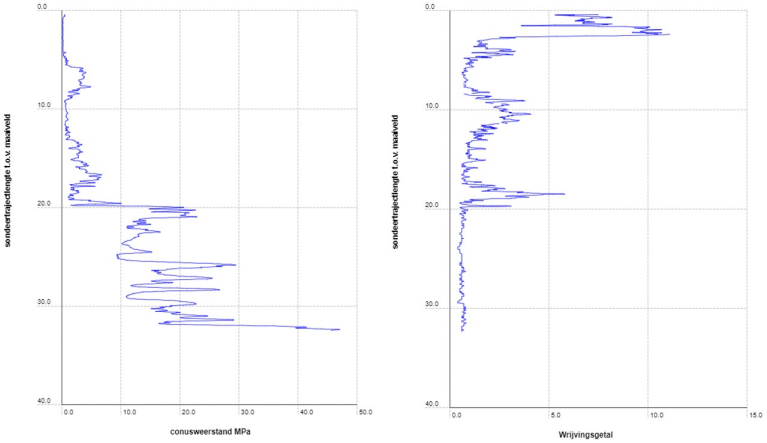

Figure 6.28: CPT graphs for location 2 in Westland.Left: Cone Resistance and Right: Friction Number

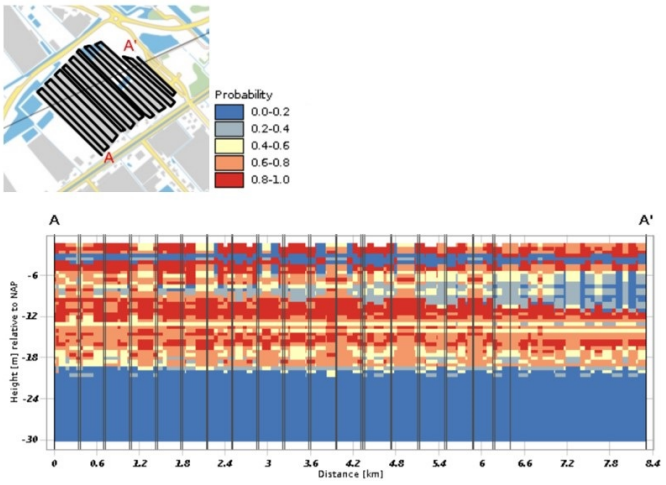

(a) Probability of clay

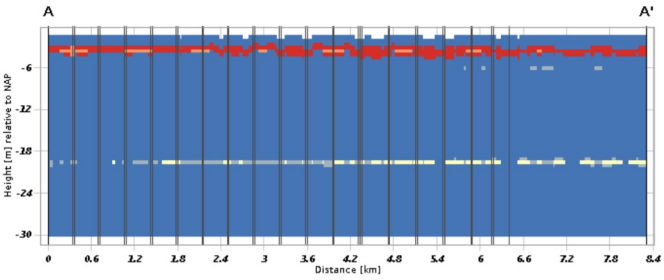

(b) Probability of Peat

Figure 6.29: Soil Profile for Cross section through Westland greenhouse A

6.3. HEIGHTS ANALYSIS - NIEUWERKERK AAN DEN IJSSEL

In order to understand where radar signals are getting back-scattered from, the residual heights of scatterers are analysed. Along with the mean heights, the measures of spread ie., interquartile range (IQR) and standard deviation are also computed. The IQR is used because it is less affected by the data points at the tail ends of the distribution. The analysis is done with two types of scatterers for the area of Nieuwerkerk aan den IJssel. One with all pixel scatterers that have temporal coherence exceeding 0.6 and the second being all PSs with amplitude stability index greater than 0.7 and temporal coherence greater than 0.6.

PIXEL SCATTERERS WITH TEMPORAL COHERENCE GREATER THAN 0.6.

The aim of the analysis is to also compare the statistics of the residual heights of greenhouses to other surfaces such as ground, buildings where it is known that the radar signal cannot penetrate the surface.

Figure 6.30 shows the histograms of the residual heights of pixel scatterers that have a minimum temporal coherence of 0.6 for the region of Nieuwerkerk aan den IJssel. The threshold on the temporal coherence is placed to select the scatterers that fit the model well (linear deformation model with APS only for large areas, and heights and deformation being the parameters to be estimated). All the histograms of the residual heights of the scatterers on the greenhouses show a bell shaped distribution. For the buildings, however, the number of scatterers with a minimum temporal coherence of 0.6, was insufficient to infer results from histograms and are therefore not shown here. Tables 6.1 and 6.2 show greenhouses and buildings which have a minimum of 40 such scatterers. Of the 33 greenhouses analysed, 30 greenhouses have a minimum of 20 scatterers whereas only 7 of the 31 buildings have a minimum of 20 scatterers. Additionally, scatterers from the ground were also used for the comparison. Figure 6.31 shows the histogram of the residual heights for the scatterers on the ground that have a minimum temporal coherence of 0.6. The range and standard deviation of these points do not indicate that the scatterers are from targets which are all present at the ground level. Therefore, this means of comparison does not serve the intended purpose of differentiating the positions of the targets from greenhouses and the ground.

Table 6.1: Statistics of scatterers with TC> 0.6 - Greenhouses- Nieuwerkerk Aan Den IJssel -Heights analysis. Greenhouses with greater than 40 points are listed

Greenhouse No.	No. of Points	Mean [m]	IQR [m]	Std dev [m]
1	108	1.401	4.767	4.339
2	258	1.256	4.717	4.938
8	66	-0.209	4.321	3.933
9	46	0.189	4.052	4.795
11	40	1.961	5.168	4.945
13	86	1.602	4.851	7.695
15	115	1.172	4.793	4.919
16	60	2.123	3.02	2.947
17	44	2.227	4.452	6.015
18	211	4.949	2.703	2.792
20	89	3.219	4.169	3.934
21	103	2.239	4.415	5.306
22	91	2.092	5.324	4.829
23	73	0.302	3.863	3.245
24	76	0.124	5.199	4.045
26	76	0.01	3.488	3.72
27	84	0.685	4.608	3.893
31	43	-1.234	6.672	7.993
32	40	-1.205	4.282	3.958

Table 6.2: Statistics of scatterers with TC> 0.6 - Buildings- Nieuwerkerk Aan Den IJssel -Heights analysis. Buildings with greater than 20 points are listed

Building No.	No. of Points	Mean [m]	IQR [m]	Std dev [m]
1	32	6.812	4.147	3.599
2	29	3.142	6.209	5.487
3	28	4.041	4.305	4.363
4	26	1.87	4.583	3.922
5	22	4.873	3.414	4.45
25	25	5.333	3.769	3.136
30	31	5.374	6.348	3.782

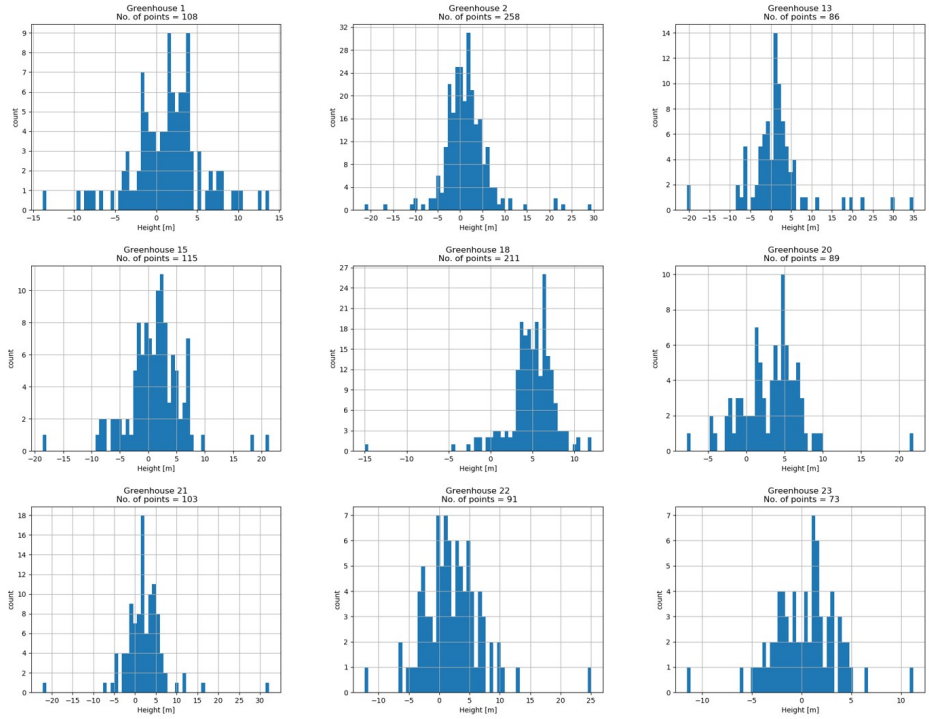

Figure 6.30: Histograms of residual heights from pixel scatterers of 0.6 minimum TC for multiple Greenhouses in the Nieuwerkerk Aan Den IJssel Area

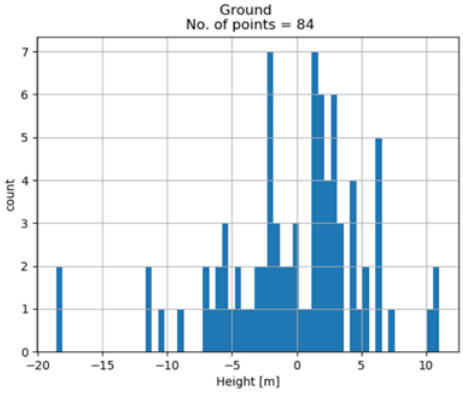

Figure 6.31: Histogram of the residual heights from ground pixel scatterers in the Nieuwerkerk Aan Den IJssel Area - Mean: -0.24m; IQR: 5.916m; Std dev: 5.495m

PSs OF NIEUWERKERK AAN DEN IJSSEL

Since analysis of all pixels by merely imposing a threshold on the temporal coherence is expected to have noisy data, PSs have also been considered. These PSs were processed by imposing an amplitude stability index threshold of 0.7 and a temporal coherence of 0.6. The visualisation of the residual heights of the PSs for one of the greenhouses (Greenhouse no. 18) is shown in figure 6.32a, where it can be seen that the PSs are spread across one portion of the greenhouse. The residual heights have a standard deviation of 2.79m. To ascertain if the standard deviation is caused due to scatterers from targets of different heights within the greenhouse or if it is due to noise (or scatterers from the facade), a comparison was made with buildings of the area. Figure 6.32b shows that scatterers on the buildings also have residual heights that are not constant. Histograms for the buildings have not been added here owing to the low number of scatterers. From the combined visualisation as shown in figure 6.32, it can be inferred that the scatterers from the greenhouse are most likely targets on the roof or the facade of the greenhouse.

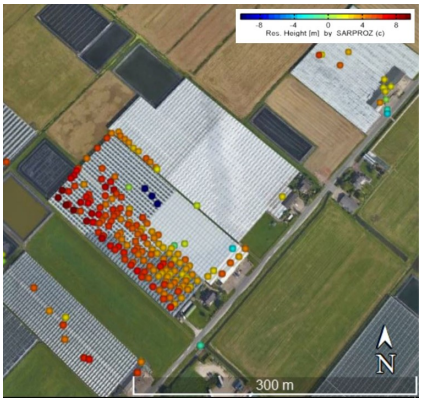

(a) Greenhouse no. 18 - Nieuwerkerk aan den IJssel

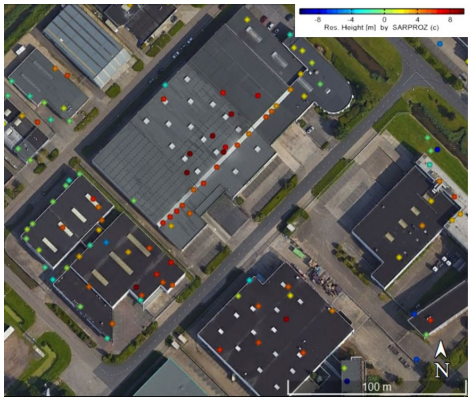

(b) Buildings in Nieuwerkerk aan den IJssel

Figure 6.32: Visualization of residual heights for PSs in the region of Nieuwerkerk aan den IJssel

6.4. HEIGHTS ANALYSIS - WESTLAND

It is seen that there was an insufficient number of PSs detected on buildings in the region of Nieuwerkerk aan den IJssel. Therefore the region of Westland is used to compare the residual heights between greenhouses and buildings since the region provides ample scope for analysing many greenhouses and buildings. Moreover, DSs are also used to verify if spatial complex averaging of the interferometric phase is suitable for extracting targets that do not pass the thresholds of high amplitude stability that was required for the selection of PSs. Such spatial averaging is useful when there is uncorrelated noise due to temporal or volume decorrelation. Sources of temporal decorrelation could be the opening and closing of windows on the roof of the greenhouse and sources of volume decorrelation could be attributed to the operations within the greenhouse and the varying nature of objects present inside the structures from time to time.

PSs and DSs were processed with both the ascedning as well as descending tracks of Radarsat-2. The thresholds used for PSs are a minimum amplitude stability index of 0.75 and a temporal coherence of 0.6. The thresholds used for DSs are a minimum spatial coherence of 0.85 and a temporal coherence of 0.6. The analysis of the whole area of westland was done in a single project due to which the threshold imposed on the spatial coherence for DSs is high (in order to limit the computation time for an area of over 100 sq km).

Tables 6.3 and 6.4 show the ascending track PSs and DSs for greenhouses and buildings respectively. The measures of spread - standard deviation, interquartile range (IQR) and the range are similar for the PSs and the DSs of greenhouses and buildings. The histograms for the greenhouses are shown in figures 6.33 to 6.36 and the histograms for the buildings are shown in figures 6.37 to 6.39. Since the measures of spread are comparable between greenhouses and buildings for both PSs and DSs, it can be inferred that the scatterers are most likley picked up from targets on the roof or the facade of the greenhouses.

Additionally, a spatial plot of the residual heights for Greenhouse 10 is visualised as shown in figure 6.40 where it can be seen that the residual heights estimated are comparable to the visual estimate of the height of the greenhouse as shown in figure 6.40.

Tables 6.5 and 6.6 show the descending track PSs and DSs for greenhouses and buildings respectively. It is noticed that the mean heights for DSs in the case of descending track data, is higher by 10-15m and the histograms of the residual heights are shifted consistently by this bias for the DSs when compared to the PSs. This is likely due to the propagation of phase correction from the reference point to all the other scatterers and the analysis shows that the reference point for the PSs is not a suitable reference point for DSs. When one of the greenhouses (greenhouse 8) was re-processed on an individual area scale with a different reference point it is seen that the residual heights of the PS and DS is comparable. The results are elaborated later in section 6.4.1. The histograms of the descending track directions presented in section A.3.2.

It can be seen that the the scatterers seen in buildings are visible in both ascending

Table 6.3: Statistics of PSs and DSs- Greenhouses – Westland full area analysis - Ascending track direction

	PS				DS			
Greenhouse No.	**No. of Points**	**Mean [m]**	**IQR [m]**	**Std dev [m]**	**No. of Points**	**Mean [m]**	**IQR [m]**	**Std dev [m]**
1	89	-0.103	1.722	1.383	83	2.037	1.746	1.477
2	48	0.651	2.86	2.161	45	3.252	2.566	2.029
3	198	0.988	2.848	2.054	180	2.816	2.672	2.205
4	452	1.652	1.878	3.593	462	4.391	1.577	1.614
5	75	-1.588	1.571	1.239	77	0.984	1.865	3.243
6	88	-2.369	1.773	1.509	82	-0.316	1.81	1.869
7	9	-0.875	3.547	2.172	9	1.125	5.381	3.712
8	2	1.584	0	4.754	2	4.628	0	1.462
9	154	-2.936	2.366	2.766	149	-0.749	2.622	3.324
10	190	10.282	2.187	3.719	125	13.124	2.012	1.644

Table 6.4: Statistics of PS and DS - Buildings – Westland full area analysis - Ascending track direction

	PS				DS			
Building No.	**No. of Points**	**Mean [m]**	**IQR [m]**	**Std dev [m]**	**No. of Points**	**Mean [m]**	**IQR [m]**	**Std dev [m]**
1	50	5.672	2.394	1.864	75	6.085	3.645	2.418
2	42	6.385	2.32	3.173	47	8.384	2.992	2.625
3	26	0.422	4.795	3.657	23	4.003	3.864	3.286
4	388	0.086	4.798	5.019	372	1.95	4.487	4.789
5	195	4.069	2.49	4.019	231	4.903	3.21	4.943
6	48	2.374	10.39	7.111	48	5.486	4.578	4.803
7	43	5.308	3.089	5.754	46	7.937	2.727	2.578
8	125	2.293	2.855	2.693	124	4.481	3.529	3.176
9	33	0.286	2.513	2.32	36	0.747	6.077	4.332
10	68	0.23	4.24	5.91	67	-0.06	5.166	4.365
11	27	1.253	4.817	4.797	39	1.657	9.254	5.149

Table 6.5: Statistics of PS and DS - Greenhouses– Westland full area analysis - Descending track direction

	PS				DS			
Greenhouse No.	**No. of Points**	**Mean [m]**	**IQR [m]**	**Std dev [m]**	**No. of Points**	**Mean [m]**	**IQR [m]**	**Std dev [m]**
7	167	4.289	6.52	4.059	136	16.769	3.442	2.833
8	347	2.931	6.592	4.313	303	16.018	4.428	3.301

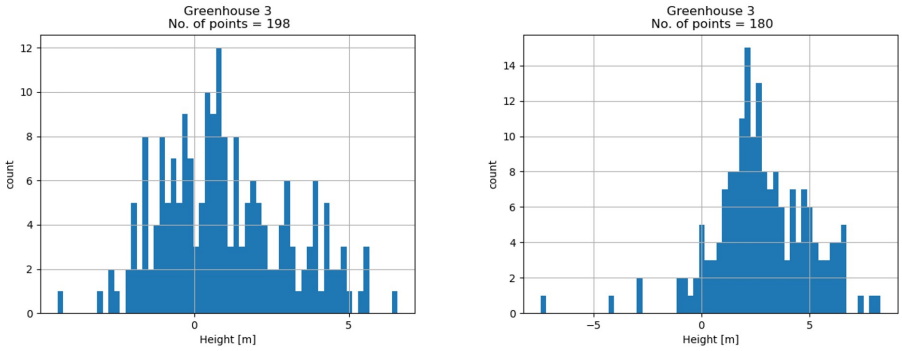

Figure 6.33: Greenhouse 3 Heights analysis in Westland full Area - Ascending Track Direction - Left: PS, Right: DS

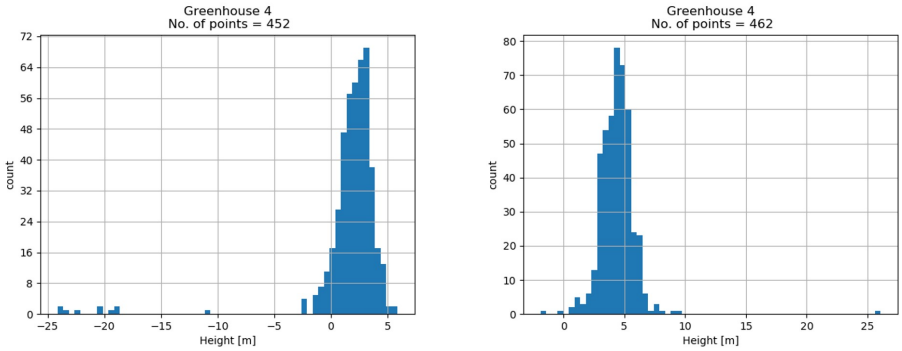

Figure 6.34: Greenhouse 4 Heights analysis in Westland full Area - Ascending Track Direction - Left: PS, Right: DS

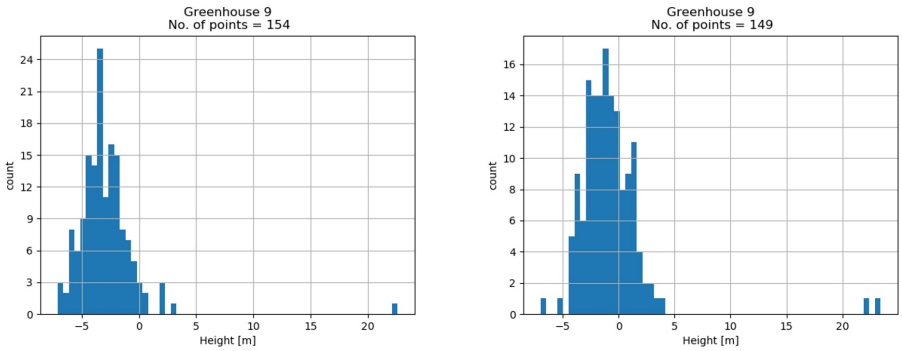

Figure 6.35: Greenhouse 9 Heights analysis in Westland full Area - Ascending Track Direction - Left: PS, Right: DS

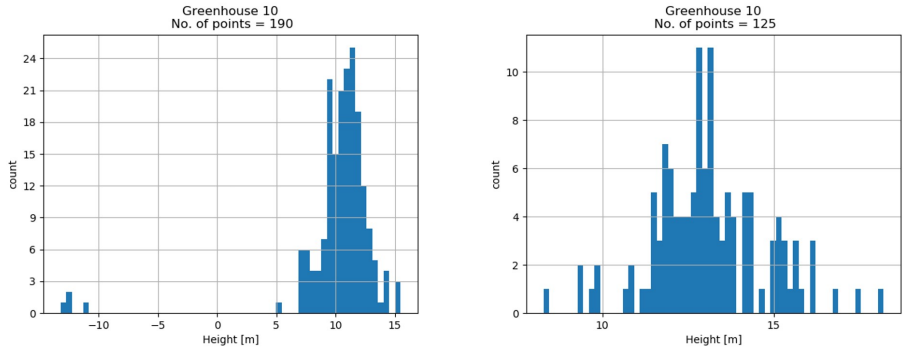

Figure 6.36: Greenhouse 10 Heights analysis in Westland full Area - Ascending Track Direction - Left: PS, Right: DS

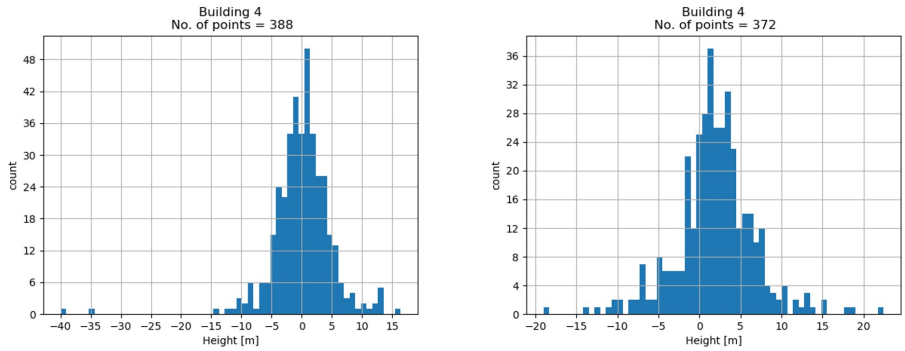

Figure 6.37: Building 4 Heights analysis in Westland full Area - Ascending Track Direction - Left: PS, Right: DS

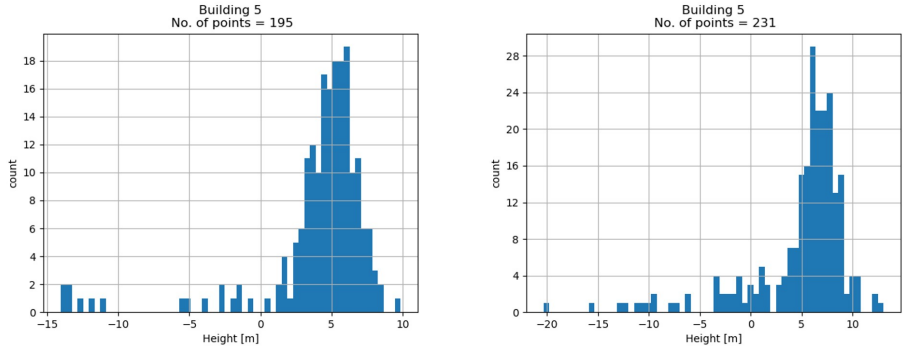

Figure 6.38: Building 5 Heights analysis in Westland full Area - Ascending Track Direction - Left: PS, Right: DS

and descending track, whereas for greenhouses, the presence of scatterers are sensitive to the track direction. This is likely to be a consequence of the difference in the nature

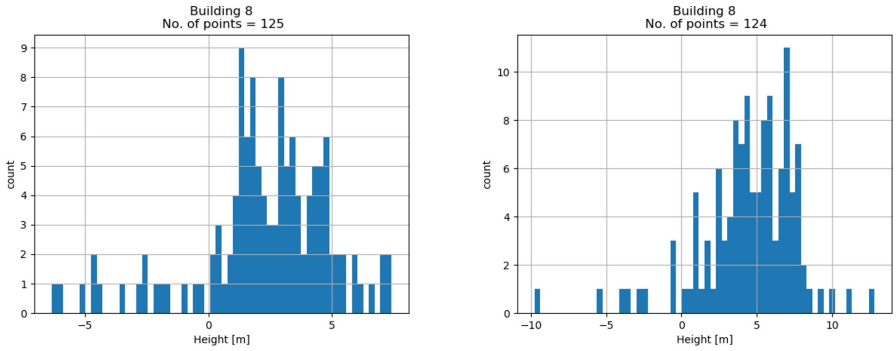

Figure 6.39: Building 8 Heights analysis in Westland full Area - Ascending Track Direction - Left: PS, Right: DS

Table 6.6: Statistics of PS and DS - Buildings– Westland full area analysis - Descending track direction

	PS				DS			
Building No.	**No. of Points**	**Mean [m]**	**IQR [m]**	**Std dev [m]**	**No. of Points**	**Mean [m]**	**IQR [m]**	**Std dev [m]**
1	8	3.156	4.024	2.799	6	15.501	2.089	2.072
2	25	5.615	4.168	2.947	15	15.948	3.63	3.943
3	88	7.98	4.244	2.917	69	19.818	3.448	3.83
4	251	-0.191	4.404	4.473	225	11.313	5.211	5.397
5	65	6.427	4.297	2.82	54	17.523	4.964	5.574
6	34	9.142	3.44	2.908	24	19.988	5.773	4.804
7	10	6.339	2.164	1.461	9	18.864	3.743	2.378
8	30	2.859	2.862	4.313	41	14.186	3.674	4.04
9	104	2.015	5.114	3.393	81	14.925	5.735	5.179
10	133	2.255	4.099	3.729	99	15.543	4.309	4.181
11	45	5.119	3.966	3.957	36	15.755	4.123	3.93

of targets detected as scatterers from greenhouses and buildings. If scatterers get detected regardless of the orientation of the beam with respect to the structure, they are most likely more 3 dimensional (like ventilation ducts or tanks on buildings) whereas if scatterers are sensitive to the relative orientation of the beam with the structure, they are most likely elongated or linear (frames and rods of the roof of greenhouses, pipes on the facade of the greenhouses).

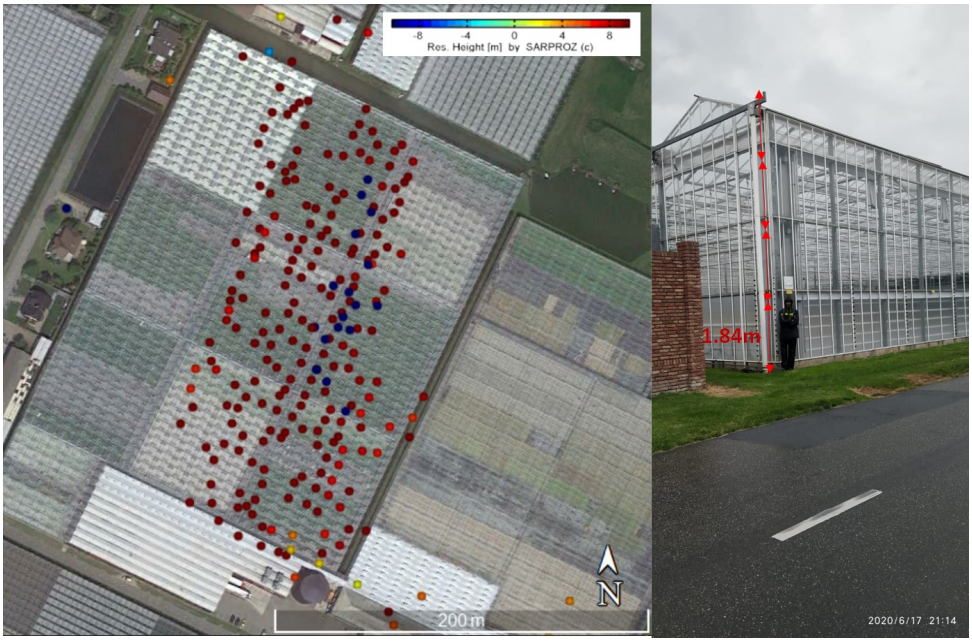

Figure 6.40: Residual heights of the persistent scatterers for greenhouse 10 (L), investigation of greenhouse's height from field visit (R)

6.4.1. COMPARISON OF PSS WITH DSS OF LOWER SPATIAL COHERENCE THRESHOLD (0.75)

This is an investigation of the positions of te DSs by taking 3 greenhouses with high density of PSs and DSs into account. Greenhouses 4 and 9 were processed in a single project owing to their proximity . There is a common reference point for both greenhouses. Greenhouse 8 was processed separately since it was located further away.

3 INDIVIDUAL GREENHOUSES

The statistics of the residual heights for the 3 greenhouses is shown in table 6.7. The histograms of the residual heights for PSs and DSs shown in figures 6.41, 6.42 and 6.43 were made by imposing two filtering conditions to remove outliers:
i) Temporal Coherence > 0.60
ii) -30m < residual height < 30m

From figures 6.41, 6.42 and 6.43, it can be seen that the number of DSs in all three greenhouses is roughly 10 times higher. Also, the residual heights of DSs show the same range as that of the PSs. The Reference point for greenhouse 4 and 9 is at the site of a house as shown in figure 6.44.

On visiting greenhouse 4, it was seen that its height was slightly higher than that of a two storey building (2x3.2m) as shown in figure 6.45. The peak in the histogram of

Table 6.7: Statistics of PSs and DSs for 3 individual greenhouses

		PS				DS		
Greenhouse No.	No. of Points	Mean [m]	IQR [m]	Std dev [m]	No. of Points	Mean [m]	IQR [m]	Std dev [m]
4	450	6.125	1.955	5.997	4425	5.265	1.66	4.691
8	420	2.856	6.582	4.558	3174	3.335	7.388	4.771
9	101	2.456	2.02	4.153	1305	1.983	1.81	3.564

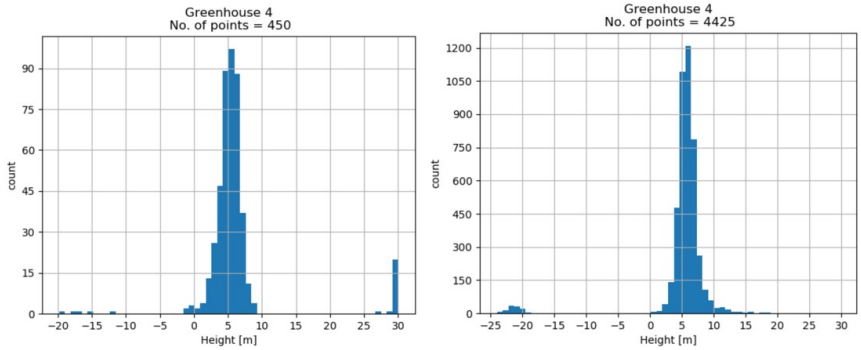

Figure 6.41: Greenhouse 4 Heights analysis on individual scale - Ascending track direction - Left:PS, Right DS

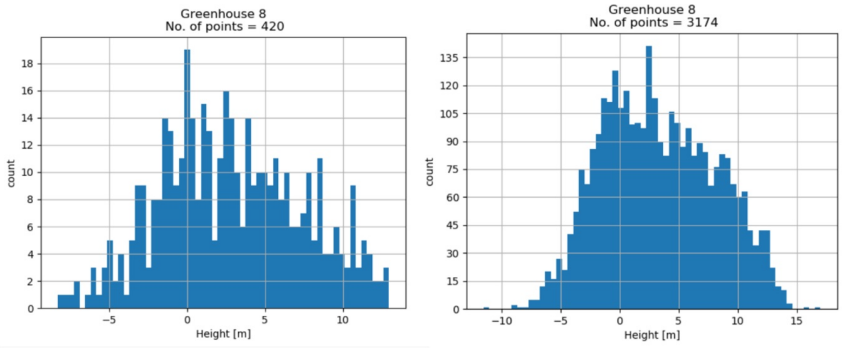

Figure 6.42: Greenhouse 8 Heights analysis on individual scale - Descending track direction - Left:PS, Right DS

greenhouse 4 as shown in figure 6.41, is at roughly 5.5m. Considering that the reference point is taken from a scatterer whose maximum height (since the scatterer could also be on the facade) could be that of a one storey building, it is reasonable to infer that the peak height of 5.5m corresponds to the roof of the greenhouse. Visualizations of the residual heights of the scatterers of greenhouse 4 is shown in figure 6.46a and figure 6.46b respectively. The scatterers have been primarily identified from the central portion of the greenhouse. From the visualisation, it can be seen that there are not a lot of scatterers that could have been picked up from the facade of the greenhouse.

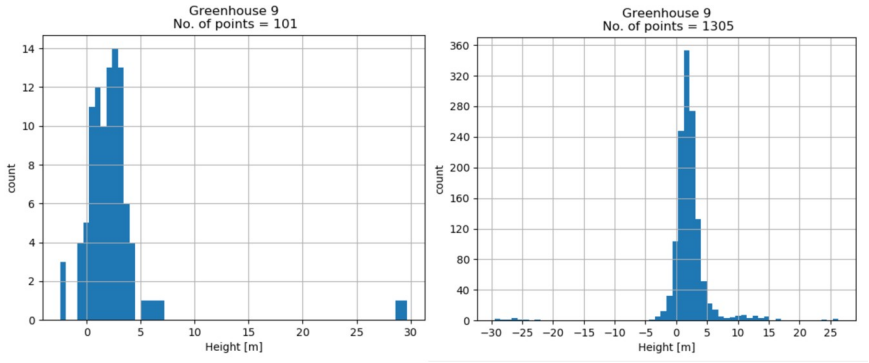

Figure 6.43: Greenhouse 9 Heights analysis on individual scale - Descending track direction - Left:PS, Right DS

Figure 6.44: Left: Reference point for the project – for greenhouse 4 and greenhouse 9. The greenhouse on the left is greenhouse 4 – Image source – Google street view

(a) Greenhouse 4 Site picture - slightly higher than a 2 storey building)

(b) Greenhouse 9 Site picture - slightly lower than a 2 storey building)

Figure 6.45: Site visit images of Greenhouse 4 and 9

From table 6.7 it can be also be seen that the IQR for greenhouse 4 and 9 are similar but greenhouse 8 has a larger measure of spread. This can be attributed to the physical structure of the greenhouses that set them apart. The author has not visited greenhouse

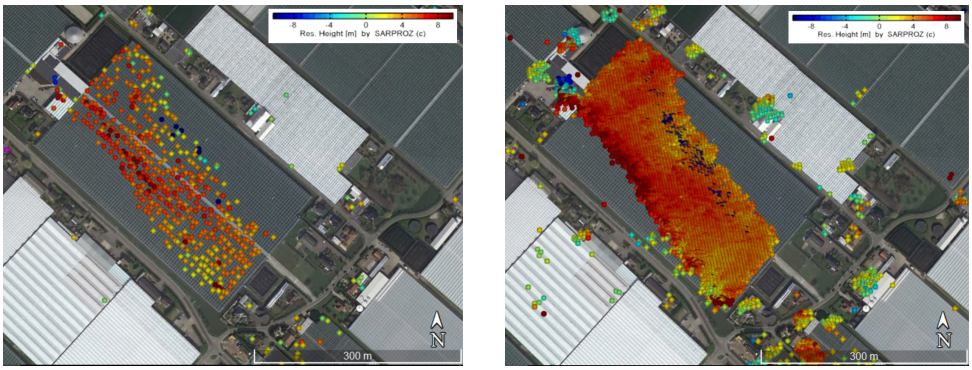

(a) Persistent scatterers (b) Distributed scatterers

Figure 6.46: PS and DS heights over greenhouse 4.

Table 6.8: The statistics of the PS and DS for Greenhouse 'Westland A' and the two buildings

	PS – Amp stability >0.6, TC >0.6				**DS Sp C >0.45, TC >0.6**			
	No. of Points	**Mean [m]**	**IQR [m]**	**Std dev [m]**	**No. of Points**	**Mean [m]**	**IQR [m]**	**Std dev [m]**
GH Westland A	165	-0.032	4.84	4.651	901	-1.197	4.39	4.111
Building 1	556	0.001	5.155	7.013	3541	1.011	4.48	5.929
Building 2	251	3.36	4.43	5.41	1492	3.494	4.565	5.598

8 but on other field visits it was seen that some greenhouses have larger variations in the heights of their roof trusses than others. The ratio of scatterers picked up from the facade of the greenhouse compared to the roof of the greenhouse also affects the spread in their residual heights.

COMPARISON WITH BUILDINGS

Buildings with concrete roofs serve as references for comparison since radar signals cannot penetrate the building walls and therefore the spread of the histograms can be used for comparison. In order to understand why the spread of the residual heights is higher for some structures compared to others, PSs and DSs of two buildings near greenhouse 'Westland A' are analysed. The reference point for this project was from a two storey building and the greenhouse appears to have a height that is lesser than that of a two storey building from Google street view. The layout of the greenhouse and the buildings are shown in figure 6.47.

Figure 6.47: Layout of the buildings analysed, the reference point is highlighted in red

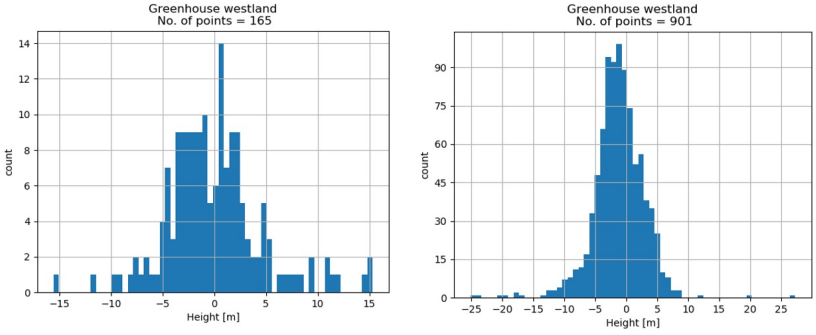

Figure 6.48: 'Greenhouse Westland A' used for comparison with buildings - Left: PS histogram, Right: DS histogram

The histograms of the residual heights of PSs and DSs for greenhouse 'Westland A' are shown in figure 6.48. The hitograms of the residual heights of PSs and DSs for the two buildings are shown in 6.49 and 6.50 respectively. The residual heights of the PSs and DSs are similar. It can be also be seen that the measures of spread (both IQR as well as Std dev) are comparable for the buildings and for greenhouse 'Westalnd A' from table 6.8. Furthermore, the IQR's of the buildings are not significantly higher than the IQR of greenhouse 8. To understand the reason for the measures of spread, visualizations are shown in figure 6.51 and figure 6.52. It can be seen that the scatterers of lower heights can be seen near the edges of the buildings and in portions where backscatter from ground could be a possibility. The comparison of the measures of spread between the greenhouses (greenhouse 4,8,9 and Westland A) and the buildings supports the inference that the radar signal does not penetrate the roofs of the greenhouses.

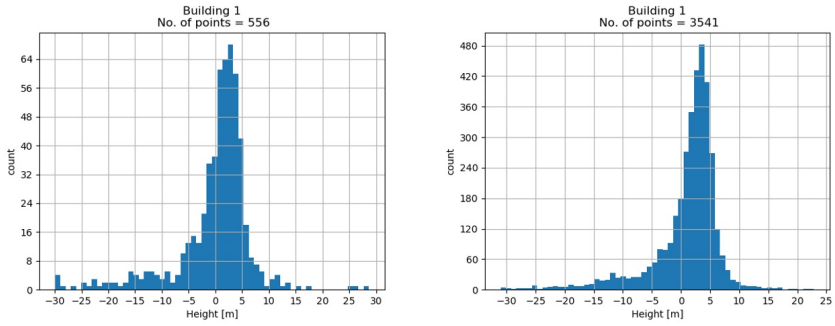

Figure 6.49: Building 1 at Westland - Left: PS histogram, Right: DS histogram

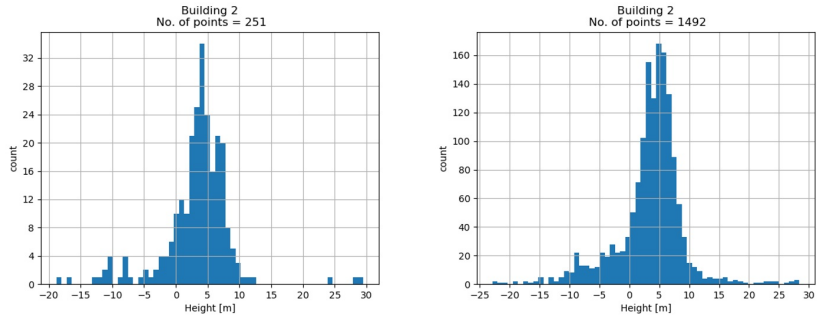

Figure 6.50: Building 2 at Westland - Left: PS histogram, Right: DS histogram

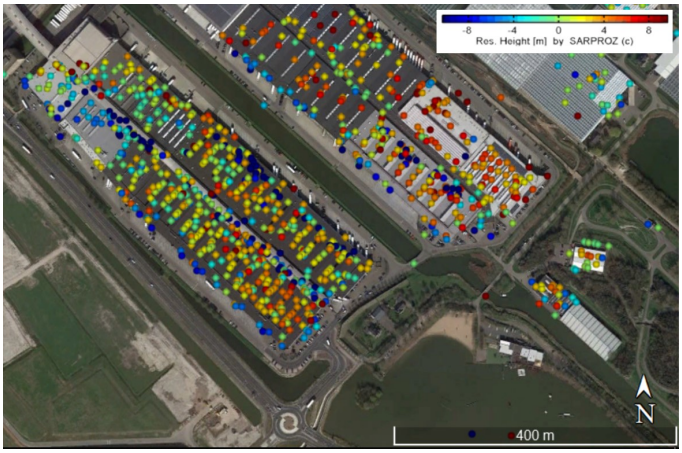

Figure 6.51: Persistent scatterers of buildings 1 and 2

6.4.2. CONCLUDING REMARKS FOR HEIGHTS ANALYSIS

Based on the analysis of comparing residual heights of PSs and DSs for the purpose of determining the positions of scatterers, the following conclusions can be made:

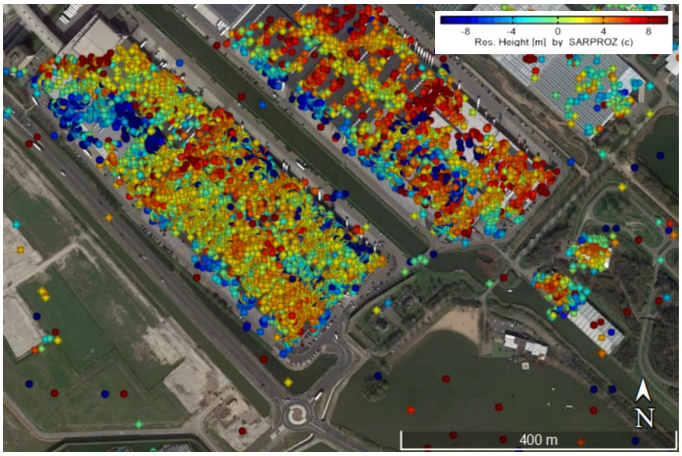

Figure 6.52: Distributed scatterers of buildings 1 and 2

1. Only greenhouses that have high number (>40) of scatterers have been used for the analysis, since statistical inferences can be drawn only from a large dataset. However, this affects the conclusions that can be drawn to answer a generalised question of *"From what portions of a greenhouse is radar signal getting back-scattered from"*. Greenhouses with a large number of scatterers may have components in their physical structure that set them apart from the rest of the greenhouses. For example, a higher density of metallic objects near the roof of the greenhouse will make it difficult for stable interferometric phases to be detected from objects inside the greenhouse.

2. From the results shown in section 6.4, it be justified that DSs having heights more than that of PSs may not only be due to the nature of the DSs. It may also be due to the reference point and the manner in which phase correction is applied to all the remaining scatterers. For example, 'Greenhouse Westland A' shown in figure 6.48, has DSs whose mean residual height is lesser than that of PSs. Thus it can be seen that the residual heights of the DSs are either higher (in most cases) or lower than that of the PSs. In every case, the magnitude of increase or decrease of the residual heights of DSs when compared to PSs, is similar for the all greenhouses/buildings that were processed with the common reference point specific to the project.

3. In case of the 3 greenhouses that have been studied individually, range of residual heights values of the PSs and the DSs are comparable to that each other. The measures of spread (IQR, standard deviation) of the residual heights of PSs and DSs for greenhouses are comparable to buildings. This is indicative of the similarity in the targets detected as PSs and DSs for both greenhouses as well as buildings. Since targets from buildings are known to be on the surface (roof or facade), it can be inferred that the scatterers from greenhouses are also on the roof or facade.

4. The precision of heights from InSAR measurements are in the order of meters.

Moreover, since DSs are formed from interferograms of smaller baselines, accuracy of the estimated heights may also suffer. Moreover, DSs are useful for the analysis of areas that have suffered temporal decorrelation but is not very useful when artefacts being analysed are correlated in space. Sources of error arise from atmospheric turbulence (when large areas are analyed - eg Westland big area). All comparisons made in this thesis are internally consistent where comparisons are made between PSs and DSs only if they have a common reference point (at least common SAR coordinates), same track direction of the images are used and the same minimum filter on temporal coherence (0.6) is imposed.
The results reveal that the residual heights of both PSs as well as the DSs are similar.

Some context can also be provided by understanding the physical operations in the greenhouses with regard to thermal sheets beneath the roofs of the greenhouses. The opening and closing of thermal polymer sheets are governed by the optimum temperature requirements and the crop season. Since PSs are characterized by stable phases in all the interferograms of the stack, it is unlikely that the scatterers can be picked up from targets beneath these sheets that cover the glasshouses near the roof. And it is seen in the case of DSs that the distribution of the residual heights is similar to that of the PSs. Therefore, it can be concluded that they are also from targets on the roof of the greenhouses.

6.5. THERMAL SIGNAL

It was seen from PSI projects which makes use of single master stacks, that the coherence between image pairs follows a seasonal pattern as shown in figure 6.53 for the big area analysis of Westland and Nieuwerkerk aan den IJssel.

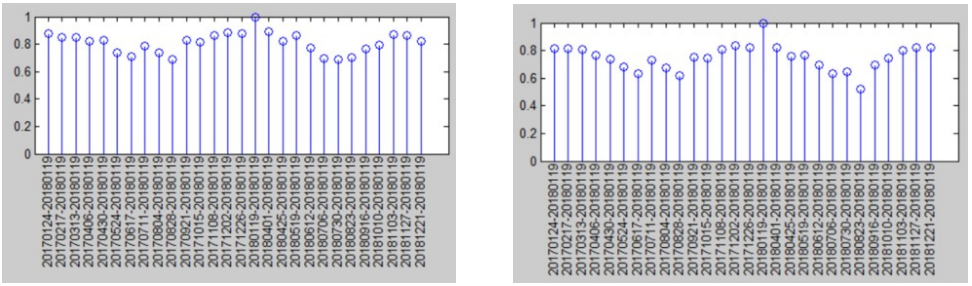

(a) Nieuwerkerk Aan Den IJssel Area (>6sq km)

(b) Westland Big Area (100 sq km)

Figure 6.53: Temporal coherence between image pairs with a single master

To verify if the seasonal pattern in coherence is indeed due to the effect of thermal contributions of expansion and contraction, and not due to other reasons (like operations induced by human activity), the master image was changed from an image in January to an image in July. From the coherence between image pairs shown in figure 6.54, it can be seen that the seasonal pattern is still observed, though somewhat subdued, most likely due to the master image being chosen towards one end of the time series of the data stack.

An experiment was therefore performed to estimate the thermal expansion in addition to heights and deformation for 'Greenhouse Westland A'. For this the analysis was done using the descending track direction, since it would also serve as a means to compare the amount of scatterers from two track directions. Additional temperature data was required to be fed into the software and temperature data was obtained for the dates at which descending track Radarsat-2 images were taken (approx 6 am). Figure 6.55 shows the PSs obtained for the project where thermal expansion was estimated and compared with the project where it was not estimated. It can be seen that the estimations of deformation between the two projects is comparable (a difference of 1mm/year in scatterers of temporal coherence > 0.6 is seen) to a large extent and as far as estimating relative subsidence within the greenhouse is considered, a small change in the absolute values of deformation will have little consequence. In fact, it can be seen that for the project where thermal expansion was estimated as an additional parameter, the number of PSs are reduced, most likely due to the lesser temporal coherence of scatterers owing to the estimation of another parameter that the interferometric phase is affected by.

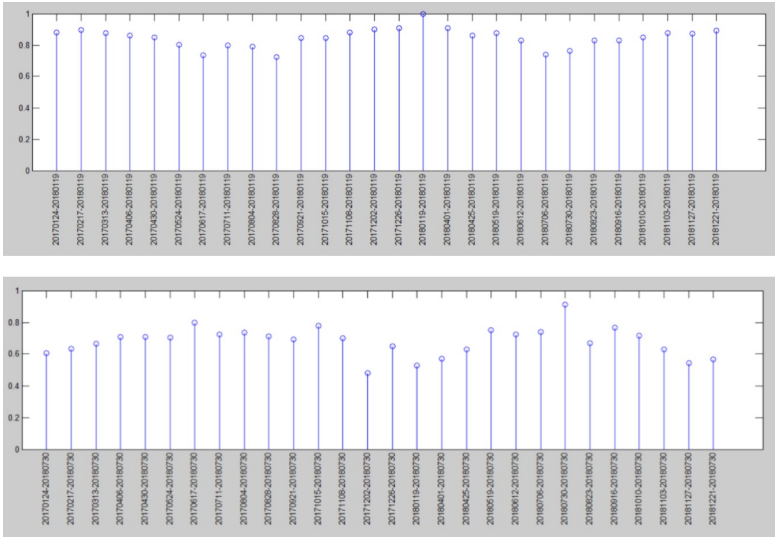

Figure 6.54: Temporal coherence between image pairs with master image in 19-01-2018 (Top) and master image in 30-07-2018 (bottom). Both projects are of Greenhouse Westland A area spanning 2.5 sq km.

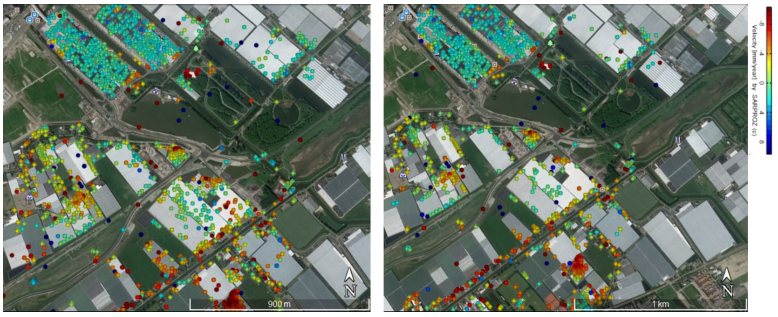

Figure 6.55: Persistent scatterers from descending track for Greenhouse 'Westland A'. Image on the left shows the scatterers without accounting for thermal expansion and the image on the right shows the scatterers when thermal expansion is accounted for.

6.6. SUBSIDENCE IN GREENHOUSE 'WESTLAND A'

A validation map of the subsidence for 'Greenhouse Westland A' was made available from the owner of the greenhouse and is shown in figure 6.56d. Figure 6.56 shows the deformation from PSs and DSs and all of them have a common reference point on a house opposite to the greenhouse. Sub figure 6.56a shows scatterers obtained as result of processing all pixels (after selecting a reference point following a strict threshold for amplitude stability index for the primary network). All pixels were processed but only those with temporal coherence greater than 0.6 are visualised. For the initial trials of PS processing, PSs were first analysed with an amplitude stability index of 0.75 and then reduced gradually to check that a compromise is achieved between seeing informative scatterers on the greenhouse and not seeing noisy scatterers on the surrounding fields and water. Figure 6.56b shows the visualisation of such PSs with an amplitude stability index of 0.6. Figure 6.56c shows DSs which most closely matches the areas of damage (as indicated by the greenhouse owner) compared to the other project trials. For the DS analysis various trials were run before arriving at the threshold of 0.45 for spatial coherence. Additionally, it can be noticed from all the three experiments, that the left most greenhouse structure has scatterers indicating more subsidence than the central greenhouse structure. This however, was not verified by the greenhouse owner.

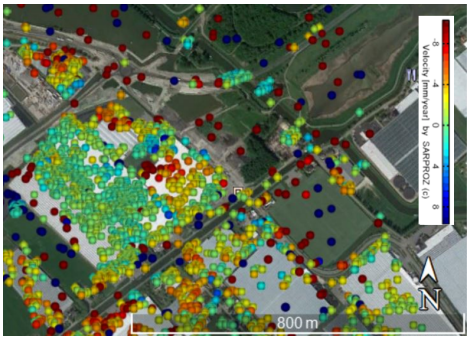

(a) All pixels with TC > 0.6

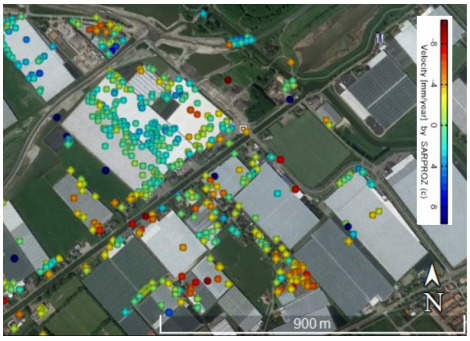

(b) PSs with amplitude stability > 0.6 and TC > 0.6

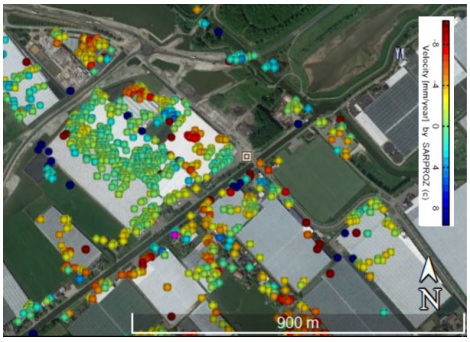

(c) DSs with spatial coherence > 0.45 and TC > 0.6

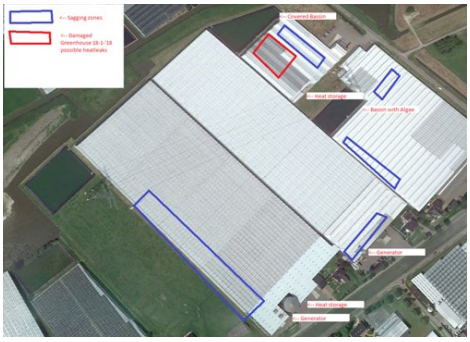

(d) Greenhouse owner damage map with blue highlighting regions of subsidence and red highlighting damage area

Figure 6.56: All scatterers here have been processed with Radarsat-2 ascending track data .

7

CONCLUSIONS AND RECOMMENDATIONS

This chapter presents the conclusions of the research question and recommendations for future. The research questions introduced in the beginning in chapter 1 are discussed.

7.1. CONCLUSIONS FOR THE RESEARCH QUESTIONS

The main research question '*Can InSAR techniques be used to estimate deformation in greenhouses?*' is answered after answering the sub questions.

1. *In a scene covering greenhouses, from what components of the greenhouse is the radar signal getting back-scattered from?*

   The InSAR analysis was performed with PSs and DSs of RadarSat-2 data. Comparisons of scatterer heights have been made between greenhouses and buildings with the assumption that the radar signal does not penetrate into the buildings. Only highly coherent greenhouses have been analysed where the minimum number of scatterers present is 40. The histograms of heights for PSs and DSs for most greenhouses follow a bell shaped distribution indicating that there is an evident peak (a height at which most number of scatterers are estimated to be). For the greenhouses visited (Greenhouses 4, 10 in Westland) and checked from Google street view cameras (Greenhouses 15, 18 and 20 - Nieuwerkerk aan den IJssel) this peak height is comparable to the height of the greenhouse. The range of the histograms are similar for PSs and DSs in most cases. This may be because the actual PSs and DSs may be targets that can be detected both as PSs as well as DSs. Bright and coherent PS-pixels with high spatial coherence can be detected as DS pixels. Moreover in cases of datasets like Radarsat-2 and Sentinel-1 where the orbital tube is narrow, DS-pixels which are highly coherent may be detected as PS pixels.

Since the standard deviations for greenhouses and buildings are comparable, the research indicates that most of the scatterers are picked up from the roof or facade of the greenhouses.

2. *Can the deformation observed, be explained with the geotechnical properties of the area?*

   Recall that this question was further subdivided and is answered accordingly,

   (a) With the knowledge of the soil profiles of the area, can assumptions be made on the expected subsidence of the area?

   Data from bore holes, CPT graphs and interpolated spatial maps of bore hole data was used to correlate the type of soil and the extent of subsidence estimated from the InSAR analysis. The areas analysed are Westland, Schiphol and Nieuwerkerk aan den IJssel. In all the areas analysed, a high correlation was seen between the presence of compressible soil layers and the presence of deformation from the InSAR estimates. Moreover, in cases where deformation from the InSAR estimates were not seen, geotechnical data showed presence of incompressible soil layers close to the surface.

   (b) Can the deformation estimated from the InSAR analysis, be explained with the knowledge of the type of foundation of the greenhouse structure?

   The depth of pile foundations were obtained from greenhouse owners. It was seen that the greenhouse owners who experienced settlement had piles whose depths were insufficient to reach the first incompressible sand layer. Moreover, the greenhouse owner who reported to have experienced no problems with settlement also reported the depth of the piles which was sufficient to reach the first incompressible soil layer. From the case of greenhouse 'Westland A' it was also seen that differential settlements occur due to different depths of piles, not all being sufficient to reach the incompressible soil layer. Therefore, the knowledge of the type of the foundation serves as good validation data to see if the estimations of deformation from the InSAR analysis are reasonable.

3. *Can contributions of thermal effects be seen in the InSAR estimations of deformation?*

   Multi temporal InSAR analysis of single master stacks showed that the coherence of image combinations followed a seasonal pattern. This is good evidence to suggest that the thermal component of structures indeed affects the interferometric phase of the scatterers. However, the relative deformations on a spatial scale, observed from the PSs of Greenhouse 'Westland A' did not change significantly after the parameters of estimation included thermal expansion in addition to height and deformation. This observation could be attributed to a full two year analysis

that was conducted and therefore accounting for the seasonal changes that occur annually. Therefore, it is concluded that estimating thermal expansion is not required for estimating relative settlements within greenhouses.

4. *How does the methodology of Persistent Scatter Interferometry compare with Distributed Scatter Interferometry for estimation of deformation in greenhouses?*

   From the analysis of 'Greenhouse Westland A' for which a validation map from the greenhouse owner is available, it is seen that PSs do indicate relative deformation, however, DSs show the regions of damage in all sections the greenhouse except one portion. Therefore, a combination of both PSs as well as DSs is useful to estimate relative settlements within greenhouses.

Overall, InSAR techniques can indeed be used to estimate deformation within greenhouses. However, since a majority of the greenhouses in Westland, contained no or very few PSs, each greenhouse has to be investigated individually for DSs as well. The research conducted in the thesis also highlights the sensitivity of the estimated parameters on the choice of the reference point. Care should be taken to ensure that the point has stable phase as it was seen that a stable reference point for a PS analysis rendered poor results for DS analysis.

In conclusion, for every greenhouse for which estimations of relative subsidence is required, a PS analysis is to be conducted first and is to be followed by a DS analysis if the number of PSs are insufficient to check for differential settlement. This is because a PS analysis is quicker and interpretation of the results are more straightforward.

It was also seen that processing both track directions for Radarsat-2 increased the number of greenhouses from which scatterers could be observed. Also, from the analysis with Sentinel-1 data, it was seen that the density of PSs is lower than that detected using Radarsat-2 on account of the lower spatial resolution of Sentinel-1 data. Despite this, it was seen that PSs were observed from some greenhouses using Sentinel-1 data where very few scatterers were seen using Radarsat-2 data. Therefore, additional datasets have proven to be useful in obtaining higher number of scatterers from which estimations of deformation can be conducted.

7.2. RECOMMENDATIONS FOR FUTURE WORK

The recommendations for further study are enumerated below:

1. The methodology for finding the positions of the scatterers in this project has the main limitation that heights from InSAR measurements alone, have precision in the order of meters whereas deformation has precision in the order of millimeters. Moreover, for distributed scatterers, interferograms of smaller baselines may further affect the accuracy of the estimated heights. Hence, it is recommended that corner reflectors are used in two ways. Firstly a network of corner reflectors placed in the region of analysis increases the accuracy of positioning the scatterer and the knowledge of the absolute height of the reference point helps in ascertaining the

heights of the scatterers [49]. Secondly, it is recommended that corner reflectors be placed at different heights of a greenhouse, one above the roof in one corner and another at the ground level at another corner to check for the passage of radar signals of the greenhouse.

2. The resolution of the external DEM plays a very crucial role in selecting reference points as well as in the estimation of residual heights. Hence, it is recommended that a Lidar based DEM of higher resolution or the DEM from AHN is used instead of SRTM.

3. With respect to choosing the adaptive multi-temporal mask for DSs, in the methodology of this thesis, the AD statistical test was used with a 5x5 pixels grid window. It is recommended that DSs are processing with masks obtained by running statistical tests on linear shapes that resemble rods and frames of the greenhouse roof. This may increase the chances of obtaining better DSs that resemble the physical structures that are monitored, more accurately.

A

APPENDIX

A.1. PROCUREMENT OF GEOTECHNICAL DATA

Bore hole and CPT data was obtained from the Bodem en grondonderzoek tab of the subtsrate data portal in dinoloket [47]. The 'Geologisch booronderzoek' contains the bore hole data and the 'Geotechnisch sondeeronderzoek (BRO)' contains data from CPT tests.

The cross sectional profile from bore hole data can be obtained from the BRO GeoTOP model under the 'Substrate Models' portal. As of 22nd September 2020, version 1.4 is present. The cross sectional profile can be obtained by drawing a line of 1km minimum distance in the interactive map.

A.2. SUPPLEMENTARY RESULTS - GREENHOUSES FACING SUBSIDENCE

The following greenhouses in Westland were identified to be facing subsidence problems.

A

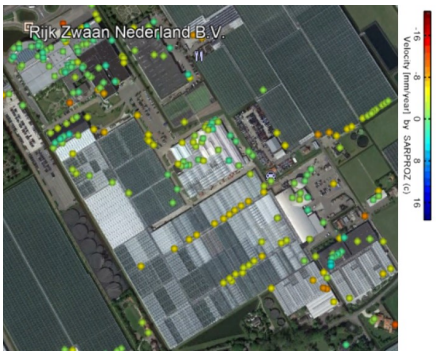

(a) Subsidence between 5-10 mm/year

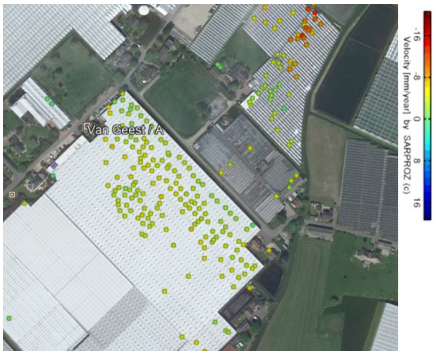

(b) Subsidence between 3-7 mm/year. Greenhouse on the top right :8-10 mm/year

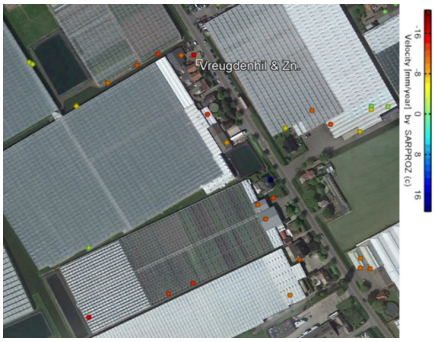

(c) Subsidence between 10-15 mm/year

(d) Subsidence between 5-7 mm/year

(e) Subsidence between 6-12 mm/year

(f) Subsidence between 3-8 mm/year.

Figure A.1: greenhouses in Westland with subsidence problems as estimated by PS InSAR analysis .

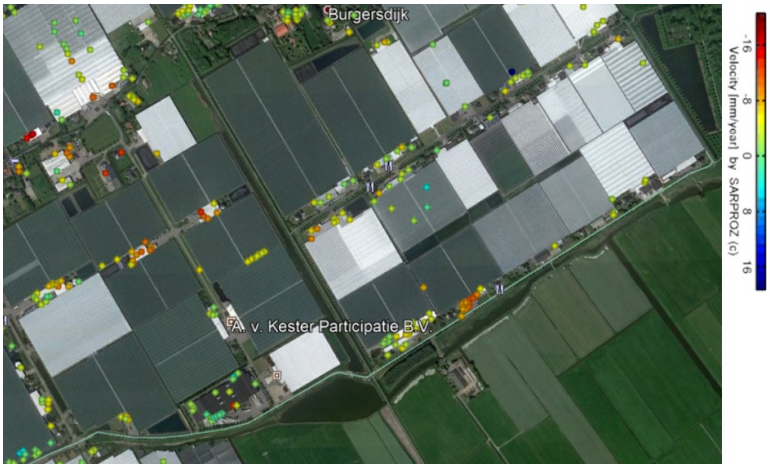

Figure A.2: The above greenhouses appear to be in a subsidence risk prone area where estimated subsidence varies from 5mm/year to 15 mm/year

A

A.3. SUPPLEMENTARY RESULTS - HEIGHTS ANALYSIS

A.3.1. ASCENDING TRACK

This section shows the histograms of the greenhouses and buildings that were not shown in section 6.4 of the chapter 6.

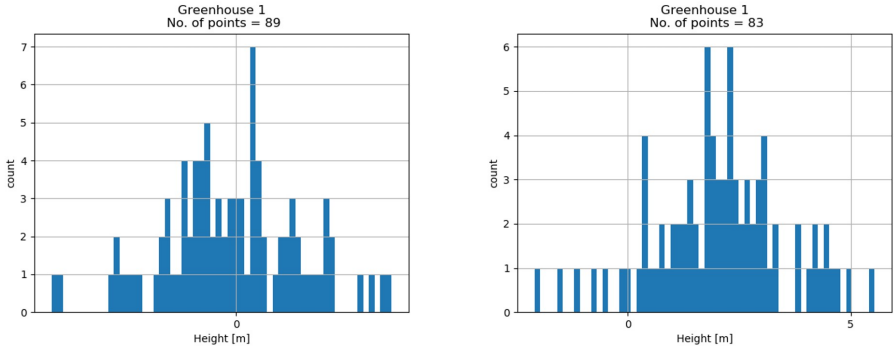

Figure A.3: Greenhouse 1 Heights analysis in Westland full Area - Ascending Track Direction - Left: PS, Right: DS

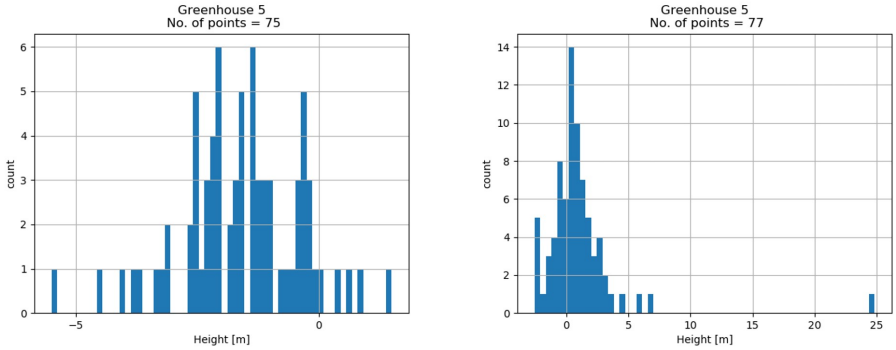

Figure A.4: Greenhouse 5 Heights analysis in Westland full Area - Ascending Track Direction - Left: PS, Right: DS

A.3.2. DESCENDING TRACK

This section shows the histograms of PSs and DSs from greenhouses and buildings for the descending track direction. Note that the reference point for the DSs is not an ideal DS target despite it being suitable for PSs. The mean height for the DSs of the structures are shifted by about 10 to 15m from the PSs heights.

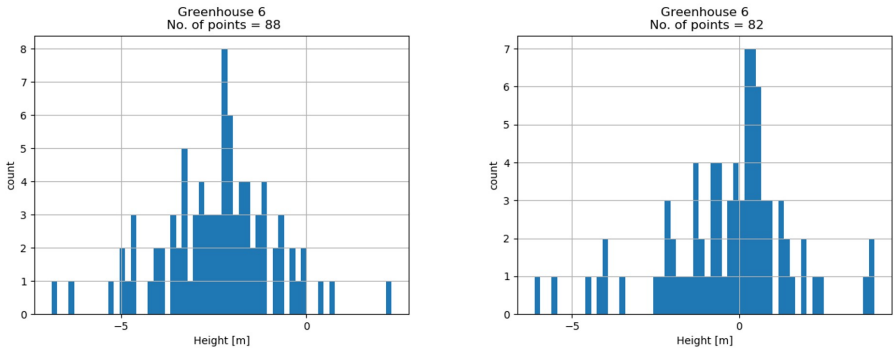

Figure A.5: Greenhouse 6 Heights analysis in Westland full Area - Ascending Track Direction - Left: PS, Right: DS

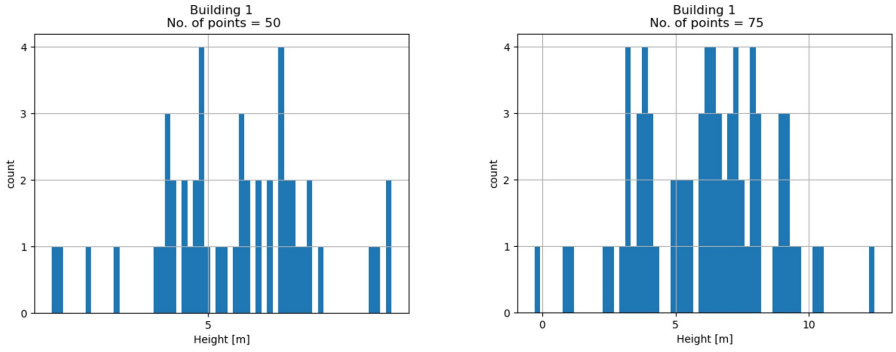

Figure A.6: Building 1 Heights analysis in Westland full Area - Ascending Track Direction - Left: PS, Right: DS

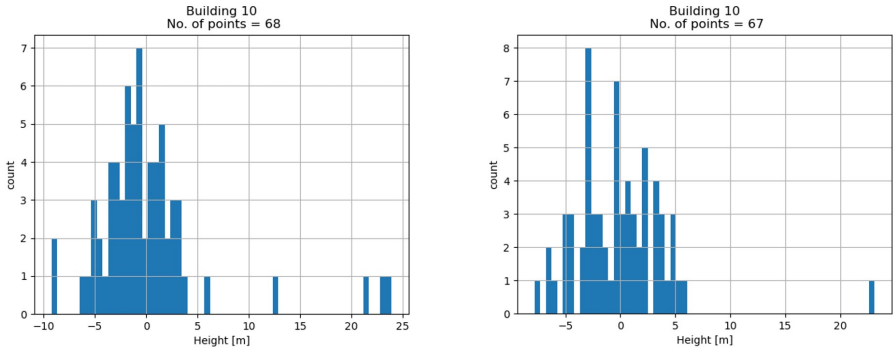

Figure A.7: Building 10 Heights analysis in Westland full Area - Ascending Track Direction - Left: PS, Right: DS

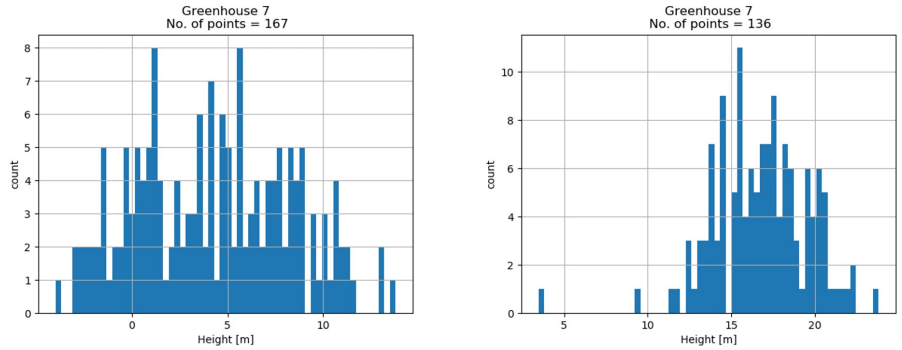

Figure A.8: Greenhouse 7 Heights analysis in Westland full Area - Descending Track Direction - Left: PS, Right: DS

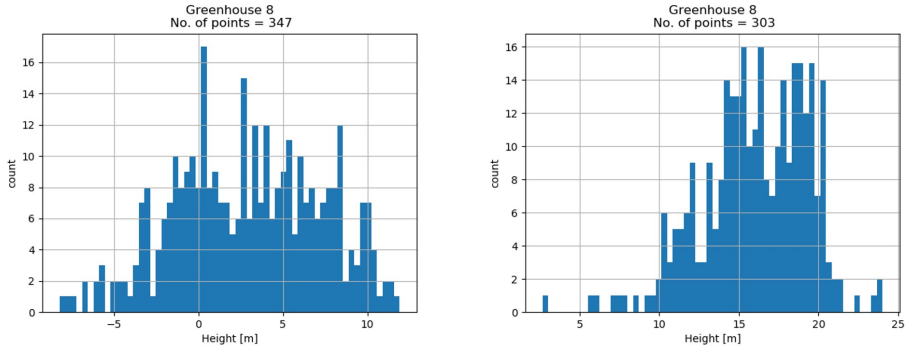

Figure A.9: Greenhouse 8 Heights analysis in Westland full Area - Descending Track Direction - Left: PS, Right: DS

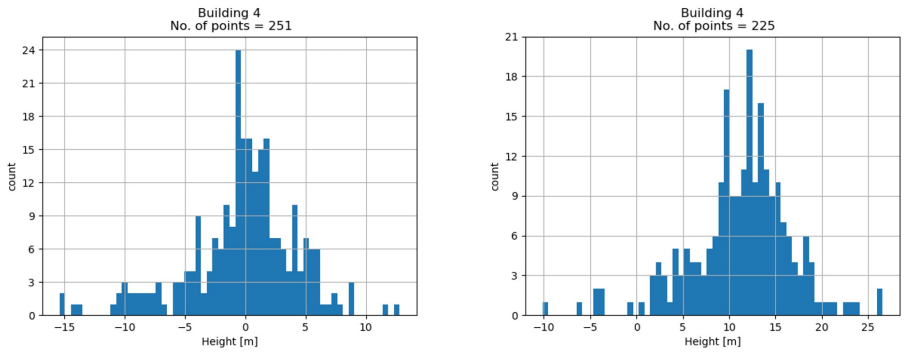

Figure A.10: Building 4 Heights analysis in Westland full Area - Descending Track Direction - Left: PS, Right: DS

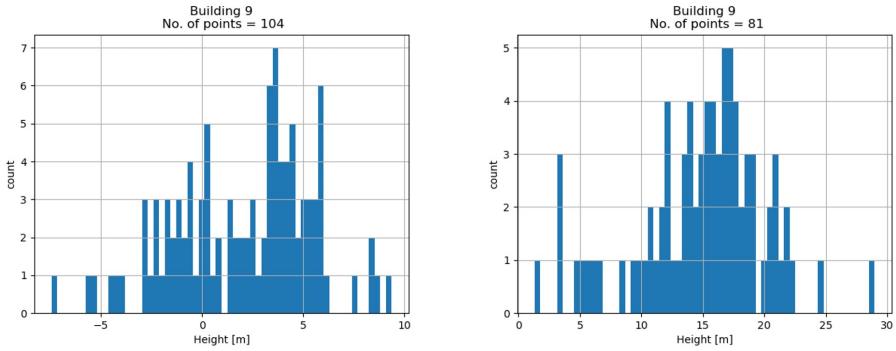

Figure A.11: Building 9 Heights analysis in Westland full Area - Descending Track Direction - Left: PS, Right: DS

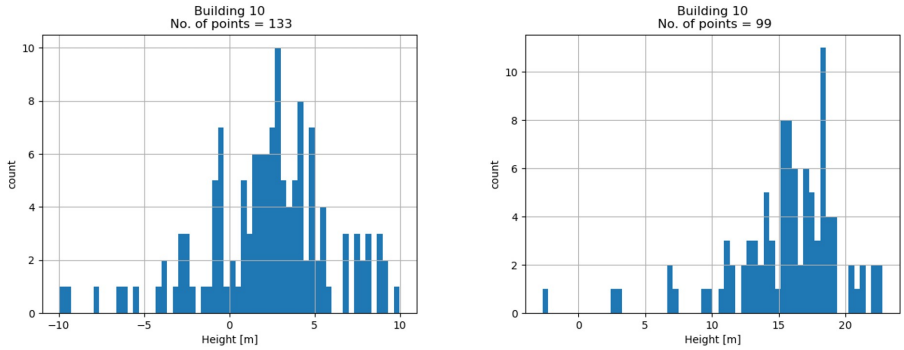

Figure A.12: Building 10 Heights analysis in Westland full Area - Descending Track Direction - Left: PS, Right: DS

A

A.4. FILTERING DATA AND COMPUTATION OF PS/DS HEIGHT STATISTICS

The filtering of data to remove noisy scatterers, the visualisation of histograms and the statistics of the residual heights was done in Python.

```
import pandas
import os
import matplotlib.pyplot as plt
from matplotlib.ticker import MaxNLocator
import matplotlib.ticker as plticker
import numpy as np
import statistics


CSV_FOLDER = r"\GIS DataBase\Urban area_NADI\Building_csv"
STAT_SUM_FILE = os.path.join(CSV_FOLDER, "statistics.csv")

statistics_file_content = []
header_line_stats = "Building no.,No. of Points,Mean,IQR,Std dev"
statistics_file_content.append(header_line_stats)


def get_plot_title(csv_file, count_points):
    filename = os.path.basename(csv_file).split('.')[0]
    title = "Building " + \
        filename.split('_')[2] + "\n No. of points = {}".format(count_points)
    # title = "Greenhouse" + "\n No. of points = {}".format(count_points)
    return title


TEMPORAL_C_THRESHOLD = 0.60

# Constants for the bins sequence
min_height_f = -30
max_height_f = 30
increment_bin = 1


for filename in os.listdir(CSV_FOLDER):
    if filename.lower().endswith('.csv'):
        print(f"Processing {filename}")
        csv_file_path = os.path.join(CSV_FOLDER, filename)
        df = pandas.read_csv(csv_file_path, sep=",")  # making the data frame

        # Filtering the data frame
```

```
max_height = max(df['Height_cor'])
min_height = min(df['Height_cor'])
filter_booleans = (df['Temporal C'] > TEMPORAL_C_THRESHOLD) & (
    df['Height_cor'] <= max_height_f) & (df['Height_cor'] >= min_height_f)
filtered_df = df[filter_booleans]

# Computing statistics of the data frame
count_points = len(filtered_df['Height_cor'])
res_heights = filtered_df['Res. Heigh']

if(count_points < 2):
    print("Less than two data points")

else:

    Q1 = np.percentile(res_heights, 25, interpolation='midpoint')

    # Third quartile (Q3)
    Q3 = np.percentile(res_heights, 75, interpolation='midpoint')

    # Interquaritle range (IQR)
    IQR = round(Q3 - Q1, 3)

    std_dev = round(statistics.stdev(filtered_df['Res. Heigh']), 3)
    mean_pts = round(statistics.mean(filtered_df['Res. Heigh']), 3)

    # Store statistics
    splitname = os.path.basename(csv_file_path).split('.')[0]
    gh_no = splitname.split('_')[2]

    # storing stats with , b/w
    statistics_line = ",".join(
        [gh_no, str(count_points), str(mean_pts), str(IQR), str(std_dev)])
    statistics_file_content.append(statistics_line)

    # Making the bins sequence for the filtered
    bins_sequence_f = np.arange(
        min_height_f, max_height_f, increment_bin)
    bins_no = len(bins_sequence_f)

    # get histogram
    height_hist = filtered_df.hist(column='Res. Heigh', bins=bins_no)
    hist_plot = height_hist[0][0]

    # set axes
```

```
        hist_plot.set_xlabel('Height [m]')
        hist_plot.set_ylabel('count')

        # set the plot title
        plot_title = get_plot_title(csv_file_path, count_points)
        hist_plot.set_title(plot_title)

        # force integer ticks on y axis
        hist_plot.yaxis.set_major_locator(MaxNLocator(integer=True))

        # x axis ticks to be units of 5
        loc = plticker.MultipleLocator(base=5.0)
        hist_plot.xaxis.set_major_locator(loc)

        # save individual graphs as png images
        img_path = os.path.join(CSV_FOLDER, filename[:-4]+'.png')
        hist_plot.figure.savefig(img_path)
        plt.show()

    # save the statistics csv
    with open(STAT_SUM_FILE, 'w') as stat_file:
        for line in statistics_file_content:
            stat_file.write(line)
            stat_file.write("\n")
```

REFERENCES

[1] P. K. Robertson and R. G. Campanella. Interpretation of cone penetration tests. *Canadian Geotechnical Journal*, 20:"718–733", 2011.

[2] Begemann HKS. The friction jacket cone as an aid in determining the soil profile. *Proceedings of the 6th International Conference on Soil Mechanics and Foundation Engineering*, 2:"17–20", 1965.

[3] Ashok K. Jain B.C.Punmia and Arun K. Jain ". *Soil Mechanics and Foundations [Dec 15, 2005] Punmia*. Laxmi Publications, 2005.

[4] Marcus Engdahl. *Multitemporal InSAR in land-cover and vegetation mapping*. PhD thesis, 2013.

[5] Andy Hooper. Persistent scatter radar interferometry for crustal deformation studies and modeling of volcanic deformation. 01 2006.

[6] S. S. Esfahany. Exploitation of distributed scatterers in synthetic aperture radar interferometry. 2017.

[7] Skygeo NCG. Bodemdalingskaart 1.0. `https://bodemdalingskaart.nl/portal/index`, note = Accessed: 10-01-2020.

[8] Vos J. D. The friction jacket cone as an aid in determining the soil profile. *Proceedings of the Second European Symposium on Penetration Testing*, 2:"933–939", 1982.

[9] Education Ministry of Culture and Netherlands Science. Cultural heritage agency of the netherlands, ministry of culture, education and science. `https://landschapinnederland.nl/`, note = Accessed: 01-02-2020.

[10] National Geographic. How the netherlands feeds the world. `https://www.nationalgeographic.com/magazine/2017/09/holland-agriculture-sustainable-farming/`, note = Accessed: 22-02-2020.

[11] R.J. De Glopper and H.P. Ritzema. *Land subsidence*, pages 477–512. Number 16 in ILRI Publication. ILRI, 2006.

[12] Bert L.A. Vermeersen, Aimée B.A. Slangen, Theo Gerkema, Fedor Baart, Kim M. Cohen, Sönke Dangendorf, Matthias Duran-Matute, Thomas Frederikse, Aslak Grinsted, Marc P. Hijma, and et al. Sea-level change in the dutch wadden sea. *Netherlands Journal of Geosciences*, 97(3):79–127, 2018.

[13] G.J. van den Born, D. Henkens F. Kragt, B. Rijken, B. van Bemmel, and S. van der Sluis. Subsiding soils, rising costs. `https://www.pbl.nl/en/publications/subsiding-soils-rising-costs`, note = Accessed: 25-02-2020.

[14] G. Erkens, van der Meulen, MJ, and H. Middelkoop. Double trouble: subsidence and co 2 respiration due to 1,000 years of dutch coastal peatlands cultivation. *Hydrogeology Journal*, 24:"551–568", 2016.

[15] Karin van Thienen-Visser and Peter A. Fokker. The future of subsidence modelling: compaction and subsidence due to gas depletion of the groningen gas field in the netherlands. *Netherlands Journal of Geosciences*, 96(5):s105–s116, 2017.

[16] Hans De Waal, Annemarie G. Muntendam-Bos, and J.P.A.. Roest. The future of subsidence modelling: Compaction and subsidence due to gas depletion of the groningen gas field in the netherlands. *Netherlands Journal of Geosciences*, 2015.

[17] Comissie Bodemdaling. Land subsidence committee. `https://www.commissiebodemdaling.nl/`, note = Accessed: 03-03-2020.

[18] Patrick J. Fox. *Consolidation and Settlement Analysis. The Civil Engineering Handbook*. 2003.

[19] Hirochika Hayashi, Satoshi Nishimoto, and Takahiro Yamanashi. Applicability of settlement prediction method to peaty ground. *Soils and Foundations*, 56:"144–151", 2016.

[20] B. H. Fellenius and A. Eslami. Soil profile interpreted from cptu data. *Proc. Geotechnical Engineering Conference, Asian Institute of Technology, Bangkok, Thailand*, 2000.

[21] René K.W.M. KLAASSEN. Life expectation of wooden foundations - a non-destructive approach. *International Symposium non destructive testing in Civil Engineering, Berlin, Germany*, 2015.

[22] Bronswijk and Evers-Vermeer. Shrinkage characteristics of clay soils in the netherlands. *Instituut voor Cultuurtechniek en Waterhuishouding, Wageningen, Netherlands*, 1987.

[23] Ramon F. Hanssen. *Radar Interferometry-Data Interpretation and Error Analysis*. Springer Netherlands, 2001.

[24] L. C. Graham. Synthetic interferometer radar for topographic mapping. *Proceedings of the IEEE*, 62(6):763–768, 1974.

[25] R. M. Goldstein, H. A. Zebker, and C. L. Werner. Satellite radar interferometry: Two-dimensional phase unwrapping. *Radio Science*, 23(4):713–720, 1988.

[26] H. A. Zebker and J. Villasenor. Decorrelation in interferometric radar echoes. *IEEE Transactions on Geoscience and Remote Sensing*, 30(5):950–959, 1992.

[27] Alessandro Ferretti, Andrea Monti-Guarnieri, Claudio Prati, Fabio Rocca, and Didier Massonet. Insar principles - guidelines for sar interferometry processing and interpretation. *ESA Training Manual*, 19, 01 2007.

[28] NSO. Netherlands space office. https://www.spaceoffice.nl/nl/satellietdataportaal/, note = Accessed: 11-12-2019.

[29] Open Access Hub. Copernicus open acess hub. https://scihub.copernicus.eu/, note = Accessed: 14-12-2019.

[30] V. Pinel, M. P. Poland, and A. Hooper. Volcanology: Lessons learned from synthetic aperture radar imagery. *Journal of Volcanology and Geothermal Research*, 12 2014.

[31] A. Ferretti, C. Prati, and F. Rocca. Permanent scatterers in sar interferometry. *IEEE Transactions on Geoscience and Remote Sensing*, 39(1):8–20, 2001.

[32] C. Colesanti, A. Ferretti, F. Novali, C. Prati, and F. Rocca. Sar monitoring of progressive and seasonal ground deformation using the permanent scatterers technique. *IEEE Transactions on Geoscience and Remote Sensing*, 41(7):1685–1701, 2003.

[33] Batuhan Osmanoglu, Filiz Sunar, Shimon Wdowinski, and Enrique Cabral-Cano. Time series analysis of insar data: Methods and trends. *ISPRS Journal of Photogrammetry and Remote Sensing*, 115(11):"90–102", 2015.

[34] Giorgia Giardina, Pietro Milillo, Matthew J. DeJong, Daniele Perissin, and Giovanni Milillo. Evaluation of insar monitoring data for post-tunnelling settlement damage assessment. *Structural Control and Health Monitoring*, 26(2):e2285, 2019. e2285 stc.2285.

[35] *Delft Object-oriented Radar Interferometric Software User's manual and technical documentation.*

[36] M. Nolan, D. R. Fatland, and L. Hinzman. Dinsar measurement of soil moisture. *IEEE Transactions on Geoscience and Remote Sensing*, 41(12):2802–2813, 2003.

[37] Freek van Leijen. *Persistent Scatterer Interferometry based on geodetic estimation theory.* PhD dissertation, Delft University of Technology, 2014.

[38] J. Tribolet. A new phase unwrapping algorithm. *IEEE Transactions on Acoustics, Speech, and Signal Processing*, 25(2):170–177, 1977.

[39] D. Perissin. Sarproz webpage www.sarproz.com, note = accessed: 01-12-2019 .

[40] D. Perissin. *Interferometric SAR Multitemporal Processing: Techniques and Applications*, pages 145–176. 11 2016.

[41] USGS. Srtm. https://www.usgs.gov/centers/eros/science/usgs-eros-archive-digital-elevation-shuttle-radar-topography-mission-srtm-1-arc?qt-science_center_objects=0#qt-science_center_objects, note = Accessed: 05-03-2020.

[42] Andy Hooper, Howard Zebker, Paul Segall, and Bert Kampes. A new method for measuring deformation on volcanoes and other natural terrains using insar persistent scatterers. *Geophyiscal Research Letters*, 31:1–5, 12 2004.

[43] P. Berardino, G. Fornaro, R. Lanari, and E. Sansosti. A new algorithm for surface deformation monitoring based on small baseline differential sar interferograms. *IEEE Transactions on Geoscience and Remote Sensing*, 40(11):"2375–2383", 11 2002.

[44] T. W. Anderson and D. A. Darling. Asymptotic theory of certain 'goodness of fit' criteria based on stochastic processes. *Ann. Math. Statist.*, 23(2):193–212, 06 1952.

[45] A. N. PETTITT. A two-sample Anderson-Darling rank statistic. *Biometrika*, 63(1):161–168, 04 1976.

[46] Yu Morishita and Ramon F. Hanssen. Deformation parameter estimation in low coherence areas using a multisatellite insar approach. *IEEE Transactions on Geoscience and Remote Sensing*, 53(8):"4275–4283", 08 2015.

[47] Wageningen University BodemenOndergrond, TNO and Ministerie van Binnenlandse Zaken en Koninkrijksrelaties. Dinoloket. `https://www.dinoloket.nl/ondergrondgegevens`, note = Accessed: 10-06-2020.

[48] Kadaster. Pdok. `https://www.pdok.nl/geo-services/-/article/rdinfo`, note = Accessed: 03-05-2020.

[49] Mengshi Yang, Paco Lopez Dekker, Prabu Dheenathayalan, Mingsheng Liao, and Ramon Hanssen. On the value of corner reflectors and surface models in insar precise point positioning. *ISPRS Journal of Photogrammetry and Remote Sensing*, 158:113–122, 10 2019.